

8-31-2011

Steady states, non-steady evolution, pinch-off and post-pinch-off of axisymmetric drops in Stokes flow

Shadi Askarian Naderi

Follow this and additional works at: https://digitalrepository.unm.edu/math_etds

Recommended Citation

Naderi, Shadi Askarian. "Steady states, non-steady evolution, pinch-off and post-pinch-off of axisymmetric drops in Stokes flow." (2011). https://digitalrepository.unm.edu/math_etds/35

This Dissertation is brought to you for free and open access by the Electronic Theses and Dissertations at UNM Digital Repository. It has been accepted for inclusion in Mathematics & Statistics ETDs by an authorized administrator of UNM Digital Repository. For more information, please contact disc@unm.edu.

Shadi A. Naderi

Candidate

Mathematics and Statistics

Department

This dissertation is approved, and it is acceptable in quality and form for publication:

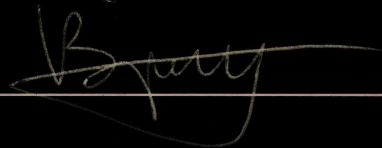
Approved by the Dissertation Committee:



, Chairperson







Steady States, Non-Steady Evolution, Pinch-off and Post-Pinch-off of Axisymmetric Drops in Stokes Flow

by

Shadi Askarian Naderi

B.S., Mathematics, University of Mashad, 2001
M.S., Mathematics, University of New Mexico, 2007
Ph.D., Mathematics, University of New Mexico, 2011

DISSERTATION

Submitted in Partial Fulfillment of the
Requirements for the Degree of

Doctor of Philosophy
Mathematics

The University of New Mexico

Albuquerque, New Mexico

June, 2011

©2011, Shadi Askarian Naderi

Dedication

I would like to dedicate this dissertation to my wonderful family. To my amazing parents and brother for all the sacrifices and encouragements. Especially to my loving husband for his patience and understanding through these years and for his support and guidance in writing this dissertation.

Acknowledgments

This dissertation could have not been written without the support and guidance of many individuals. I am grateful to my dissertation advisor, professor Monika Nitsche for her excellent guidance, caring and patience. I became interested in fluid dynamics through her research work after my previous advisor, professor Alejandro Aceves, who moved to Southern Methodist University. Dr. Nitsche's flexibility in scheduling was crucial in finishing this dissertation. In the process of completing this dissertation, her patience and support helped me overcome many obstacles. I also would like to thank professor Aceves who has always been there to listen and give advice. I would like to acknowledge my committee members, professor Stephen Lau, professor Evangelos Coutsias and professor Peter Vorobieff for their support and valuable comments. My sincere thanks also goes to professor Luke Lester for his valuable guidance on a separate research project that I explored during my graduate studies. I would like to thank my friends that kept me sane throughout this journey. I greatly value friendship and appreciate their support. I am truly grateful to my parents, brother and my in-laws for their endless support and patience. Lastly, I would like to thank my husband, Dr. Nader Naderi, for all his support and understanding.

Steady States, Non-Steady Evolution, Pinch-off and Post-Pinch-off of Axisymmetric Drops in Stokes Flow

by

Shadi Askarian Naderi

ABSTRACT OF DISSERTATION

Submitted in Partial Fulfillment of the
Requirements for the Degree of

Doctor of Philosophy
Mathematics

The University of New Mexico
Albuquerque, New Mexico

June, 2011

Steady States, Non-Steady Evolution, Pinch-off and Post-Pinch-off of Axisymmetric Drops in Stokes Flow

by

Shadi Askarian Naderi

B.S., Mathematics, University of Mashad, 2001

M.S., Mathematics, University of New Mexico, 2007

Ph.D., Mathematics, University of New Mexico, 2011

Ph.D., Mathematics, University of New Mexico, 2011

Abstract

A good understanding of drop evolution and breakup is important in many applications. For instance, controlling the liquid droplet size is crucial in atomization processes such as fuel combustion and fertilizer application, as well as drop-on-demand technologies such as ink-jet printing and DNA arraying. In these applications, the length scales are very small relative to viscosity so that the Reynolds number is much less than unity. The aim of this work is to investigate the evolution and breakup of drops in Stokes flow.

Drop evolution depends on different factors, such as the drop size, the viscosity, any applied force, or surface tension. In this dissertation, the behavior of axisymmetric viscous drops in a nonlinear strain field is investigated for various parameters.

The three non-dimensional parameters that determine the flow in our case are: the capillary number Ca which measures the strength of the strain field and drop viscosity relative to surface tension, the ratio λ of inner to outer viscosities, and the relative nonlinearity c_2 of the background flow. It is known that the drop approaches a steady state for sufficiently small values of Ca and that there exists a critical value of the capillary number, Ca_{cr} , above which no steady states exist. We examine the evolution of the drop as a function of these three parameters. Our main results are explained in three parts. (1) A full classification of the steady-state solutions in the parameter-space for $Ca \leq Ca_{cr}$ is presented. In particular, we describe the deformation, maximum curvature and the critical capillary number as functions of the key parameters. We find previously unobserved biconcave steady shapes. (2) The non-steady evolution for $Ca > Ca_{cr}$ is studied and classified. With $c_2 = 0$, the drop keeps elongating and becomes more pointed in time. With positive values of c_2 , the surface approaches a cusp as it increases in length. With negative values of c_2 , the surface collapses at two points on the axis in finite time. Thus the solution has a finite time pinch-off singularity (3) Based on experimental observations, the drop surface is expected to break at the time of pinch-off and reconnect to form several smaller drops. We develop a numerical method to simulate the break-and-reconnection process. This enables us to compute the after pinch-off drop evolution. Our simulations indicate that this phenomenon has a linear self-similar behavior before and after pinch-off. Further pinch-offs is observed. Throughout this work the fifth-order boundary integral method presented by Nitsche et al. [1] is used. This method enables us to resolve the flow using fewer computational points compared to the commonly used second-order method. Furthermore, it is shown that the uniformly fifth-order method proposed in earlier work [1] makes a significant improvement in the results in certain cases.

Contents

List of Figures	xii
Glossary	xviii
1 Introduction	1
2 Governing Equations	7
2.1 Stokes Approximation	8
2.2 Harmonic and Biharmonic Functions	10
2.3 Green's Function of Stokes Flow	11
2.4 Lorenz Reciprocal Identity	14
2.5 Boundary Integral Formulation	15
2.6 Non-dimensionalization	21
2.6.1 Non-zero Surface Tension, $\gamma > 0$	21
2.6.2 Zero Surface Tension, $\gamma = 0$	23

3	Numerical Approach	25
3.1	Discretization and Initial Conditions	25
3.2	Evaluating Particle Velocity	26
3.2.1	Quadrature Rules For Integrals	28
3.2.2	Finding \mathbf{u} and \mathbf{v} , $\lambda > 0$, $\lambda \neq 1$	29
3.3	Evolving Cartesian Coordinates	30
3.4	Evolving Arclength-Angle Coordinates	31
3.4.1	Equal Arclength	31
3.4.2	Mesh Refinement	33
4	Steady States For $Ca < Ca_{cr}$ and Non-Steady Evolution for $Ca > Ca_{cr}$	37
4.1	Background Flow	37
4.2	Time Evolution of a Drop Towards Steady States	39
4.2.1	Identifying the Steady States	41
4.3	Classification of Steady States Solutions	43
4.3.1	Steady States as Function of $Ca < Ca_{cr}$	43
4.3.2	Steady States as Function of λ , $Ca = Ca_{cr}$	46
4.3.3	Steady States as Function of c_2 , $Ca = Ca_{cr}$	50
4.4	Non-steady Evolution	52
4.4.1	Cusp or Corner?	54

Contents

4.4.2	Effect of Accuracy	56
4.4.3	Pinch-off or Exponential Growth?	58
5	Finite Time Pinch-off and Recoiling	63
5.1	Pre Pinch-off Numerical Results	63
5.2	Numerical Method to Simulate the Breaking of a Drop	67
5.3	Numerical Results of Recoiling	71
6	Conclusions	76
6.1	Summary and Conclusions	76
6.2	Proposed Future Research	77
	Appendices	78
A	Derivation of G, Ω, p and T	79
B	Contribution of u_∞ on Inner and Outer Velocity	82
C	Scaling Arguments	85
	References	87

List of Figures

1.1	Taylor's 'four roller' apparatus.	2
1.2	Some steady state axisymmetric bubbles subject to the Sherwood straining flow computed by Pozrikidis for $\lambda = 0$. (a) $c_2 = 0.5$ (b) $c_2 = 0$ (c) $c_2 = -0.2$	3
1.3	Time evolution of axisymmetric bubbles subject to the Sherwood straining flow presented by Pozrikidis. (a) $c_2 = 0.5$ and $Ca = \infty$ (b) $c_2 = 0$ and $Ca = \infty$ (c) $c_2 = -0.2$ and $Ca = 0.15$	4
2.1	An axisymmetric viscous drop containing a fluid of viscosity μ_2 placed in a fluid of viscosity μ_1 with outer flow velocity \mathbf{u}^∞ , C is the curve on the right half of x-y plane representing the surface of the drop, $\alpha = 0$ and $\alpha = \pi$ are the points where C crosses the y -axis.	7
2.2	A control volume V within the domain of a flow bounded by the closed surface D . \mathbf{n} is the outward normal.	16
3.1	(a) Curve C representing the surface of the drop with poles $\alpha = 0$ and $\alpha = \pi$ (b) Discretized curve.	26

List of Figures

3.2	Axisymmetric surface S , axis of symmetry y , azimuthal angle ϕ and outward normal vector \mathbf{n}	27
3.3	Tangent angle $\theta(\alpha, t)$, and the arc-length $s(\alpha)$	31
3.4	(a) $R(\alpha)$ constructed to bunch the points at the tips, $\varepsilon=0, 0.5$, and 0.9 (b) $g(\alpha)$ constructed to bunch the points near the pinch-off $\varepsilon=0, 0.5$, and 0.9 (c) $R(\alpha)$ constructed to bunch the points at only one tip $\varepsilon=0, 0.5$, and 0.9	35
4.1	Background flow. (a) $c_2 = 0.5$ (b) $c_2 = 0$ (c) $c_2 = -0.2$	38
4.2	Computed time evolution of axisymmetric drops. (a) $c_2 = 0.5, \lambda = 0.01, Ca = 0.15$ (b) $c_2 = 0, \lambda = 0.01, Ca = 0.25$ (c) $c_2 = -0.2, \lambda = 0.01, Ca = 0.2$ (d) $c_2 = -0.5, \lambda = 0.01, Ca = 0.3$	40
4.3	Maximum curvature κ_{max} , maximum y -coordinate y_{max} , and deformation D , vs. time.	41
4.4	Ratios $r(k) = \Delta Q_{k+1}/\Delta Q_k$, where $\Delta Q_k = Q_{k+1} - Q_k$, and Q is the maximum curvature (r_κ), the maximum y -coordinate (r_y), and deformation (r_D), vs. time.	42
4.5	(a) Initial solution and steady states for $Ca = 0.005, 0.01, 0.0511, 0.0876, 0.1164, 0.1387, 0.1560, 0.1690, 0.1787, 0.1855, 0.1900, 0.1924, \lambda = 0.05, n = 512, \Delta t = 0.01$, and $c_2 = 0$ (b) Deformation as a function of capillary number (c) Maximum curvature as a function of capillary number.	44
4.6	(a) Steady States for $Ca = 0.005 : 0.01 : 0.205, \lambda = 0, c_2 = 0, n = 512$ and $\Delta t = 0.01$. (b) Deformation as a function of capillary number (c) Maximum curvature as a function of capillary number.	45

List of Figures

4.7	Steady States for $Ca = 0.3$, $\lambda = 0$, $c_2 = 0$	46
4.8	(a) Steady states for $Ca = Ca_{cr}$ and $\lambda = 10, 1, 0.05, 0.02, 0.01$ (b) Deformation as a function of $\log_{10}(\lambda)$ (c) Maximum curvature as a function of $\log_{10}(\lambda)$	47
4.9	(a) Ca_{cr} as a function of $\log_{10}(\lambda)$, $c_2 = 0$ (b) Ca_{cr}^* as a function of $\log_{10}(\lambda)$, $c_2 = 0$	48
4.10	Ca_{cr}^* as a function of $\log_{10}(\lambda)$ presented by Eggers, $c_2 = 0$	48
4.11	(a) Rescaled length $l^* = l\lambda^{1/3}$ as a function of $\log_{10}(\lambda)$, $c_2 = 0$, $Ca = Ca_{cr}$ (b) Rescaled length $l^* = l\lambda^{1/3}$ as a function of $Ca^* = Ca\lambda^{1/6}$, $c_2 = 0$, $Ca = Ca_{cr}$	49
4.12	(a) Steady States for $c_2 = -0.1, -0.2, -0.3, -0.4$ and -0.5 , $\lambda = 1$ and $Ca = Ca_{cr}$ (b) Steady States for $c_2 = 0, 0.1, 0.2, 0.3, 0.4$ and 0.5 , $\lambda = 1$ and $Ca = Ca_{cr}$	50
4.13	(a) Maximum curvature as a function of c_2 , $\lambda = 1$ (b) Critical capillary number as a function of c_2 , $\lambda = 1$ (c) Deformation as a function of c_2 , $\lambda = 1$	51
4.14	Evolution of drops passed the critical capillary numbers, $\lambda = 0.01$. (a) $c_2 = 0.5$, $Ca = 0.2$ (b) $c_2 = 0.5$, $Ca = \infty$ (c) $c_2 = 0$, $Ca = 0.3$ (d) $c_2 = 0$, $Ca = \infty$ (e) $c_2 = -0.2$, $Ca = 0.3$ (f) $c_2 = -0.2$, $Ca = \infty$	53
4.15	(a) Tangent angle θ (b) Drop profiles for $Ca = 0.5$, $c_2 = 0.5$, $n = 256$, $\Delta t = 0.0001$, $\varepsilon_{max} = 0.999$, $\lambda = 0.01$, $t = 0.4, 0.5$ and 0.6396	54
4.16	Angle θ as s function of arc length for $Ca = 0.5$, $c_2 = 0.5$ and $t = 0 : 500 : 6396$. Arrow displays the direction of increasing time.	55
4.17	Length as a function of time for $Ca = 0.5$, $c_2 = 0.5$ and $t = 0 : 6396$	55

List of Figures

4.18	(a) Evolution of a drop with $c_2 = 0$, $\lambda = 10$, $Ca = 0.4$, $n = 2048$ and $\Delta t = 0.005$ (b) Maximum curvature as a function of time using point wise method (c) Curvature as a function of time using uniform method.	56
4.19	(a) Curvature as a function of time for $c_2 = 0.5$, $Ca = 0.5$, $n = 2048$, and $\Delta t = 0.001$ (b) $1/\text{curvature}$ as a function of time using point wise method (c) $1/\text{curvature}$ as a function of time using uniformly fifth-order method.	58
4.20	The maximum value of x component of the drop in time in semi-log scale for $Ca = \infty$, $\lambda = 0.5$, $c_2 = -0.2$ up to time $t = 33$	59
4.21	The values of $1/x_{max}$ component of the drop for $n = 256$, $\Delta t = 0.0005$ (solid curve), $n = 512$, $\Delta t = 0.0001$ (blue dashed-dot curve) and $n = 1024$, $\Delta t = 0.0001$ (dot curve).	60
4.22	Evolution of a drop towards pinch-off for $c_2 = -0.2$ and $\lambda = 0.01$. (a) $Ca = 0.5$ (b) $Ca = 0.6$ (c) $Ca = 0.7$ (d) $Ca = 1$	61
4.23	Evolution of the drops towards pinch-off for different values of viscosity ratio. (a) $\lambda = 0.01$, $c_2 = -0.2$, $Ca = 0.5$ (b) $\lambda = 1$, $c_2 = -0.2$, $Ca = 0.2$	62
5.1	Evolution of a drop with $c_2 = -0.2$, $Ca = 0.2$ and $\lambda = 1$ computed using uniformly fifth-order method with $n = 4096$ points. (a) Solution is shown for $t = 0 : 5 : 35$, $t = 35 : 0.25 : 36$, $t = 36 : 0.1 : 37.9$, $t = 37.9 : 0.02 : 38$ and $t = 38 : 0.000025 : 38.00685$ (b) The close-up of bottom pinch-off for $t = 38 : 0.00025 : 38.0066$	64

List of Figures

5.2	(a) Minimum radius of neck vs. time computed using $n = 4098$ (o), $n = 2048$ (X) and $n = 1024$ (+) (b) The close-up. The dashed line is the least squares fit for the interval $(38.0065, 38.0069)$	65
5.3	(a) Position of pinch-off vs. time computed using $n = 4098$ (b) The close-up. The dashed line is a least squares fit for a small interval near the pinch-off.	66
5.4	(a) Minimum radius of the neck, x_{min} as a function of the time to pinch, $t_p - t$ (b) $y_{min} - y_0$ as a function of the time to pinch, $t_p - t$	66
5.5	Self-similar solution shown for upper pinch-off.	67
5.6	Close up of the solution near pinch-off at $t = 38.00685$ and $n = 4096$, points used for cutting at $j_1 = 905$ and $j_2 = 915$ (Red star), $j_1 = 908$ and $j_2 = 913$ (Blue pentagon) and the red curve displays that x coordinate departs away from its minimum value.	69
5.7	(a) Shape of the three separated drops after pinch-off (b) Solution at $t = 38.00685$ (dashed line), cut and reconnected curves (solid line) , α^* and α_n , start and end points of the gap for the bottom drop, β^* and β_n start and end points of the gap for the middle drop.	70
5.8	(a) θ as a function of arc length s for the bottom drop (-) and fifth-order polynomial interpolation (.) (b) Close up with start point α_n and end point α^* of the interpolation.	70
5.9	Solution before pinch-off at $t = 38.00685$, $n=4096$ (dashed curve), Cut solution with cut points at $j_1 = 905$ and $j_2 = 916$ (dotted curve), Cut solution with cut points at $j_1 = 908$ and $j_2 = 913$ (solid curve).	71
5.10	Time evolution after pinch-off for $t = 0 : 0.01 : 0.1$	72

List of Figures

5.11	First row: (a) Evolution of drops after pinch-off for $t = 0 : 0.3 : 1.53$ (b) Close up of part (a) (c) Close up of new pinch-off for $j=4096$, cut at $j=905,916$ (dashed curve), $n=4096$ cut at $j=908,913$ (dot-dashed curve) and $n=2048$ cut at 510, 521 (doted curve). Second row: Step by step evolution shown in part (b).	73
5.12	Position of the tips y_{min} with respect to time for satellite drop (Solid line), bottom drop (dashed line) and the least square fit (dashed-dot line) $t = t_c : 0.01 : t_c + 0.21$	74
5.13	(a) Position of pinch-off as a function of time $t - t_p$ for the satellite drop (b) Position of pinch-off as a function of time $t - t_p$ for the bottom drop, dashed line is plotting $t - t_p$	74
5.14	Self-similar solution after pinch-off shown for upper pinch-off.	75

Glossary

Ca	Capillary number
μ_1, μ_2	Viscosity of the external fluid and viscosity of the internal fluid
λ	Viscosity ratio μ_2/μ_1
R	Initial radius of the drop
γ	Surface tension
G	Measure of the strain strength
\mathbf{u}	Radial velocity
\mathbf{v}	Axial velocity
c_2	Coefficient of non-linear term in the outer flow
y	Radial coordinate
x	Axial coordinate
\mathbf{u}^∞	Outer flow velocity
\mathbf{u}_s	Single layer velocity
\mathbf{u}^d	Double layer velocity

Glossary

n	Number of computational points
ρ	Density
p	Pressure
\mathbf{b}	Body force
Re	Reynolds number
$\boldsymbol{\sigma}, T$	Stress tensor
ω	Vorticity
D	Deformation
κ	Curvature
Ca_{cr}	Critical capillary number
Ca_s	Singular capillary number

Chapter 1

Introduction

Drop evolution has been studied for over ten decades experimentally, analytically, and numerically. One of the earliest experimental studies is the work of Taylor [2] in 1934. He constructed a ‘four roller’ apparatus, indicated in the sketch in figure 1.1. The rollers are immersed in a fluid of viscosity μ_1 and turn so as to produce a strain velocity along one axis. Then, a drop of fluid with viscosity μ_2 is placed between the wheels and the results are photographed. The flow is characterized by two non-dimensional quantities, Ca and λ . The capillary number $Ca = RG\mu_1/\gamma$ measures the strength of the strain field G , the initial drop radius R , and the outer fluid viscosity μ_1 , relative to the surface tension γ . The value $\lambda = \mu_2/\mu_1$ is the ratio of inner over outer fluid viscosities. Taylor’s experiment revealed the existence of steady states as long as the capillary number is below a critical value Ca_{cr} . He also found that for $Ca > Ca_{cr}$, the drop elongates and bursts. Since the drop sizes in the experiment are about $10^{-5}m$ and the kinematic viscosity of a commonly used outer fluid such as oil is about $1 - 10 \text{ pa} \cdot \text{s}$, the Reynolds number $Re = LU/\nu \ll 1$ is much smaller than unity. Such flows are well-approximated by Stokes equations, which have been the basis of later numerical and analytical studies.

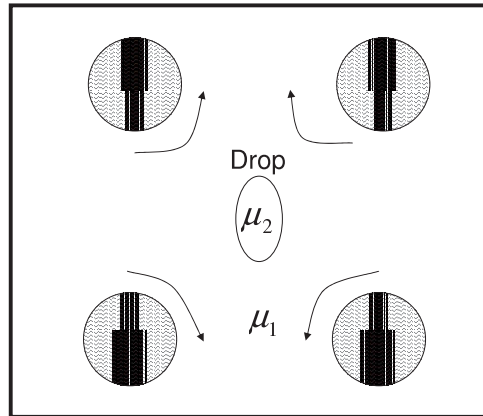


Figure 1.1: Taylor's 'four roller' apparatus.

Taylor [3] and Buckmaster [4] used slender body theory to develop a theory for the stationary shape of the drops. Barthes-Biesel and Acrivos [5] presented a theoretical model which for sufficiently large strain fields qualitatively predicts the deformation and break-up of the droplets. Siegel [6] applied analytical and numerical methods to investigate the time evolution of an inviscid bubble ($\lambda = 0$) in two-dimensional Stokes flow. He considered constant surface tension as well as variable surface tension and found that the steady state solutions for inviscid bubbles exist for all values of the capillary number.

Youngren and Acrivos [7], [8] first introduced the basic numerical method for axisymmetric Stokes flow past solid particles using a boundary integral approach. They applied this method to drops and showed a good agreement with theoretical work of Barthes-Biesel, Acrivos and Buckmaster. They determined the steady shapes for inviscid bubbles ($\lambda = 0$) and predicted cuspidal shapes. Rallison and Acrivos [9] and Rallison [10] further improved the numerical method and computed the critical

capillary number for various $\lambda > 0$. They also showed that the drop elongates indefinitely for larger capillary numbers. Pozrikidis [11] computed a sample of steady states for $\lambda = 0$. Most recently, Eggers and du Pont [12] found a family of stable and unstable steady states. They did not compute the flow evolution, but used Newton's method to find the stationary solutions iteratively.

In most analytical and numerical works, the strain field is assumed to be linear. Sherwood [13] introduced a nonlinear correction with magnitude c_2 into the background flow. Pozrikidis [11] computed different drop shapes for $c_2 \neq 0$ and $\lambda = 0$. He computed some steady states for finite capillary numbers as shown in figure 1.2 and unsteady elongations for infinite Ca as shown in figure 1.3(a,b). 1.3(c) displays some unsteady dumbbell shapes for finite Ca . Although Pozrikidis [11] presents some

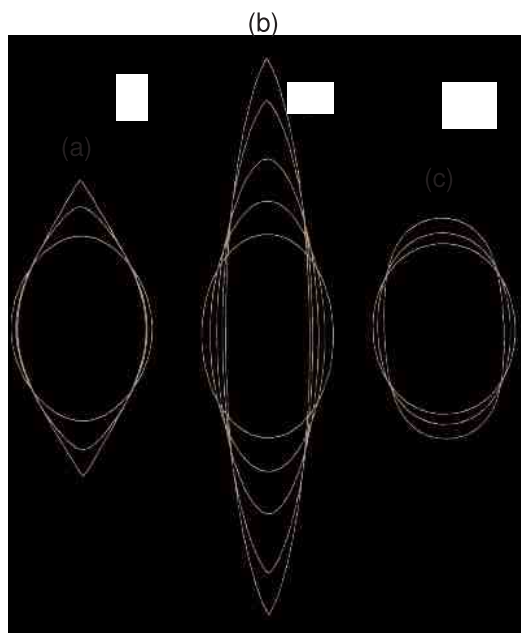


Figure 1.2: Some steady state axisymmetric bubbles subject to the Sherwood straining flow computed by Pozrikidis for $\lambda = 0$. (a) $c_2 = 0.5$ (b) $c_2 = 0$ (c) $c_2 = -0.2$.

drop shapes for $c_2 \neq 0$, a full complete study of the effect of these key parameters

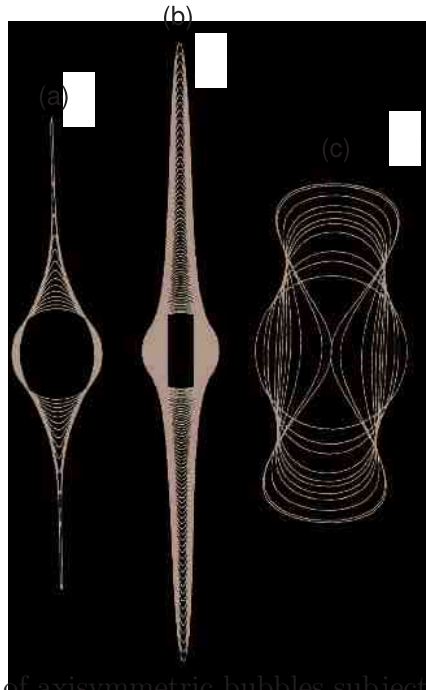


Figure 1.3: Time evolution of axisymmetric bubbles subject to the Sherwood straining flow presented by Pozrikidis. (a) $c_2 = 0.5$ and $Ca = \infty$ (b) $c_2 = 0$ and $Ca = \infty$ (c) $c_2 = -0.2$ and $Ca = 0.15$.

on drop evolution is missing from the literature.

Recently, drop breakup has been the subject of several experimental and numerical investigations. These studies date back to approximately 1990. Eggers [14] considered an axisymmetric column of fluid with a free surface and demonstrated that the shape of the neck and its velocity is described by scaling functions. Stone and Leal [15] presented experimental results of breaking bubbles and numerical simulations showing that pinching would occur just before the breakup. Cristini et al. [16] developed a three-dimensional algorithm to simulate the process of drop breakup in viscous flows. In experiments, after the drop breaks into droplets, the surface recoils away from the breaking point. Brenner et al. [17] simulated the breaking of inviscid bubbles and found that after breakup the flow does not follow a simple scaling law due to some instability in the fluid. Lister and Stone [18] considered viscous drops

and derived a self-similar scaling law from the balance between surface tension and viscous forces when inertia is negligible. They show that both axial and radial scales decrease linearly as time approaches pinch-off. Zhang and Lister [19] and Sierou and Lister [20] also performed some studies in similarity solutions for capillary pinch-Off. Gekle et al. [21] studied the pinch-off of an axisymmetric air bubble in an inviscid fluid and they showed that the drop eventually follow the universal behavior.

Several works address other aspects of drop evolution. For instance, the effects of surfactants have been studied numerically and experimentally. Stone and Leal [22] studied the deformation of drops when adding a surfactant. Manga and Stone [23] present the two-dimensional simulations. Later, Loewenberg and Hinch [24] presented a three-dimensional simulation approach. The same year, Antanovskii [25] included the effects of an insoluble surfactant for steady flows. Pozrikidis [11] uses a finite-volume method to further compute the evolution of the concentration of an insoluble surfactant over an interface. Eggleton et al. [26] investigated the effects of surfactants on a drop in an extensional flow. Jin et al. [27] studied the effects of surfactants on altering the pinching process. Further, Lac and Homsy [28] presented the drop formation in a steady electric field. They identified various break-up points depending on resistivity, permittivities, and viscosity ratios. However, these works are beyond the scope of the present study.

The main contributions of this dissertation are the following

(1) This work presents a full classification of the steady states in the parameter space c_2 , λ and $Ca \leq Ca_{cr}$. Where possible, the findings are compared with previous analytical and numerical results. We find previously unobserved biconcave shapes, and correct some results in the literature describing the critical capillary number as a function of λ . (2) The non-steady evolution of drops for $Ca > Ca_{cr}$ is described and classified. In particular, we find that, when $c_2 < 0$ and $Ca_{cr} < Ca < Ca_s$, the drop develops a finite time singularity, and pinches at two points on the axis

Chapter 1. Introduction

of symmetry. Ca_s is a limiting value, above which no pinching was observed. (3) Evolution of the drop toward pinch-off is studied and a method is developed which enables us to compute past pinch-off. We find similarity behavior of the drop before and after pinch-off. Formation of multiple pinch-offs is observed.

This dissertation is organized as follows. Chapter 2 derives the governing boundary integral equations used in this study, following Pozrikidis [29]. Chapter 3 presents the numerical approach used in this work. Chapter 4 exhibits the time evolution of drop interfaces followed by a complete classification of the steady states as functions of λ , Ca and c_2 . The non-steady evolution for $Ca > Ca_{cr}$ is also presented in this chapter. Chapter 5 describes the numerical method used to simulate breaking and reconnection for $c_2 < 0$. Self similar behavior before and after pinch-off is found. Lastly, a summary of our work and remaining future work are presented in chapter 6.

Chapter 2

Governing Equations

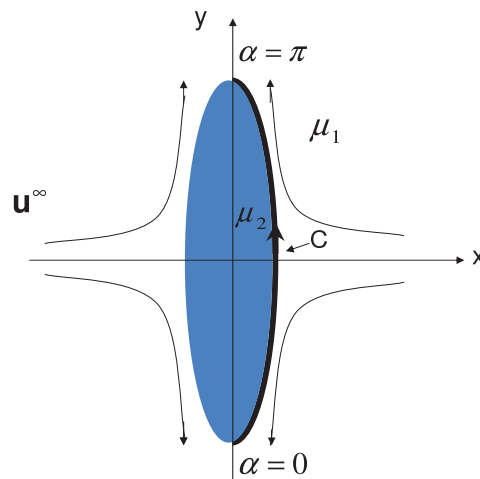


Figure 2.1: An axisymmetric viscous drop containing a fluid of viscosity μ_2 placed in a fluid of viscosity μ_1 with outer flow velocity \mathbf{u}^∞ , C is the curve on the right half of x-y plane representing the surface of the drop, $\alpha = 0$ and $\alpha = \pi$ are the points where C crosses the y -axis.

As shown in figure 2.1, an axisymmetric drop with viscosity μ_2 is placed in a fluid of viscosity μ_1 with far field velocity \mathbf{u}^∞ where y is the axis of symmetry. We

are interested in the regime where $Re \ll 1$. These flows are approximated by Stokes fluid flows. Stokes flow is a linear approximation of fluid in which the viscous forces dominate the inertial forces; this is the case when length scales are small, velocity is low or viscosity is very large. To compute the evolution of these drops, we need to find the velocity on the surface of the drop. In this chapter, we derive the formulas for the velocity.

2.1 Stokes Approximation

In this section, following the work of Pozrikidis [29], the steady Stokes approximation is derived from the Navier-Stokes equations in a regime where the Reynolds number are much smaller than unity.

The Navier-Stokes equations are

$$\rho \left(\frac{\partial \mathbf{u}}{\partial t} + \mathbf{u} \cdot \nabla \mathbf{u} \right) = -\nabla p + \mu \nabla^2 \mathbf{u} + \rho \mathbf{b}, \quad \nabla \cdot \mathbf{u} = 0 \quad (2.1.1)$$

where \mathbf{u} is the field velocity, ρ is the density, μ is the fluid viscosity, \mathbf{b} is a body force, and p is the pressure. We assume ρ and \mathbf{b} are constant. Let L be a characteristic length, U a characteristic velocity and T a characteristic time. If $T = L/U$, then $\beta = Re$, and the Stokes regime $Re \ll 1$ is reached if L or U are very small relative to μ . Equation (2.1.1) can be non-dimensionalized, introducing the following dimensionless quantities,

$$\mathbf{u}' = \frac{\mathbf{u}}{U}, \quad \mathbf{x}' = \frac{\mathbf{x}}{L}, \quad \mathbf{t}' = \frac{\mathbf{t}}{T}, \quad p' = \frac{pL}{\mu U}.$$

By rewriting equation (2.1.1) in terms of primed variables, we obtain,

$$\rho \left(\frac{\partial \mathbf{u}' U}{\partial \mathbf{t}'} + \frac{1}{L} \mathbf{u}' U \cdot \nabla_{\mathbf{x}'} (\mathbf{u}' U) \right) = -\frac{\mu U}{L^2} \nabla_{\mathbf{x}'} p' + \frac{\mu}{L^2} \nabla_{\mathbf{x}'}^2 (\mathbf{u}' U) + \rho \mathbf{b},$$

that is,

$$\frac{\rho U}{T} \frac{\partial \mathbf{u}'}{\partial \mathbf{t}'} + \frac{\rho U^2}{L} \mathbf{u}' \cdot \nabla_{\mathbf{x}'} (\mathbf{u}') = -\frac{\mu U}{L^2} \nabla_{\mathbf{x}'} p' + \frac{\mu U}{L^2} \nabla_{\mathbf{x}'}^2 \mathbf{u}' + \rho \mathbf{b}.$$

Multiplying both sides by $\frac{L^2}{U\mu}$, we obtain,

$$\frac{\rho L^2}{\mu T} \frac{\partial \mathbf{u}'}{\partial t'} + \frac{\rho U L}{\mu} \mathbf{u}' \cdot \nabla_{\mathbf{x}'}(\mathbf{u}') = -\nabla_{\mathbf{x}'} p' + \nabla_{\mathbf{x}'}^2 \mathbf{u}' + \frac{\rho \mathbf{b} L^2}{U \mu}.$$

Let

$$\beta = \frac{L^2}{\nu T}, \quad Fr = \frac{U^2}{|\mathbf{b}| L}, \quad Re = \frac{UL}{\nu}, \quad \nu = \frac{\mu}{\rho},$$

where β is the frequency parameter, Fr is the Froude number, Re is the Reynolds number and ν is the kinematic viscosity. Therefore the dimensionless form of equation (2.1.1) is

$$\beta \frac{\partial \mathbf{u}'}{\partial t'} + Re \mathbf{u}' \cdot \nabla_{\mathbf{x}'} \mathbf{u}' = -\nabla_{\mathbf{x}'} p' + \nabla_{\mathbf{x}'}^2 \mathbf{u}' + \frac{Re}{Fr} \frac{\mathbf{b}}{|\mathbf{b}|}. \quad (2.1.2)$$

If $Re, \beta \ll 1$, then all terms on the left-hand side of equation (2.1.2) are small relative to the terms on the right-hand side. These regimes are reached when $L \ll 1$ or $\nu \gg 1$. Therefore equation (2.1.2) simplifies to

$$-\nabla_{\mathbf{x}'} p' + \nabla_{\mathbf{x}'}^2 \mathbf{u}' + \frac{Re}{Fr} \frac{\mathbf{b}}{|\mathbf{b}|} = 0. \quad (2.1.3)$$

The fraction $Re/Fr = L^2 |\mathbf{b}| / U \nu$ may also be negligible depending on how small or large the length, velocity, and the body force are. For instance if L, U and \mathbf{b} are $O(1)$, and $\nu \gg 1$, then the body force is negligible while it will not vanish if body force is large and velocity is small. Going back to dimensional variables, the approximating Stokes equations are

$$-\nabla p + \mu \nabla^2 \mathbf{u} + \rho \mathbf{b} = 0, \quad (2.1.4)$$

derived by George Gabriel Stokes (August 1819-February 1903). The Stokes equations imply that pressure, viscous and body forces are in balance at any time, and that the structure of the flow only depends on the boundary conditions. In some particular cases where a flow is characterized by a sudden acceleration, the structure of the flow depends on both the history of the motion and on the boundary conditions. In such a case $\beta \sim 1$ and the flow is approximated by

$$\rho \frac{\partial \mathbf{u}}{\partial t} = -\nabla p + \mu \nabla^2 \mathbf{u} + \rho \mathbf{b}. \quad (2.1.5)$$

In this dissertation, the drop velocity is computed using the steady Stokes equations. The drop is then evolved with this velocity, thereby changing the flow. This is known as the quasi-steady Stokes approximation.

2.2 Harmonic and Biharmonic Functions

This section derives the harmonic and biharmonic functions to be used in the derivation of the boundary integral formulation. The steady Stokes equations (2.1.4) can be written as

$$\nabla \cdot \boldsymbol{\sigma} + \rho \mathbf{b} = 0. \quad (2.2.1)$$

Here $\boldsymbol{\sigma}$ is the stress tensor given by

$$\sigma_{ij} = -p\delta_{ij} + \mu \left(\frac{\partial u_i}{\partial x_j} + \frac{\partial u_j}{\partial x_i} \right), \quad (2.2.2)$$

where δ_{ij} is the Kronecker delta, and the vector $\nabla \cdot \boldsymbol{\sigma} = \partial_j \sigma_{ij} \mathbf{e}_i$ where \mathbf{e}_i are the cartesian unit basis vectors and the summation convention over repeated indices is used. Taking the divergence of the Stokes equation yields

$$\begin{aligned} \nabla \cdot (-\nabla p + \mu \nabla^2 \mathbf{u} + \rho \mathbf{b}) &= 0, \\ -\nabla \cdot \nabla p + \mu \nabla \cdot \nabla^2 \mathbf{u} + \nabla \cdot (\rho \mathbf{b}) &= 0. \end{aligned}$$

Since density and body force are assumed to be constant, $\nabla \cdot (\rho \mathbf{b}) = 0$. The vector identity $\nabla \cdot \nabla^2 \mathbf{u} = \nabla^2 (\nabla \cdot \mathbf{u})$ and the continuity equation $\nabla \cdot \mathbf{u} = 0$ imply that $\nabla \cdot \nabla^2 \mathbf{u} = 0$. Therefore, pressure is a harmonic function,

$$\nabla^2 p = 0. \quad (2.2.3)$$

Taking the Laplacian of the Stokes equation,

$$\nabla^2 (-\nabla p + \mu \nabla^2 \mathbf{u} + \rho \mathbf{b}) = 0,$$

using the same vector identity as above, and considering that pressure is harmonic, it follows that \mathbf{u} is biharmonic,

$$\nabla^4 \mathbf{u} = 0. \quad (2.2.4)$$

Taking the curl of the Stokes equation,

$$\nabla \times (-\nabla p + \mu \nabla^2 \mathbf{u} + \rho \mathbf{b}) = 0,$$

and using the vector identity $\nabla \times \nabla F = 0$, valid for any twice differentiable function F , and $\nabla \times \nabla^2 F = \nabla^2(\nabla \times F)$, it follows that the vorticity $\boldsymbol{\omega} = \nabla \times \mathbf{u}$ is harmonic as well,

$$\nabla^2 \boldsymbol{\omega} = 0. \quad (2.2.5)$$

2.3 Green's Function of Stokes Flow

The aim of this section is to derive the free space Green's function for Stokes equations, also known as the Stokeslet. The free space Green's function is the solution to the equation with body force given by a point force $(\mathbf{g}/\rho)\delta(\mathbf{x} - \mathbf{x}_0)$,

$$-\nabla p + \mu \nabla^2 \mathbf{u} + \mathbf{g}\delta(\mathbf{x} - \mathbf{x}_0) = 0, \quad (2.3.1)$$

where, $\mathbf{x} \in \mathbb{R}^3$, and $\mathbf{u}, \nabla p \rightarrow 0$ as $|\mathbf{x}| \rightarrow \infty$. Here, \mathbf{g} is an arbitrary constant vector, \mathbf{x}_0 is an arbitrary point, and δ is the three dimensional delta function

$$\delta(\mathbf{x} - \mathbf{x}_0) = \delta(\mathbf{x}_1 - \mathbf{x}_{01})\delta(\mathbf{x}_2 - \mathbf{x}_{02})\delta(\mathbf{x}_3 - \mathbf{x}_{03})$$

Any body force can be written as a sum of such point forces. From the linearity of the Stokes equations, it follows that the solution for any body force in free space can be represented by a sum of Stokeslets. Also from the linearity of Stokes equations, it follows that the solutions of equation (2.3.1) can be written as

$$u_i(\mathbf{x}) = \frac{1}{8\pi\mu} G_{ij}(\mathbf{x} - \mathbf{x}_0) g_j, \quad (2.3.2)$$

$$p(\mathbf{x}) = \frac{1}{8\pi} p_j(\mathbf{x} - \mathbf{x}_0) g_j. \quad (2.3.3)$$

The reason for choosing the coefficient $1/8\pi$ is explained during the construction of \mathbf{G} later in this section. In equations (2.3.2) and (2.3.3), \mathbf{x}_0 is the source point, \mathbf{x} is the field point, and $u_i(\mathbf{x})$ represents the velocity field due to a concentrated point force of strength \mathbf{g} placed at \mathbf{x}_0 .

Taking the curl of the equation (2.3.2) yields

$$\omega_i(\mathbf{x}) = \frac{1}{8\pi\mu} \Omega_{ij}(\mathbf{x} - \mathbf{x}_0) g_j \quad \Omega_{ij} = \varepsilon_{ipl} \partial_p G_{lj} \quad (2.3.4)$$

where ε_{ipl} is the Levi-Civita epsilon and $\boldsymbol{\omega}$ is the vorticity tensor. Substituting equation (2.3.2) into equation (2.2.2) yields

$$\sigma_{ij} = -\frac{1}{8\pi} p_l \delta_{ij} g_l + \mu \left(\frac{1}{8\pi\mu} \frac{\partial G_{il}}{\partial x_j} + \frac{1}{8\pi\mu} \frac{\partial G_{jl}}{\partial x_i} \right) g_l,$$

which can be rewritten as

$$\sigma_{ij}(\mathbf{x}) = \frac{1}{8\pi} T_{ilj}(\mathbf{x} - \mathbf{x}_0) g_l, \quad (2.3.5)$$

where \mathbf{T} is the stress tensor and

$$T_{ilj}(\mathbf{x} - \mathbf{x}_0) = -\delta_{ij} p_l(\mathbf{x} - \mathbf{x}_0) + \frac{\partial G_{il}}{\partial x_j}(\mathbf{x} - \mathbf{x}_0) + \frac{\partial G_{jl}}{\partial x_i}(\mathbf{x} - \mathbf{x}_0). \quad (2.3.6)$$

To find the fundamental solution \mathbf{G} , the delta function is replaced by the equivalent expression as follows

$$\delta(\hat{\mathbf{x}}) = -\frac{1}{4\pi} \nabla^2 \left(\frac{1}{r} \right), \quad (2.3.7)$$

where $r = |\hat{\mathbf{x}}|$, and $\hat{\mathbf{x}} = \mathbf{x} - \mathbf{x}_0$. Using the equation (2.3.1), far away, where velocity vanishes, pressure is given as

$$p = \frac{1}{4\pi} \mathbf{g} \cdot \nabla \left(\frac{1}{r} \right). \quad (2.3.8)$$

Since the pressure is harmonic and equation (2.3.8) is a unique harmonic function ($\mathbf{x} \neq 0$) satisfying the boundary conditions, the equation (2.3.8) is given for pressure

in the whole domain. Substituting equation (2.3.7) and equation (2.3.8) into equation (2.3.1) yields

$$-\nabla \left(\frac{1}{4\pi} \mathbf{g} \cdot \nabla \left(\frac{1}{r} \right) \right) + \mu \nabla^2 \mathbf{u} + \mathbf{g} \left(-\frac{1}{4\pi} \nabla^2 \left(\frac{1}{r} \right) \right) = 0,$$

which can be further simplified as follows

$$\mu \nabla^2 \mathbf{u} = -\frac{1}{4\pi} \mathbf{g} \cdot (\nabla \nabla - I \nabla^2) \left(\frac{1}{r} \right), \quad (2.3.9)$$

where $\nabla \mathbf{F} = \partial_i F_j e_j \otimes e_i$.

Since the operator $(\nabla \nabla - I \nabla^2)$ is invertible, we can express the velocity in terms of a scalar function \mathbf{H}

$$\mathbf{u} = \frac{1}{\mu} \mathbf{g} \cdot (\nabla \nabla - I \nabla^2) \mathbf{H}. \quad (2.3.10)$$

Substituting equation (2.3.10) into equation (2.3.9) yields

$$\mu \nabla^2 \left(\frac{1}{\mu} \mathbf{g} \cdot (\nabla \nabla - I \nabla^2) \mathbf{H} \right) = -\frac{1}{4\pi} \mathbf{g} \cdot (\nabla \nabla - I \nabla^2) \left(\frac{1}{r} \right),$$

which simplifies to

$$(\nabla \nabla - I \nabla^2) \left(\nabla^2 \mathbf{H} + \frac{1}{4\pi r} \right) = 0. \quad (2.3.11)$$

Thus \mathbf{H} is the solution to Poisson's equation $\nabla^2 \mathbf{H} = -1/(4\pi r)$. Using equation (2.3.7) it can be seen that \mathbf{H} is the fundamental solution of biharmonic function $\nabla^4 \mathbf{H} = \delta(\hat{\mathbf{x}})$. One can check that

$$\mathbf{H} = -\frac{r}{8\pi}. \quad (2.3.12)$$

Substituting equation (2.3.12) into equation (2.3.10) yields

$$u_i(x) = \frac{1}{8\pi\mu} G_{ij}(\hat{\mathbf{x}}) g_j,$$

where $\mathbf{G} = (I \nabla^2 - \nabla \nabla) r$, which can be written as

$$G_{ij}(\hat{\mathbf{x}}) = \frac{\delta_{ij}}{r} + \frac{\hat{x}_i \hat{x}_j}{r^3}. \quad (2.3.13)$$

This is the Green's function for Stokes equations, also known as the Stokeslet. See Appendix (A) for the derivation of equation (2.3.13). The associated vorticity, pressure and stress tensor are

$$\Omega_{ij}(\hat{\mathbf{x}}) = \varepsilon_{ipl} \partial_p G_{lj} = 2\varepsilon_{ijl} \frac{\hat{\mathbf{x}}_l}{r^3} \quad (2.3.14)$$

$$p_i(\hat{\mathbf{x}}) = 2 \frac{\hat{\mathbf{x}}_i}{r^3}, \quad (2.3.15)$$

$$T_{ijk}(\hat{\mathbf{x}}) = -6 \frac{\hat{\mathbf{x}}_i \hat{\mathbf{x}}_j \hat{\mathbf{x}}_k}{r^5}. \quad (2.3.16)$$

See appendix A for details.

2.4 Lorenz Reciprocal Identity

In this section the Lorenz identity is derived. We define the modified stress tensor $\boldsymbol{\sigma}_{Mod}(\mathbf{x}) = \boldsymbol{\sigma}(\mathbf{x}) + \rho \mathbf{b} \cdot \mathbf{x}$ and modified pressure $p_{Mod}(\mathbf{x}) = p(\mathbf{x}) - \rho \mathbf{b} \cdot \mathbf{x}$. In these variables, the Stokes equations are

$$\nabla \cdot \boldsymbol{\sigma}_{Mod} = 0 \quad -\nabla p_{Mod} + \mu \nabla^2 \mathbf{u} = 0. \quad (2.4.1)$$

By assuming two separate Stokes flows with generated velocities \mathbf{u} and \mathbf{u}' and associated stress tensors $\boldsymbol{\sigma}_{Mod}$ and $\boldsymbol{\sigma}'_{Mod}$, the following equation can be derived. Since there already exist a superscript and a subscript, we drop the subscript "Mod".

$$\begin{aligned} 0 = u'_i \frac{\partial \sigma_{ij}}{\partial x_j} &= \frac{\partial}{\partial x_j} (u'_i \sigma_{ij}) - \sigma_{ij} \frac{\partial u'_i}{\partial x_j} \\ &= \frac{\partial}{\partial x_j} (u'_i \sigma_{ij}) - \left[-p \delta_{ij} + \mu \left(\frac{\partial u_i}{\partial x_j} + \frac{\partial u_j}{\partial x_i} \right) \right] \frac{\partial u'_i}{\partial x_j} \\ &= \frac{\partial}{\partial x_j} (u'_i \sigma_{ij}) - \mu \left(\frac{\partial u_i}{\partial x_j} + \frac{\partial u_j}{\partial x_i} \right) \frac{\partial u'_i}{\partial x_j}. \end{aligned} \quad (2.4.2)$$

In equation (2.4.2) the pressure term can be eliminated since $\delta_{ij} = 0$ when $i \neq j$ and from the continuity equation $p \nabla \cdot \mathbf{u} = 0$ when $i = j$. The same argument can be

made by interchanging \mathbf{u} and \mathbf{u}' , and thus

$$0 = u_i \frac{\partial \sigma'_{ij}}{\partial x_j} = \frac{\partial}{\partial x_j} (u_i \sigma'_{ij}) - \mu \left(\frac{\partial u'_i}{\partial x_j} + \frac{\partial u'_j}{\partial x_i} \right) \frac{\partial u_i}{\partial x_j}. \quad (2.4.3)$$

Subtracting equation (2.4.3) from equation (2.4.2) yields

$$\frac{\partial}{\partial x_j} (u'_i \sigma_{ij} - u_i \sigma'_{ij}) = u'_i \frac{\partial \sigma_{ij}}{\partial x_j} - u_i \frac{\partial \sigma'_{ij}}{\partial x_j} = 0. \quad (2.4.4)$$

Therefore, the reciprocal identity can be written as

$$\nabla \cdot (\mathbf{u}' \cdot \boldsymbol{\sigma}_{Mod} - \mathbf{u} \cdot \boldsymbol{\sigma}'_{Mod}) = 0. \quad (2.4.5)$$

2.5 Boundary Integral Formulation

The goal of this section is to derive a formula for the velocity of the interface bounding a drop in Stokes flow. The result will be a boundary integral representation of this velocity. The desired formula is obtained by first finding the velocities inside and outside of the drop, and then taking a limit from either side as the interface is approached.

We use the Lorenz identity where we let $\mathbf{u}', \boldsymbol{\sigma}'$ be the velocity and stress tensor associated with free space Greens's function

$$u'_i = \frac{1}{8\pi\mu} G_{ij}(\mathbf{x} - \mathbf{x}_0) g_j$$

and

$$\sigma'_{ik} = \frac{1}{8\pi} T_{ijk}(\mathbf{x} - \mathbf{x}_0) g_j$$

and $\mathbf{u}, \boldsymbol{\sigma}$ are the velocity and stress tensor of a stokes flow in a domain Ω . Then, by Lorenz,

$$\frac{\partial}{\partial x_k} [G_{ij}(\mathbf{x} - \mathbf{x}_0) \sigma_{ik}(\mathbf{x}) - \mu u_i(\mathbf{x}) T_{ijk}(\mathbf{x} - \mathbf{x}_0)] g_j = 0. \quad (2.5.1)$$

for any \mathbf{g} , and therefore,

$$\frac{\partial}{\partial x_k} [G_{ij}(\mathbf{x} - \mathbf{x}_0) \sigma_{ik}(\mathbf{x}) - \mu u_i(\mathbf{x}) T_{ijk}(\mathbf{x} - \mathbf{x}_0)] = 0. \quad (2.5.2)$$

We now select a control volume V in Ω which is bounded by a closed surface D .

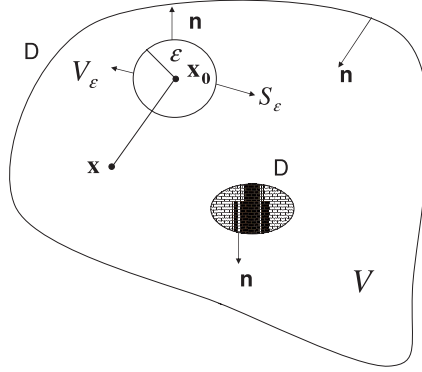


Figure 2.2: A control volume V within the domain of a flow bounded by the closed surface D . \mathbf{n} is the outward normal.

First we assume that \mathbf{x}_0 is outside of V . Integrating equation (2.5.2) over V , and using the divergence theorem to convert the volume integral into surface integral, we can obtain

$$\int_D [G_{ij}(\mathbf{x} - \mathbf{x}_0) \sigma_{ik}(\mathbf{x}) - \mu u_i(\mathbf{x}) T_{ijk}(\mathbf{x} - \mathbf{x}_0)] n_k(\mathbf{x}) dS(\mathbf{x}) = 0, \quad (2.5.3)$$

where the normal vector \mathbf{n} is directed into the control volume V . Now assume that \mathbf{x}_0 is in V . Let V_ϵ be a small sphere of radius ϵ centered on \mathbf{x}_0 as shown in figure 2.2. Integrating equation (2.5.2) over $V - V_\epsilon$ and using the divergence theorem, the following equation is obtained,

$$\int_{D, S_\epsilon} [G_{ij}(\mathbf{x} - \mathbf{x}_0) \sigma_{ik}(\mathbf{x}) - \mu u_i(\mathbf{x}) T_{ijk}(\mathbf{x} - \mathbf{x}_0)] n_k(\mathbf{x}) dS(\mathbf{x}) = 0, \quad (2.5.4)$$

Chapter 2. Governing Equations

where S_ε is the spherical surface enclosing V_ε . Let ε approaches zero over S_ε . Since G is free space Green's function and $\mathbf{n} = \hat{\mathbf{x}}/\varepsilon$ where $\hat{\mathbf{x}} = \mathbf{x} - \mathbf{x}_0$, it follows that,

$$\begin{aligned} & \int_D [G_{ij}(\mathbf{x} - \mathbf{x}_0) \sigma_{ik}(\mathbf{x}) - \mu u_i(\mathbf{x}) T_{ijk}(\mathbf{x} - \mathbf{x}_0)] n_k(\mathbf{x}) dS(\mathbf{x}) \\ &= - \int_{S_\varepsilon} \left[\left(\frac{\delta_{ij}}{\varepsilon} + \frac{\hat{x}_i \hat{x}_j}{\varepsilon^3} \right) \sigma_{ik}(\mathbf{x}) + 6\mu u_i(\mathbf{x}) \frac{\hat{x}_i \hat{x}_j \hat{x}_k}{\varepsilon^5} \right] n_k dS \end{aligned} \quad (2.5.5)$$

$$= - \int_{S_\varepsilon} \left[\left(\frac{\delta_{ij}}{\varepsilon} + \frac{\hat{x}_i \hat{x}_j}{\varepsilon^3} \right) \sigma_{ik}(\mathbf{x}) n_k + 6\mu u_i(\mathbf{x}) \frac{\hat{x}_i \hat{x}_j \varepsilon n_k \cdot n_k}{\varepsilon^5} \right] dS, \quad (2.5.6)$$

where $n_k \cdot n_k = \sum_k n_k^2 = |n_k|^2 = 1$. As epsilon approaches zero, the values of \mathbf{u} and $\boldsymbol{\sigma}$ over S_ε tend to $\mathbf{u}(\mathbf{x}_0)$ and $\boldsymbol{\sigma}(\mathbf{x}_0)$. Since δ_{ij} is Kronecker delta, $\left| \frac{\delta_{ij}}{\varepsilon} \right| < \frac{1}{\varepsilon}$. Also because $\hat{x}_i = \varepsilon n_i$ and $\hat{x}_j = \varepsilon n_j$, we have $\left| \frac{\hat{x}_i \hat{x}_j}{\varepsilon^3} \right| \leq \frac{1}{\varepsilon}$. Because $\boldsymbol{\sigma}$ is continuous, there exists an ε and M such that $\boldsymbol{\sigma}(\mathbf{x}) < M\boldsymbol{\sigma}(\mathbf{x}_0)$ for small enough ε . Thus

$$\left| \left(\frac{\delta_{ij}}{\varepsilon} + \frac{\hat{x}_i \hat{x}_j}{\varepsilon^3} \right) \sigma_{ik}(\mathbf{x}) n_k \varepsilon^2 \right| \leq \frac{2}{\varepsilon} 4\pi M \varepsilon^2 \boldsymbol{\sigma}(\mathbf{x}_0) = O(\varepsilon) \rightarrow 0$$

as $\varepsilon \rightarrow 0$. Therefore,

$$\begin{aligned} & \int_D [G_{ij}(\mathbf{x} - \mathbf{x}_0) \sigma_{ik}(\mathbf{x}) - \mu u_i(\mathbf{x}) T_{ijk}(\mathbf{x} - \mathbf{x}_0)] n_k(\mathbf{x}) dS(\mathbf{x}) \\ &= -6\mu u_i(\mathbf{x}_0) \frac{1}{\varepsilon^4} \int_{S_\varepsilon} \hat{x}_i \hat{x}_j dS(\mathbf{x}). \end{aligned} \quad (2.5.7)$$

Using the divergence theorem $\int_V (\nabla \cdot \mathbf{F}) dV = \int_S (\mathbf{F} \cdot \mathbf{n}) dS$ where $\mathbf{F} = \hat{x}_i$, we obtain

$$\int_{S_\varepsilon} \hat{x}_i \hat{x}_j dS(\mathbf{x}) = \varepsilon \int_{S_\varepsilon} \hat{x}_i n_j dS(\mathbf{x}) = \varepsilon \int_{V_\varepsilon} \frac{\partial \hat{x}_i}{\partial \hat{x}_j} dV(\mathbf{x}) = \delta_{ij} \frac{4}{3} \pi \varepsilon^4. \quad (2.5.8)$$

Substituting equation (2.5.8) into equation (2.5.7) yields

$$\begin{aligned} & \int_D [G_{ij}(\mathbf{x} - \mathbf{x}_0) \sigma_{ik}(\mathbf{x}) - \mu u_i(\mathbf{x}) T_{ijk}(\mathbf{x} - \mathbf{x}_0)] n_k(\mathbf{x}) dS(\mathbf{x}) \\ &= -8\pi \mu u_j(\mathbf{x}_0). \end{aligned} \quad (2.5.9)$$

Therefore the equation above can be simplified as

$$u_j(\mathbf{x}_0) = -\frac{1}{8\pi\mu} \int_D \sigma_{ik}(\mathbf{x}) n_k(\mathbf{x}) G_{ij}(\mathbf{x} - \mathbf{x}_0) dS(\mathbf{x})$$

$$+\frac{1}{8\pi}\int_D u_i(\mathbf{x}) T_{ijk}(\mathbf{x}-\mathbf{x}_0) n_k(\mathbf{x}) dS(\mathbf{x}). \quad (2.5.10)$$

The first term is similar to the potential of a single point charge and since T in the second term is given in terms of the derivatives of G , it is similar to the potential of a double layer charge. For this reasoning, the first term on the right-hand side is called single-layer potential and the second distribution is called double-layer potential.

Now, the goal is to compute the limit of double-layer potential as the point \mathbf{x}_0 approaches the boundary D either from the internal or external side. Since the boundary D is of class C_2 and the velocity varies in a continuous manner, using theorem 6.17 in [30],

$$\begin{aligned} & \lim_{\mathbf{x}_0 \rightarrow D} \int_D u_i(\mathbf{x}) T_{ijk}(\mathbf{x}-\mathbf{x}_0) n_k(\mathbf{x}) dS(\mathbf{x}) \\ &= \pm 4\pi u_j(\mathbf{x}_0) + pv \int_D u_i(\mathbf{x}) T_{ijk}(\mathbf{x}-\mathbf{x}_0) n_k(\mathbf{x}) dS(\mathbf{x}). \end{aligned} \quad (2.5.11)$$

The plus sign represents that the point \mathbf{x}_0 approaches D from outside of the flow and minus sign otherwise. The symbol pv indicates the principal value of the double layer potential. Substituting equation (2.5.11) into equation (2.5.10) with the plus sign, for a point \mathbf{x}_0 which is on the boundary D , yields

$$\begin{aligned} u_j(\mathbf{x}_0) &= -\frac{1}{8\pi\mu} \int_D \sigma_{ik}(\mathbf{x}) n_k(\mathbf{x}) G_{ij}(\mathbf{x}-\mathbf{x}_0) dS(x) \\ &+ \frac{1}{8\pi} \left[4\pi u_j(\mathbf{x}_0) + pv \int_D u_i(\mathbf{x}) T_{ijk}(\mathbf{x}-\mathbf{x}_0) n_k(\mathbf{x}) dS(\mathbf{x}) \right], \end{aligned} \quad (2.5.12)$$

which simplifies as

$$\begin{aligned} u_j(\mathbf{x}_0) &= -\frac{1}{4\pi\mu} \int_D \sigma_{ik}(\mathbf{x}) n_k(\mathbf{x}) G_{ij}(\mathbf{x}-\mathbf{x}_0) dS(x) \\ &+ \frac{1}{4\pi} pv \int_D u_i(\mathbf{x}) T_{ijk}(\mathbf{x}-\mathbf{x}_0) n_k(\mathbf{x}) dS(\mathbf{x}). \end{aligned} \quad (2.5.13)$$

By considering the body force $\mathbf{f} = \boldsymbol{\sigma} \cdot \mathbf{n}$ and identifying the boundary D with the interface S , equation (2.5.9) can be written as

$$u_j^{(1)}(\mathbf{x}_0) = -\frac{1}{8\pi\mu_1} \int_S f_i^{(1)} G_{ij}(\mathbf{x}-\mathbf{x}_0) dS(x) + \frac{1}{8\pi} \int_S u_i(\mathbf{x}) T_{ijk}(\mathbf{x}-\mathbf{x}_0) n_k(\mathbf{x}) dS(\mathbf{x}).$$

$$(2.5.14)$$

The superscript ⁽¹⁾ indicates the surface force over the external side of S . By applying the reciprocal identity equation (2.5.2) for the internal flow $\mathbf{u}^{(2)}$ at a point \mathbf{x}_0 , we can write

$$\int_S f_i^{(2)}(\mathbf{x}) G_{ij}(\mathbf{x} - \mathbf{x}_0) dS(\mathbf{x}) - \mu_2 \int_S u_i(\mathbf{x}) T_{ijk}(\mathbf{x} - \mathbf{x}_0) n_k(\mathbf{x}) dS(\mathbf{x}) = 0. \quad (2.5.15)$$

Multiplying equation (2.5.15) by $\frac{-1}{8\pi\mu_1}$ and subtracting from equation (2.5.14), yields

$$\begin{aligned} u_j^{(1)}(\mathbf{x}_0) &= \frac{-1}{8\pi\mu_1} \int_S \Delta f_i(\mathbf{x}) G_{ij}(\mathbf{x} - \mathbf{x}_0) dS(x) \\ &+ \frac{1}{8\pi} \left(1 - \frac{\mu_2}{\mu_1}\right) \int_S u_i(\mathbf{x}) T_{ijk}(\mathbf{x} - \mathbf{x}_0) n_k(\mathbf{x}) dS(\mathbf{x}). \end{aligned} \quad (2.5.16)$$

Considering that the velocity at infinity is \mathbf{u}^∞ then $u_j^{(1)}(\mathbf{x}_0)$ is given by

$$\begin{aligned} u_j^{(1)}(\mathbf{x}_0) &= u_j^\infty(\mathbf{x}_0) + \frac{-1}{8\pi\mu_1} \int_S \Delta f_i(\mathbf{x}) G_{ij}(\mathbf{x} - \mathbf{x}_0) dS(x) \\ &+ \frac{1-\lambda}{8\pi} \int_S u_i(\mathbf{x}) T_{ijk}(\mathbf{x} - \mathbf{x}_0) n_k(\mathbf{x}) dS(\mathbf{x}), \end{aligned} \quad (2.5.17)$$

where $\lambda = \mu_2/\mu_1$ and $\Delta \mathbf{f}$ is the discontinuity in the interfacial surface force as follows

$$\Delta \mathbf{f} = \mathbf{f}^{(1)} - \mathbf{f}^{(2)} = (\boldsymbol{\sigma}^{(1)} - \boldsymbol{\sigma}^{(2)}) \cdot \mathbf{n}.$$

Next, we seek to derive a boundary integral representation for the internal flow

$$\begin{aligned} u_j^{(2)}(\mathbf{x}_0) &= \frac{1}{8\pi\mu_2} \int_S f_i^{(2)} G_{ij}(\mathbf{x} - \mathbf{x}_0) dS(x) \\ &- \frac{1}{8\pi} \int_S u_i(\mathbf{x}) T_{ijk}(\mathbf{x} - \mathbf{x}_0) n_k(\mathbf{x}) dS(\mathbf{x}), \end{aligned} \quad (2.5.18)$$

and the reciprocal relation for the external fluid results in

$$\int_S f_i^{(1)}(\mathbf{x}) G_{ij}(\mathbf{x} - \mathbf{x}_0) dS(\mathbf{x}) - \mu_1 \int_S u_i(\mathbf{x}) T_{ijk}(\mathbf{x} - \mathbf{x}_0) n_k(\mathbf{x}) dS(\mathbf{x}) = 0. \quad (2.5.19)$$

Multiplying equation (2.5.19) by $\frac{-1}{8\pi\mu_2}$ and subtracting from equation (2.5.18) yields

$$\begin{aligned} u_j^{(2)}(\mathbf{x}_0) &= \frac{-1}{8\pi\mu_1\lambda} \int_S \Delta f_i(\mathbf{x}) G_{ij}(\mathbf{x} - \mathbf{x}_0) dS(x) \\ &+ \frac{1}{8\pi} \left(\frac{\mu_1}{\mu_2} - 1 \right) \int_S u_i(\mathbf{x}) T_{ijk}(\mathbf{x} - \mathbf{x}_0) n_k(\mathbf{x}) dS(\mathbf{x}). \end{aligned} \quad (2.5.20)$$

Considering the contribution of \mathbf{u}^∞ , equation (2.5.20) can be written in the following form

$$\begin{aligned} u_j^{(2)}(\mathbf{x}_0) &= u_j^\infty(\mathbf{x}_0) + \frac{-1}{8\pi\mu_1\lambda} \int_S \Delta f_i(\mathbf{x}) G_{ij}(\mathbf{x} - \mathbf{x}_0) dS(x) \\ &+ \frac{1-\lambda}{8\pi\lambda} \int_S u_i(\mathbf{x}) T_{ijk}(\mathbf{x} - \mathbf{x}_0) n_k(\mathbf{x}) dS(\mathbf{x}). \end{aligned} \quad (2.5.21)$$

Now letting the point \mathbf{x}_0 approach the interface, we obtain

$$\begin{aligned} u_j^{(1)}(\mathbf{x}_0) &= u_j^\infty(\mathbf{x}_0) + \frac{-1}{8\pi\mu_1} \int_S \Delta f_i(\mathbf{x}) G_{ij}(\mathbf{x} - \mathbf{x}_0) dS(x) \\ &+ \frac{1-\lambda}{8\pi} \left(4\pi u_j^{(1)}(\mathbf{x}_0) + pv \int_S u_i(\mathbf{x}) T_{ijk}(\mathbf{x} - \mathbf{x}_0) n_k(\mathbf{x}) dS(\mathbf{x}) \right), \end{aligned} \quad (2.5.22)$$

which can be simplified as

$$\begin{aligned} u_j^{(1)}(\mathbf{x}_0) &= \frac{2}{1+\lambda} u_j^\infty(\mathbf{x}_0) + \frac{-1}{4\pi\mu_1(1+\lambda)} \int_S \Delta f_i(\mathbf{x}) G_{ij}(\mathbf{x} - \mathbf{x}_0) dS(x) \\ &+ \frac{1}{4\pi} \frac{1-\lambda}{1+\lambda} pv \int_S u_i(\mathbf{x}) T_{ijk}(\mathbf{x} - \mathbf{x}_0) n_k(\mathbf{x}) dS(\mathbf{x}). \end{aligned} \quad (2.5.23)$$

Since the contribution of outer flow is u_∞/λ (See Appendix B for the derivation), similarly for the internal flow we obtain,

$$\begin{aligned} u_j^{(2)}(\mathbf{x}_0) &= \frac{2}{1+\lambda} u_j^\infty(\mathbf{x}_0) + \frac{-1}{4\pi\mu_1(1+\lambda)} \int_S \Delta f_i(\mathbf{x}) G_{ij}(\mathbf{x} - \mathbf{x}_0) dS(x) \\ &+ \frac{1}{4\pi} \frac{1-\lambda}{1+\lambda} pv \int_S u_i(\mathbf{x}) T_{ijk}(\mathbf{x} - \mathbf{x}_0) n_k(\mathbf{x}) dS(\mathbf{x}). \end{aligned} \quad (2.5.24)$$

Finally, the velocity on the interface can be computed as the average between two fluid velocities on each side [11]

$$u_j(\mathbf{x}_0) = \frac{2}{1+\lambda} u_j^\infty(\mathbf{x}_0) + \frac{-1}{4\pi\mu_1(1+\lambda)} \int_S \Delta f_i(\mathbf{x}) G_{ij}(\mathbf{x} - \mathbf{x}_0) dS(x)$$

$$+ \frac{1}{4\pi} \frac{1-\lambda}{1+\lambda} pv \int_S u_i(\mathbf{x}) T_{ijk}(\mathbf{x} - \mathbf{x}_0) n_k(\mathbf{x}) dS(\mathbf{x}). \quad (2.5.25)$$

Therefore the velocity component u_j at a point \mathbf{x}_0 can be written as

$$u_j(\mathbf{x}_0) = \frac{2}{1+\lambda} u_j^\infty(\mathbf{x}_0) - \frac{\gamma}{\mu_1(1+\lambda)} u_j^s(\mathbf{x}_0) + \frac{1-\lambda}{1+\lambda} u_j^d(\mathbf{x}_0), \quad (2.5.26)$$

where

$$u_j^s(\mathbf{x}_0) = \frac{1}{4\pi} \int_S G_{ij}(\mathbf{x} - \mathbf{x}_0) n_i(\mathbf{x}) \kappa(\mathbf{x}) dS(x), \quad (2.5.27)$$

$$u_j^d(\mathbf{x}_0) = \frac{1}{4\pi} pv \int_S u_i(\mathbf{x}) T_{ijk}(\mathbf{x} - \mathbf{x}_0) n_k(\mathbf{x}) dS(\mathbf{x}), \quad (2.5.28)$$

for $j = 1, 2, 3$. Here κ is the total curvature, γ is the surface tension and $[\boldsymbol{\sigma} \cdot \mathbf{n}]_D = 2\kappa_m \gamma \mathbf{n} = \nabla \cdot \mathbf{n} \gamma \mathbf{n}$. Also $\kappa = 2\kappa_m = \nabla \cdot \mathbf{n}$, where κ_m is the mean curvature and $[\cdot]_D$ indicates the jump condition from the outside to the inside of the drop.

2.6 Non-dimensionalization

At this point, it is convenient to use dimensionless equations. Thereby equation (2.5.26) can be non-dimensionalized using the radius of initial drop R as the characteristic length, γ/μ_1 as the characteristic velocity U , $R\mu_1/\gamma$ as the characteristic time T . Also

$$[|u^\infty|] = [RG]$$

where G is the magnitude of the rate of strain of the external field \mathbf{u}^∞ .

2.6.1 Non-zero Surface Tension, $\gamma > 0$

By changing variables $u' = \frac{u}{U}$, $x' = \frac{x}{R}$, $t' = \frac{t}{T}$ we obtain,

$$u_j(\mathbf{x}_0) = \frac{\gamma}{\mu} u_j'(\mathbf{x}_0), \quad u_j^\infty(\mathbf{x}_0) = RG u_j'^\infty(\mathbf{x}_0).$$

Therefore the dimensionless equation can be written as

$$\frac{\gamma}{\mu_1} u'_j(\mathbf{x}_0) = \frac{2RG}{1+\lambda} u_j'^{\infty}(\mathbf{x}_0) - \frac{\gamma}{\mu_1(1+\lambda)} u_j^s(\mathbf{x}_0) + \frac{1-\lambda}{1+\lambda} u_j^d(\mathbf{x}_0),$$

where

$$u_j^s(\mathbf{x}_0) = \frac{1}{4\pi} \int_S G_{ij}(\mathbf{x} - \mathbf{x}_0) n_i(\mathbf{x}) \kappa(\mathbf{x}) dS(x),$$

$$u_j^d(\mathbf{x}_0) = \frac{\gamma}{\mu_1} \frac{1}{4\pi} pv \int_S u'_i(\mathbf{x}) T_{ijk}(\mathbf{x} - \mathbf{x}_0) n_k(\mathbf{x}) dS(\mathbf{x}).$$

In single layer integral, G and κ both have units of $1/m$ that is canceled by the unit of dS which is m^2 . Also in the second layer integral, the unit of T is $1/m^2$ that is canceled with the unit of dS . The above equation can be simplified as

$$u_j(\mathbf{x}_0) = \frac{2Ca}{1+\lambda} u_j^{\infty}(\mathbf{x}_0) - \frac{1}{(1+\lambda)} u_j^s(\mathbf{x}_0) + \frac{1-\lambda}{1+\lambda} u_j^d(\mathbf{x}_0), \quad (2.6.1)$$

where

$$u_j^s(\mathbf{x}_0) = \frac{1}{4\pi} \int_S G_{ij}(\mathbf{x} - \mathbf{x}_0) n_i(\mathbf{x}) \kappa(\mathbf{x}) dS(x), \quad (2.6.2)$$

$$u_j^d(\mathbf{x}_0) = \frac{1}{4\pi} pv \int_S u_i(\mathbf{x}) T_{ijk}(\mathbf{x} - \mathbf{x}_0) n_k(\mathbf{x}) dS(\mathbf{x}). \quad (2.6.3)$$

$Ca = RG\mu_1/\gamma$ is the capillary number which defines the measure of the viscous forces relative to the surface tension.

In the case of having several drops in the flow, the total velocity is the sum of self-induced velocity of the drop, the externally-induced velocities of the other drops, and the outer velocity. Considering the case of having two drops, the velocity equation can be written as

$$u_j(\mathbf{x}_0) = \frac{2}{1+\lambda} \tilde{u}_j^{\infty}(\mathbf{x}_0) - \frac{\gamma}{\mu_1(1+\lambda)} u_j^s(\mathbf{x}_0) + \frac{1-\lambda}{1+\lambda} u_j^d(\mathbf{x}_0), \quad (2.6.4)$$

where $\tilde{u}^{\infty} = u^{\infty} + u_o^{(1)}$, and $u_o^{(1)}$ is the velocity that the outer drop induces on the main drop (the main drop refers to the drop which its total velocity is the point of interest). Using equation (2.5.16), $u_o^{(1)}$ can be written as

$$u_{oj}^{(1)}(\mathbf{x}_0) = \frac{-1}{8\pi\mu_1} \int_S \Delta f_i(\mathbf{x}) G_{ij}(\mathbf{x} - \mathbf{x}_0) dS(x)$$

$$+\frac{1-\lambda}{8\pi} \int_S u_{oi}(\mathbf{x}) T_{ijk}(\mathbf{x}-\mathbf{x}_0) n_k(\mathbf{x}) dS, \quad (2.6.5)$$

which can be rearranged as

$$u_{oj}^{(1)}(\mathbf{x}_0) = \frac{-\gamma}{2\mu_1} u_o^s(\mathbf{x}_0) + \frac{1-\lambda}{2} u_o^d(\mathbf{x}_0), \quad (2.6.6)$$

where

$$u_{oj}^s(\mathbf{x}_0) = \frac{1}{4\pi} \int_S G_{ij}(\mathbf{x}-\mathbf{x}_0) n_i(\mathbf{x}) \kappa(\mathbf{x}) dS(x), \quad (2.6.7)$$

$$u_{oj}^d(\mathbf{x}_0) = \frac{1}{4\pi} \int_S u_i(\mathbf{x}) T_{ijk}(\mathbf{x}-\mathbf{x}_0) n_k(\mathbf{x}) dS(\mathbf{x}). \quad (2.6.8)$$

Thus the dimensionless equation can be written as follows

$$u_j(\mathbf{x}_0) = \frac{2Ca}{1+\lambda} u_j^\infty(\mathbf{x}_0) - \frac{1}{1+\lambda} u_{oj}^s(\mathbf{x}_0) + \frac{1-\lambda}{1+\lambda} u_{oj}^d(\mathbf{x}_0) - \frac{1}{1+\lambda} u_j^s(\mathbf{x}_0) + \frac{1-\lambda}{1+\lambda} u_j^d(\mathbf{x}_0). \quad (2.6.9)$$

2.6.2 Zero Surface Tension, $\gamma = 0$

When $\gamma = 0$, the velocity equation (2.5.26) can be written as

$$u_j(\mathbf{x}_0) = \frac{2}{1+\lambda} u_j^\infty(\mathbf{x}_0) + \frac{1-\lambda}{1+\lambda} u_j^d(\mathbf{x}_0), \quad (2.6.10)$$

where

$$u_j^d(\mathbf{x}_0) = \frac{1}{4\pi} pv \int_S u_i(\mathbf{x}) T_{ijk}(\mathbf{x}-\mathbf{x}_0) n_k(\mathbf{x}) dS(\mathbf{x}).$$

To derive the dimensionless equation, GR is used as the characteristic velocity, R as the characteristic length and $1/G$ as the characteristic time. Doing so yields the dimensionless equation as follows

$$GRu_j'(\mathbf{x}_0) = GR \frac{2}{1+\lambda} u_j'^\infty(\mathbf{x}_0) + \frac{1-\lambda}{1+\lambda} u_j'^d(\mathbf{x}_0),$$

$$u_j'^d(\mathbf{x}_0) = GR \frac{1}{4\pi} pv \int_S u_i'(\mathbf{x}) T_{ijk}(\mathbf{x}-\mathbf{x}_0) n_k(\mathbf{x}) dS(\mathbf{x}).$$

Chapter 2. Governing Equations

Dividing each side by GR , the dimensionless equation can be written as

$$u_j(\mathbf{x}_0) = \frac{2}{1+\lambda} u_j^\infty(\mathbf{x}_0) + \frac{1-\lambda}{1+\lambda} u_j^d(\mathbf{x}_0), \quad (2.6.11)$$

where

$$u_j^d(\mathbf{x}_0) = \frac{1}{4\pi} pv \int_S u_i(\mathbf{x}) T_{ijk}(\mathbf{x} - \mathbf{x}_0) n_k(\mathbf{x}) dS(\mathbf{x}). \quad (2.6.12)$$

Chapter 3

Numerical Approach

3.1 Discretization and Initial Conditions

To move the drop, we need to solve the equation,

$$\frac{\partial \mathbf{x}}{\partial t} = \mathbf{u}(\mathbf{x}, t)$$

on the curve C shown in figure 3.1(a), with initial conditions $\mathbf{x}(\alpha, 0) = \mathbf{x}_0(\alpha)$. Curve C is parameterized as follows

$$C : (x(\alpha, t), y(\alpha, t)), 0 \leq \alpha \leq \pi.$$

To numerically solve this equation, the curve C is discretized using $n + 1$ points (x_j, y_j) , $j = 0, 1, \dots, n$ as shown in figure 3.1(b). Let the Lagrangian particles be $\alpha_j = j\pi/n$ for $j = 0, \dots, n$, and the coordinates of computational points to be given as $x_j(t)$ and $y_j(t)$ which approximate $x(\alpha_j, t)$ and $y(\alpha_j, t)$. y and x are the axial and radial coordinates, respectively. The velocity of the interface is calculated at each point (x_j, y_j) . The system that is solved numerically is

$$\frac{dx_j}{dt} = u(x_j, y_j, t) \qquad \frac{dy_j}{dt} = v(x_j, y_j, t) \qquad (3.1.1)$$

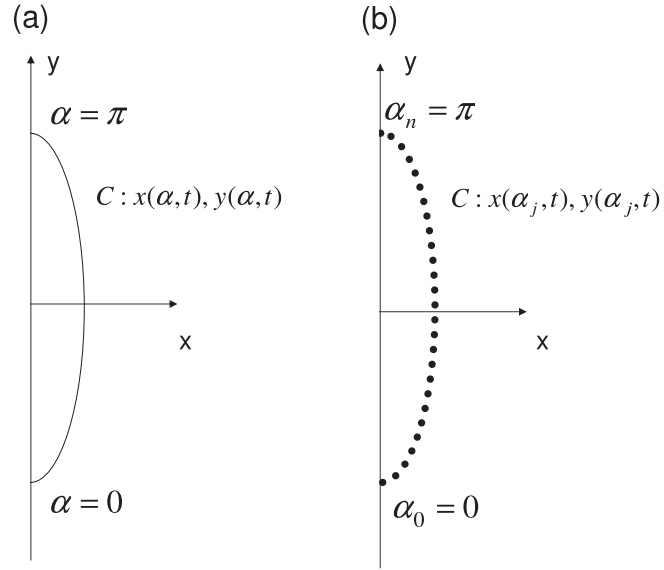


Figure 3.1: (a) Curve C representing the surface of the drop with poles $\alpha = 0$ and $\alpha = \pi$ (b) Discretized curve.

The initial condition is chosen to be a unit sphere, thus $x_j(0) = \cos(\alpha)$ and $y_j(0) = \sin(\alpha)$.

3.2 Evaluating Particle Velocity

In this section, it is shown how the velocity $u(x_j, t)$ in equation (3.1.1) is evaluated. In the case of axisymmetric flows the integration with respect to the angular variable ϕ (shown in figure 3.2) reduces the boundary integrals to line integrals over a curve C . Therefore the single and double layer velocities described in equations (2.5.27) and (2.5.28) reduce to

$$u^s(\alpha_j, t) = \frac{1}{4\pi} \int_0^\pi H^{us}(\alpha, \alpha_j, t) \kappa(\alpha, t) d\alpha \quad (3.2.1)$$

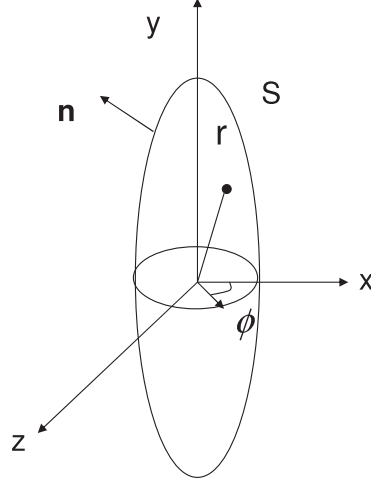


Figure 3.2: Axisymmetric surface S , axis of symmetry y , azimuthal angle ϕ and outward normal vector \mathbf{n} .

$$v^s(\alpha_j, t) = \frac{1}{4\pi} \int_0^\pi H^{vs}(\alpha, \alpha_j, t) \kappa(\alpha, t) d\alpha \quad (3.2.2)$$

$$u^d(\alpha_j, t) = \frac{1}{4\pi} \int_0^\pi H_1^{ud}(\alpha, \alpha_j, t) u(\alpha, t) + H_2^{ud}(\alpha, \alpha_j, t) v(\alpha, t) d\alpha \quad (3.2.3)$$

$$v^d(\alpha_j, t) = \frac{1}{4\pi} \int_0^\pi H_1^{vd}(\alpha, \alpha_j, t) u(\alpha, t) + H_2^{vd}(\alpha, \alpha_j, t) v(\alpha, t) d\alpha, \quad (3.2.4)$$

where

$$H^s(\alpha, \alpha_j, t) = M_1(x, x_j, y - y_j) \dot{y}(\alpha, t) - M_2(x, x_j, y, y_j) \dot{x}(\alpha, t) \quad (3.2.5)$$

$$H_l^d(\alpha, \alpha_j, t) = Q_{l1}(x, x_j, y - y_j) \dot{y}(\alpha, t) - Q_{l2}(x, x_j, y, y_j) \dot{x}(\alpha, t) \quad (3.2.6)$$

and $l = 1, 2$. The velocity at a point $\alpha = \alpha_j$ is $\mathbf{u}(\alpha_j, t) = (u(\alpha_j, t), v(\alpha_j, t))$ where u, v are the radial and axial velocities. Here $x = x(\alpha, t)$, $y = y(\alpha, t)$, $x_j = x(\alpha_j, t)$, $y_j = y(\alpha_j, t)$ and the dot stands for differentiation with respect to α . The functions

M and Q are provided in [1] and the curvature κ is given by

$$\kappa = \frac{\dot{y}}{x\sqrt{\dot{x}^2 + \dot{y}^2}} + \frac{\dot{x}\ddot{y} - \dot{y}\ddot{x}}{(\dot{x}^2 + \dot{y}^2)^{3/2}}$$

3.2.1 Quadrature Rules For Integrals

In this study, it is assumed that the surface intersects the axis of symmetry with the endpoints $\alpha = 0$ and π , which also correspond to the poles where $x = 0$. The integrands in equations (3.2.1), (3.2.3), (3.2.2) and (3.2.4) are a function G of variables α, α_j and t . Using expansions of the complete elliptic integrals about the poles and using Mathematica, it is shown that [1]

$$G(\alpha, \alpha_j, t) = \tilde{G}(\alpha, \alpha_j, t) + \sum_{k=0}^{\infty} c_k (\alpha - \alpha_j)^k \log |\alpha - \alpha_j|, \quad (3.2.7)$$

where \tilde{G} is smooth. The double layer is more regular than the single layer since $c_0 = 0$. A common approach used in previous studies is to desingularize the single layer using the identity $\int_0^\pi H^s(\alpha, \alpha_j, t) d\alpha = 0$. Using this identity equation, equations (3.2.1) and (3.2.2) can be rewritten as

$$\begin{aligned} u^s(\alpha_j, t) &= \frac{1}{4\pi} \int_0^\pi H^{us}(\alpha, \alpha_j, t) (\kappa(\alpha, t) - \kappa(\alpha_j, t)) d\alpha \\ v^s(\alpha_j, t) &= \frac{1}{4\pi} \int_0^\pi H^{vs}(\alpha, \alpha_j, t) (\kappa(\alpha, t) - \kappa(\alpha_j, t)) d\alpha \end{aligned} \quad (3.2.8)$$

This removes the leading order singular term which means $c_0 = 0$ for the integrands in equation (3.2.8). The integrals in equation (3.2.7) can be approximated to any arbitrary order using the quadrature rule introduced by Sidi and Israeli [31] as follows,

$$\begin{aligned} \int_a^b G(\alpha, \alpha_j, t) d\alpha &= h \sum_{\substack{k=0 \\ k \neq j}}^n G(\alpha_k, \alpha_j, t) + h\tilde{G}(\alpha_j, \alpha_j, t) + c_0(\alpha_j, t)h \log \frac{h}{2\pi} \\ &+ \sum_{\substack{k=2 \\ k \text{ even}}}^m \nu_k c_k(\alpha_j, t) h^{k+1} + \sum_{\substack{k=2 \\ k \text{ odd}}}^m \gamma_k \left[\frac{\partial^k G}{\partial \alpha^k}(b, \alpha_j, t) - \frac{\partial^k G}{\partial \alpha^k}(a, \alpha_j, t) \right] h^{k+1} \end{aligned}$$

$$= O(h^{m+2}) \tag{3.2.9}$$

where m is any integer greater or equal to zero. $\alpha_k = a + kh$, $k = 0, \dots, n$ and $h = (b-a)/n$. The symbol " indicates that the first and last summands are weighted by $1/2$. The constants required for a fifth-order method used in this dissertation are $\gamma_1 = -1/12$, $\gamma_3 = -1/720$, and $\nu = -0.06089691411678654156\dots$. Since all c_k and derivatives depend on α_j and t , the order of convergence is pointwise. Nitsche et al. [1] found that this method suffers from a round-off error caused by digit cancelation. They resolved this problem by extracting the singular part of the equation and recombining the singular terms to reduce the digit cancelation. They also found that the error increases near the poles due to the unbounded behavior of the derivatives of G at the poles and the coefficients c_k . They achieved a uniformly fifth-order approximation by finding a pole correction. A good approximation B of G is found such that it captures the singular behavior of G at the poles using Taylor expansions. Next, they used B to write

$$\int G = \int (G - B) + \int B \tag{3.2.10}$$

where $G-B$ is less singular than G . The integral of B can be essentially pre-computed at minimal cost per timestep. The result is a uniform fifth-order quadrature.

3.2.2 Finding \mathbf{u} and \mathbf{v} , $\lambda > 0$, $\lambda \neq 1$

If $\lambda \neq 1$, the double layer contributions given in equations (3.2.3) and (3.2.4) form a coupled system of Fredholm integral equations of the second type. The Fredholm integral equation is solved for \mathbf{u} using GMRES [32] with a prescribed residual tolerance of 10^{-13} . This method converges in four iterations for $\lambda = 100$, five iterations for $\lambda = 10$ and six iterations for $\lambda = 0.01$ and $\lambda = 0$. When $\lambda = 1$, there is no contribution of the double layer integral to the velocity component.

The Case of $\lambda > 0$

Equation (2.6.1) that we are solving for the velocity is in the form $\mathbf{u} = \mathbf{u}_d + \mathbf{U} = A\mathbf{u} + \mathbf{U}$ or $(A - I)\mathbf{u} = -\mathbf{U}$ where $\mathbf{U} = \mathbf{u}_\infty + \mathbf{u}^s$ and $A = 1/4\pi\rho v \int_S (\mathbf{T} \cdot \mathbf{n})_{ij} (\mathbf{x} - \mathbf{x}_0) dS(\mathbf{x})$. The eigenvalues corresponding to the matrix A are all smaller than one and $A - I$ is an invertible matrix which enables us to solve the equations using iterative methods.

The Case of $\lambda = 0$

In the case of inviscid bubble $\lambda = 0$, the matrix A has an eigenvalue of $\beta = 1$. Therefore $A - I$ is a singular matrix and any iterative method used to solve \mathbf{u}^d diverges. By Wielandt's theorem [33], we use the modified matrix that has the same eigenvalues as A with the exception of $\beta = 1$. This becomes possible by replacing the kernel $(\mathbf{T} \cdot \mathbf{n})_{ij}$ in the equation of \mathbf{u}^d by $(T(\mathbf{x} - \mathbf{x}_0) \cdot \mathbf{n}(\mathbf{x}_0))_{ij} + Cn_i(\mathbf{x})n_j(\mathbf{x}_0)$ where C is an arbitrary constant. This replacement enforces the volume conservation $\int_S \mathbf{u} \cdot \mathbf{n} dS = 0$

3.3 Evolving Cartesian Coordinates

Using the system of ordinary differential equations (3.1.1), the positions of the computational points are computed using a fourth-order Runge-Kutta method. If this system is solved in the Cartesian coordinates, the Lagrangian particles accumulate near the isolated points. In certain cases, these accumulations cause numerical instabilities. This method is used where $Ca = \infty$ which occurs in the absence of surface tension. In this particular case, the drop evolves very fast in time and therefore the accumulation of Lagrangian points does not cause any instabilities.

3.4 Evolving Arclength-Angle Coordinates

Due to the instabilities that the use of Cartesian coordinates causes, an arclength-angle formulation is used for $Ca < \infty$. In this formulation the variables tangent

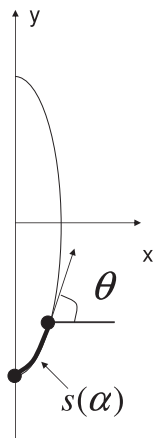


Figure 3.3: Tangent angle $\theta(\alpha, t)$, and the arc-length $s(\alpha)$

angle $\theta(\alpha, t)$ and the relative spacing between the points s_α are used as shown in figure 3.3, where $s(\alpha, t)$ is the arc-length.

3.4.1 Equal Arclength

In this section the aim is to develop a method in which the computational particles remain equally spaced. The Lagrangian particles α are used to track the interface which can be determined by the normal velocity. Note that the tangential velocity only determines the position of the marker points. Therefore the interface is obtained by

$$\frac{\partial \mathbf{x}}{\partial t} = \mathbf{u} + T\mathbf{s}, \quad (3.4.1)$$

where $\mathbf{s}(\alpha, t)$ is the unit tangent vector, and $T(\alpha, t)$ is an arbitrarily function. Following Hou et al. [34], T is chosen such that the position of Lagrangian marker particles can be controlled. To solve the rounded shape drops or the shapes with low curvatures, T is chosen such that the particles remain equally spaced in the arc-length. Alternative values of $T(\alpha, t)$ are chosen for the case of high curvature and pinch-off which later is explained in section 3.4.1. The sheet is described by a curve in the symmetry plane, $X(\alpha, t) = (x(\alpha, t), y(\alpha, t))$, $\alpha \in [0, \pi]$, where the y -axis is the symmetry axis, x is the radial direction, and α is a Lagrangian parameter that remains constant for computational particles in time. Equation (3.4.1) can be rewritten in terms of the tangent angle $\theta(\alpha, t)$ and the relative spacing between points s_α , where $s(\alpha, t)$ is the arc-length. The subscripts α and t represent the partial differentiation with respect to that variable. θ and s_α are related to x and y by

$$x_\alpha = s_\alpha \cos\theta, \quad y_\alpha = s_\alpha \sin\theta, \quad (3.4.2)$$

where $x(0, t) = 0$ and $y(0, t) = y_0(t)$. In the case where the arc-lengths are equal, the spacing between the points are constant in α , and thus $s_\alpha = L(t)/\pi$, where L is the length of the drop in the crosssection. By Hou et. al. [34] equation (3.4.1) is equivalent to

$$L_t = - \int_0^\pi \theta'_\alpha U d\alpha', \quad \theta_t = \frac{\pi}{L}(U_\alpha + \theta_\alpha \tilde{T}), \quad (y_0)_t = v(0, t), \quad (3.4.3)$$

where $U = \mathbf{u} \cdot \mathbf{n}$, $\mathbf{n} = \langle -y_\alpha, x_\alpha \rangle / s_\alpha$ is the outward unit normal, and $\tilde{T}(\alpha, t) = \alpha L_t / \pi + \int_0^\alpha \theta'_\alpha U d\alpha'$. \tilde{T} is related to T as $\tilde{T} = \mathbf{u} \cdot \mathbf{s} + T$. A unit sphere is chosen as the initial condition which is described by

$$\theta(0) = \alpha, \quad L(0) = \pi \quad (3.4.4)$$

Thereafter, the variables L , θ satisfy a system of ordinary differential equations (3.4.3) which is solved using a fourth-order Runge-Kutta method. All of the derivatives are spectrally calculated and all the integrals are approximated to sixth-order using the modified trapezoidal rule. The velocity \mathbf{u} is computed either to point-wise fifth-order or to uniform fifth-order as explained in section 3.2.

3.4.2 Mesh Refinement

Choosing the marker points in a controlled manner is also desirable. If the drop is smooth and rounded with low curvature, the computational points were forced to remain equally spaced in time, as explained in the previous section. In the case where the curvature is high at the tips, we would like to concentrate the marker points at those locations. Also, in the case when pinch-off occurs, points are needed to cluster at the pinch-points. Following the work of Nitsche and Steen [35], similarly to the equal arc-length formulation θ and s_α are related to x and y by

$$x_\alpha = s_\alpha \cos\theta, \quad y_\alpha = s_\alpha \sin\theta,$$

where $x(0, t) = 0$ and $y(0, t) = y_0(t)$. In this case, the governing equations are

$$s_{\alpha,t} = \tilde{T}_\alpha - \theta_\alpha U, \quad \theta_t = \frac{1}{s_\alpha}(U_\alpha + \theta_\alpha \tilde{T}), \quad (y_0)_t = v(0, t) \quad (3.4.5)$$

It is suggested by Nitsche and Steen [35] that, to obtain local mesh refinement, \tilde{T} has to be specified so that the relative spacing between the particles is $s_\alpha = R(\alpha)L(t)$, with L being the length of the curve and R attaining its minimum at a desired value of α . This approach implies that: (1) the particles cluster at a fixed position α_c at all times and (2) the amount of refinement is fixed in time.

It is desired to cluster the points in the region of high curvature which are the tips or pinch-off points in this work. It is also desired for the marker points to be initially uniformly distributed and the amount of local refinement to increase as the curvature increases. To accomplish this, the spacing s_α is set as follows

$$s_\alpha = f(\alpha, t), \quad (3.4.6)$$

where $f > 0$ is specified dynamically to be smallest at the tips while solving the steady states. To solve the pinch-off, f is chosen to be smallest at the points where pinch-off develops. The function f needs to satisfy the following constraint

$$\int_0^\pi f \, d\alpha = \int_0^\pi s_\alpha \, d\alpha = L(t) \quad (3.4.7)$$

Once f is specified, $\tilde{T}(\alpha, t)$ is determined from $s_{\alpha,t} = f_t(\alpha, t) = \tilde{T}_\alpha - \theta_\alpha U$ to be

$$\tilde{T}(\alpha, t) = \tilde{T}(0) + \int_0^\alpha f_t + \theta_\alpha U d\alpha', \quad (3.4.8)$$

where we choose $\tilde{T}(0) = 0$. Due to the symmetry of the initial conditions given in equation (3.4.4), s_α , θ_α and therefore, U are periodic with period π . To ensure that s_α , θ_α , and U remain periodic, \tilde{T} needs to be periodic as well. This can be achieved by enforcing f to be periodic as well such that

$$\int_0^\pi f_t d\alpha = \int_0^\pi \theta_\alpha U d\alpha \quad (3.4.9)$$

In this work, the function $R(\alpha) = (1 - \varepsilon \cos(2\alpha))/\pi$ is chosen to accumulate the points at the tips (See figure 3.4(a)). $R(\alpha)$ is positive with $\int_0^\pi R(\alpha) = 1$. $R(\alpha) = 1/\pi$ for $\varepsilon = 0$ which is the case of uniform mesh. $R(\alpha)$ has two minimums, occurring at $\alpha = 0$ and $\alpha = \pi$ for $0 < \varepsilon < 1$. Here, ε is chosen such that it increases linearly from 0 to its maximum value ε_{max} . Solving for the pinch-off, the computational points are accumulated at the locations of pinch-off. The function $R(\alpha)$ is chosen to have its minimum at α_c and $\pi - \alpha_c$, which are associated with the points for which the pinch-off occurs. In these simulations, $R(\alpha) = \frac{g(p)}{\int_0^\pi g(p) d\alpha}$ where $g(x) = 1.125 + \varepsilon(\cos(4x) - \cos(2x))$ and $p(x) = \tan^{-1}(-1.155 \tan x)$ in which the value -1.155 is chosen based on the pinching position using trial and error. After the pinch-off, three separate drops form. For the middle drop which is symmetric, points are bunched at $\alpha = 0$ and $\alpha = \pi$. Therefore $R(\alpha) = (1 - \varepsilon \cos(2\alpha))/\pi$ is used where the ε is chosen such that it decreases linearly from ε_{max} to 0 (see figure 3.4(b)). The bottom end piece of the main drop has its points concentrated at $\alpha = \pi$ for $R(\alpha) = (1 + \varepsilon \cos(\alpha))/\pi$ (see figure 3.4(c)). The top end piece is symmetric to the bottom end piece. Given $R(\alpha)$ and the length of the drop, the function $f(\alpha, t) = R(\alpha)L(t)$ can be computed.

To compute the rate of change of arc-length in time

$$\dot{s} = \dot{f} = R_t L + L_t R$$

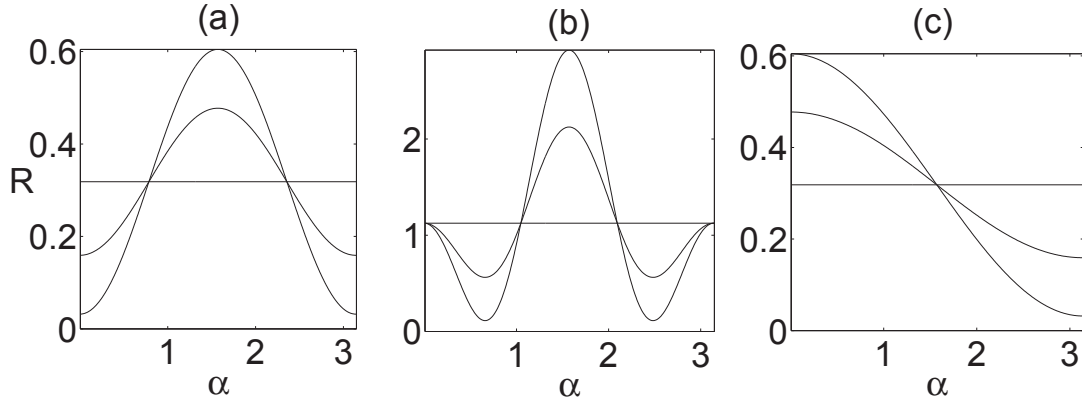


Figure 3.4: (a) $R(\alpha)$ constructed to bunch the points at the tips, $\varepsilon=0, 0.5,$ and 0.9 (b) $g(\alpha)$ constructed to bunch the points near the pinch-off $\varepsilon=0, 0.5,$ and 0.9 (c) $R(\alpha)$ constructed to bunch the points at only one tip $\varepsilon=0, 0.5,$ and 0.9 .

where $L_t = -\int_0^\pi \theta_\alpha U d\alpha$ and $U = \mathbf{u} \cdot \mathbf{n}$. The derivative R_t is calculated using a first-order finite difference method. Note that using the first-order finite difference approach only affects the position of computational points, and it does not influence the overall accuracy of the method.

Next, we discretize the interface by $n + 1$ points which are uniformly spaced in the Lagrangian variable α , so that $\alpha_j = j\pi/n$, $j = 0, \dots, n$, and solve the system of ordinary differential equations (3.4.5) using a fourth-order Runge-Kutta method with initial conditions $s_{\alpha,j}(0) = 1, \theta_j(\alpha_j, 0) = \alpha_j$. Before the pinch-off, all the spatial derivatives are spectrally calculated. Since the parameters $x(\alpha_j, t), y(\alpha_j, t), \theta(\alpha_j, t), s(\alpha_j, t)$ and the curvature are periodic, the derivatives can be spectrally calculated. After the pinch-off, since the second derivatives are not continuous due to applying the spline interpolation, the second-order central finite difference method is used to compute the derivatives. The periodicity at $\alpha = 0$ and $\alpha = \pi$ is used to obtain this

Chapter 3. Numerical Approach

approximation. Compared to the fourth-order finite difference approach, the second-order method helps smooth out the jump caused by recoiling. All the integrals are approximated to sixth-order using the modified trapezoidal rule. The velocity \mathbf{u} is computed either to point-wise fifth-order or to uniform fifth-order.

Chapter 4

Steady States For $Ca < Ca_{cr}$ and Non-Steady Evolution for $Ca > Ca_{cr}$

In this chapter, the numerical results obtained from the simulations of an axisymmetric drop in Stokes flow immersed in an axisymmetric strain flow are presented.

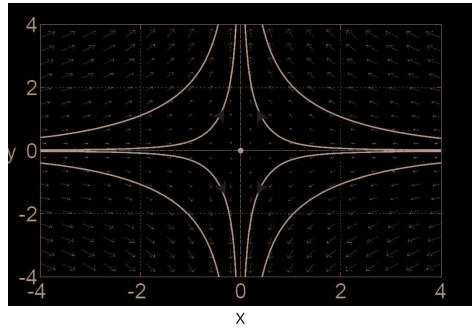
4.1 Background Flow

We consider the extensional flow introduced by Sherwood [13] described by,

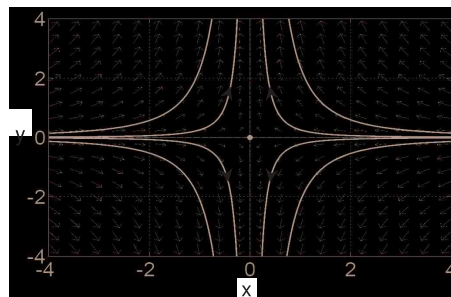
$$u^\infty = -\frac{1}{2}\left(Gx + \frac{3Gc_2y^2x}{R^2}\right), \quad v^\infty = Gy + \frac{Gc_2y^3}{R^2}, \quad (4.1.1)$$

where $R = 1$ is the initial drop radius, G is the measure of strain field and c_2 is the coefficient of the higher order nonlinear term. The imposed axisymmetric flow is a combination of a linear flow and a cubic flow. There is no quadratic term due to symmetry and the coefficients are chosen so that it satisfies the continuity

(a) $c_2 > 0$



(b) $c_2 = 0$



(c) $c_2 < 0$

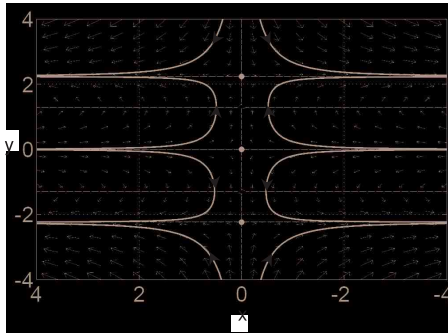


Figure 4.1: Background flow. (a) $c_2 = 0.5$ (b) $c_2 = 0$ (c) $c_2 = -0.2$.

equation. Previous studies mostly considered linear far field only, $c_2 = 0$ which is a good approximation for sufficiently small drops. Part of our goal is to study the effect of the nonlinear term given by $c_2 \neq 0$ introduced by Sherwood [13]. Figure 4.1 represents three different background flows for the values of $c_2 = -0.2, 0$, and 0.5 .

The flow with positive c_2 is qualitatively similar to the flow with $c_2 = 0$. All three flows have saddle points at the origin. For $c_2 \geq 0$, there is a single stagnation point. For $c_2 < 0$, there are three at $(0, 0)$, $(0, -1/\sqrt{-c_2})$ and $(0, 1/\sqrt{-c_2})$. The nonlinear term becomes more important for the drops reaching these stagnation points. The effect of the nonlinear term is presented in this chapter. Section 4.2 presents the drop evolution for various values of c_2 , as well as the method used to identify the steady states. Section 4.3 presents a complete classification of the steady states in the parameter space. In section 4.4, we investigate the behavior of drops for capillary numbers past their critical value and discuss the improvement achieved by using uniform fifth-order method.

4.2 Time Evolution of a Drop Towards Steady States

This section investigates the time evolution of a drop towards the steady states for fixed values of $Ca < Ca_{cr}$ and c_2 . Note that the critical value is the value of capillary number above which no steady states exist. The initial condition is a unit sphere centered at the origin. An appropriate value for Δt based on the maximum curvature and the number of computational points is chosen to compute the drop evolution. The dependence of the steady states on the parameters is studied.

Figure 4.2 displays the computed results for (a) $c_2 = 0.5$, $Ca = 0.15$; (b) $c_2 = 0$, $Ca = 0.25$; (c) $c_2 = -0.2$, $Ca = 0.2$ and (d) $c_2 = -0.5$, $Ca = 0.3$ at times (a) $t \in [0, 9.5]$, (b) $t \in [0, 70]$, (c) $t \in [0, 31]$ and (d) $t \in [0, 66]$. These results were obtained using (a) $n = 1024$, $\Delta t = 0.005$ (b) $n = 512$, $\Delta t = 0.005$ (c) $n = 256$, $\Delta t = 0.01$ and (d) $n = 64$, $\Delta t = 0.02$. The figure shows that as time increases, the drop starts deforming from the initial spherical shape and keeps deforming until it

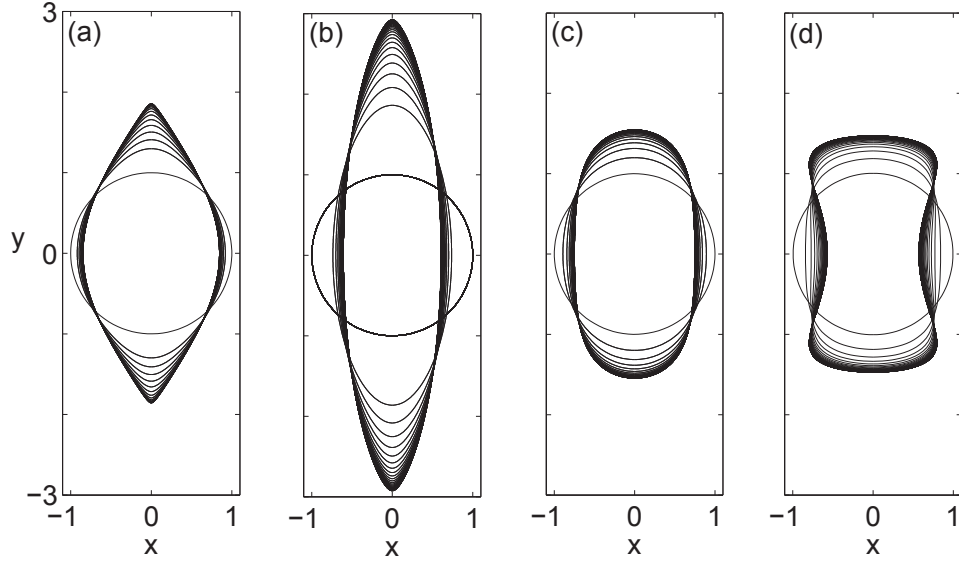


Figure 4.2: Computed time evolution of axisymmetric drops. (a) $c_2 = 0.5$, $\lambda = 0.01$, $Ca = 0.15$ (b) $c_2 = 0$, $\lambda = 0.01$, $Ca = 0.25$ (c) $c_2 = -0.2$, $\lambda = 0.01$, $Ca = 0.2$ (d) $c_2 = -0.5$, $\lambda = 0.01$, $Ca = 0.3$.

approaches a steady state. In figure (a), with $c_2 > 0$, the drop tips tend to become increasingly pointed. In figure (b), with $c_2 = 0$, the drop elongates before reaching a steady state. In figure (c), with $c_2 = -0.2$, the drop maintains a rounded shape throughout the evolution and reaches an approximately elliptical steady shape. In figure (d), with a more negative value of $c_2 = -0.5$, the drop evolves towards a biconcave shape. In this dissertation, we choose values of $c_2 \in [-0.5, 0.5]$. This enables us to separately investigate all the possible drop shapes and also provides a full characterization of the drop evolution in time. For small capillary numbers, the drop does not change much from its initial state. For the cases shown in figure 4.2, the capillary numbers are chosen close to their critical values to investigate the

evolution of the drop in more deformed shapes. Larger n and smaller Δt is needed for larger maximal curvature.

4.2.1 Identifying the Steady States

This section presents an approach to identify the steady state solutions. As an example, we consider the drop for the case of $c_2 = 0$, $\lambda = 0.01$ and $Ca = 0.25$ shown in figure 4.2(b). The parameters that we track to determine the steady states are the maximum curvature κ_{max} , the maximum y -coordinate y_{max} (also refer to as L), and the drop deformation, defined to be $D = (L - B)/(L + B)$ where B is the half-width of the drop at $y = 0$. Figure 4.3 shows the evolution of these parameters in time. All three appear to approach a constant as time increases. These constants describe the steady state values.

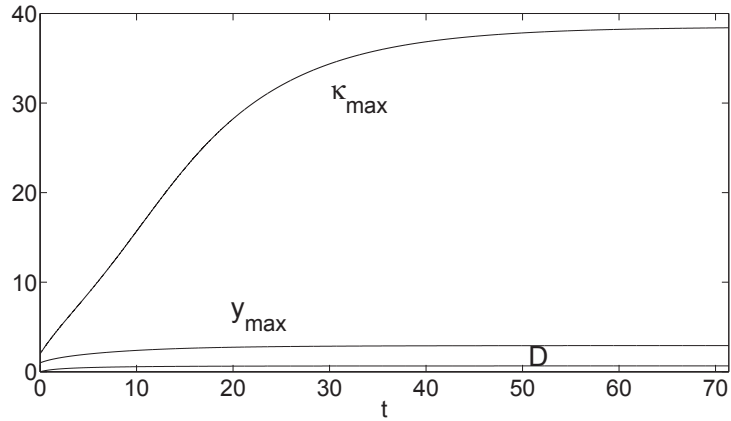


Figure 4.3: Maximum curvature κ_{max} , maximum y -coordinate y_{max} , and deformation D , vs. time.

To better approximate the limiting steady state values κ_{max} , y_{max} and D , we investigate the rate at which the difference between consecutive values decreases. Let $Q(t)$ represent one of the values of interest, κ_{max} , or y_{max} , or $D(t)$. We set

$Q_k = Q(t_k)$ and investigate $\Delta Q_k = Q_{k+1} - Q_k$. We find that these differences decrease by a factor that approaches a constant. To illustrate, figure 4.4 plots the ratios $r(k) = \Delta Q_{k+1}/\Delta Q_k$ for each of the three quantities. It shows that for all three quantities the values approach a constant. Thus, the series,

$$Q_\infty = Q_j + \sum_{k=j}^{\infty} \Delta Q_k \quad (4.2.1)$$

converges geometrically for sufficiently large j , as long as $r < 1$. Based on extensive

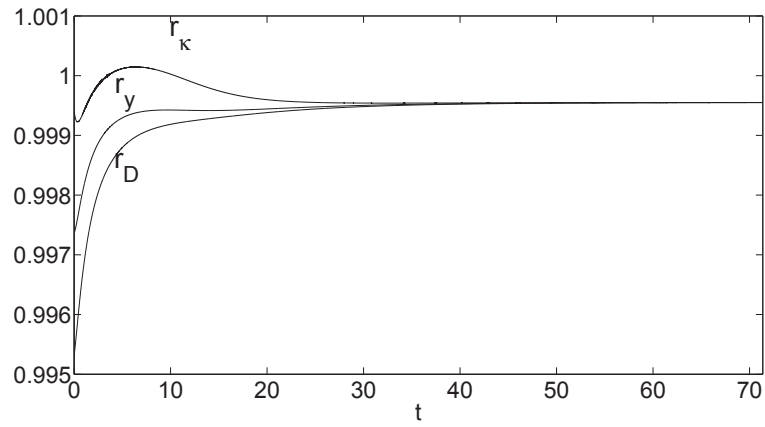


Figure 4.4: Ratios $r(k) = \Delta Q_{k+1}/\Delta Q_k$, where $\Delta Q_k = Q_{k+1} - Q_k$, and Q is the maximum curvature (r_κ), the maximum y-coordinate (r_y), and deformation (r_D), vs. time.

simulations, we found that convergence of these ratios to a value $r < 1$ is an earlier reliable indicator of the existence of a steady state, than the actual values of y_{max} , D , and k_{max} . Furthermore, obtained ratios can be used to verify the resolution needed for these simulations and also can be considered as an indicator of the non-steady region. If $r > 1$, either the resolution is low or $Ca > Ca_{cr}$ [1]. To determine the steady state values we approximate,

$$Q_\infty \approx Q_j + \Delta Q_j \sum_{k=0}^{\infty} r^k = Q_j + \frac{\Delta Q_j}{1-r}. \quad (4.2.2)$$

Note that,

$$Q_j + \frac{\Delta Q_j}{\Delta t} \frac{\Delta t}{1-r} \approx Q_j + \frac{dQ}{dt}(t_j) \frac{\Delta t}{1-r}. \quad (4.2.3)$$

This shows that r depends on Δt so that $\Delta t/(1-r) \approx \text{constant}$.

To compute the steady states using the equation (4.2.2), we choose j such that $\Delta D/\Delta t$ is less than 10^{-5} .

4.3 Classification of Steady States Solutions

In this section, a complete classification of the steady state solutions is presented as a function of the three key parameters: Ca , λ , and c_2 .

4.3.1 Steady States as Function of $Ca < Ca_{cr}$

This section shows dependence of steady states on ca , for fixed values of $\lambda = 0.05$ and $c_2 = 0$. The behavior for other λ , and c_2 is qualitatively similar.

The Case of $\lambda > 0$

We compute steady states for an increasing sequence of values of $Ca = Ca_k$, and use these results to determine Ca_{cr} . To approximate Ca_{cr} slowly from below, we increase Ca by an amount ΔCa such that the change in D , ΔD , is a small specified value initially set to 0.01. Linear extrapolation is used to estimate Ca_{k+1} . That is, give Ca_k and Ca_{k-1} , we obtain Ca_{k+1} as follows,

$$Ca_{k+1} = Ca_k + \frac{Ca_k - Ca_{k-1}}{D_k - D_{k-1}}(\Delta D).$$

Capillary number values $Ca_0 = 0.005$ and $Ca_1 = 0.01$ are chosen initially. As the slope $\Delta Ca/\Delta D$ increases, the deformation-step ΔD should be maintained small to prevent overshooting to the region of $Ca > Ca_{cr}$. When the slope is greater than 100, the process is terminated and the last capillary number is our approximation for Ca_{cr} . Figure 4.5(a) plots the steady states solutions for an increasing set of values Ca approaching Ca_{cr} . As the capillary number increases, these curves depart from the sphere and become more elongated and deformed. Figure 4.5(b,c) plot

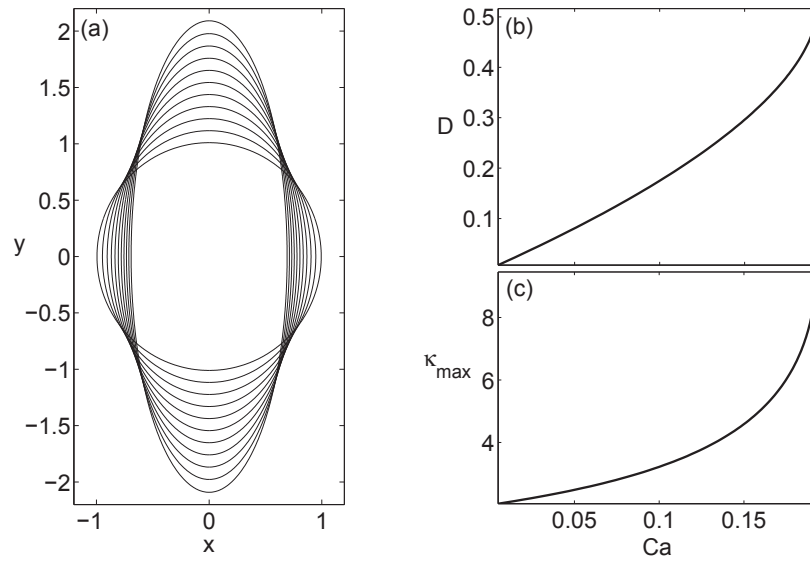


Figure 4.5: (a) Initial solution and steady states for $Ca = 0.005, 0.01, 0.0511, 0.0876, 0.1164, 0.1387, 0.1560, 0.1690, 0.1787, 0.1855, 0.1900, 0.1924$, $\lambda = 0.05$, $n = 512$, $\Delta t = 0.01$, and $c_2 = 0$ (b) Deformation as a function of capillary number (c) Maximum curvature as a function of capillary number.

the deformation D and the maximum curvature, respectively, as a function of the capillary number. As the capillary number increases and approaches its critical value, maximum curvature and deformation of the drop increase. To evaluate the curvature more accurately, in some cases the stopping criterion is chosen to be a slope of 1000. The stopping criterion has a noticeable effect on the drop's curvature, but at the same time it does not impact the critical capillary number much. Later in section

4.3.2, the effect of the stopping criterion will be evident. The simulations such as shown in figure 4.5, used to determine Ca_{cr} for a fix set of λ , usually take weeks to compute. For smaller values of λ , the maximal curvature near Ca_{cr} are large requiring smaller Δt , and larger n . For larger values of λ , the maximum curvature is moderate but the flow is approaching the steady states very slowly which slows down the simulations. To reduce the simulation time, the steady state solution for each capillary number is used as the initial condition for the next step.

The Case of $\lambda = 0$

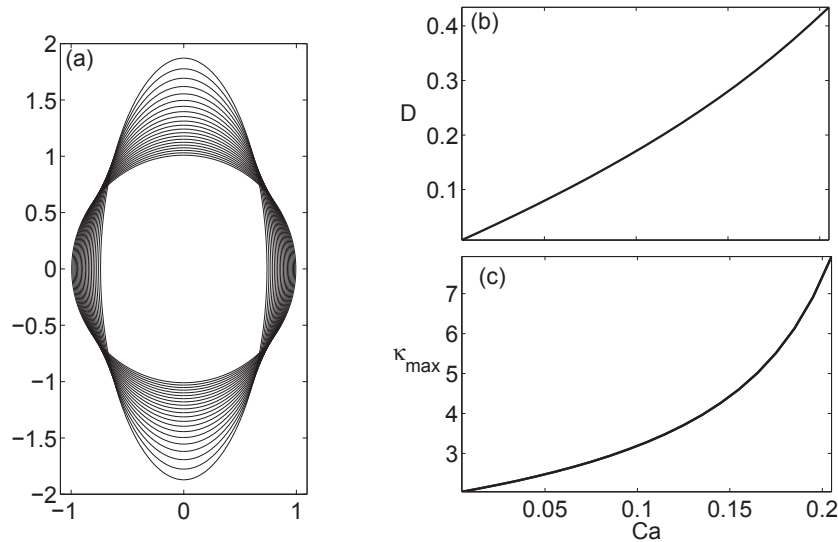


Figure 4.6: (a) Steady States for $Ca = 0.005 : 0.01 : 0.205$, $\lambda = 0$, $c_2 = 0$, $n = 512$ and $\Delta t = 0.01$. (b) Deformation as a function of capillary number (c) Maximum curvature as a function of capillary number.

For $\lambda = 0$, slender-body theory predicts a stationary drop for all values of Ca [5].

In this section we present multiple steady state solutions and discuss our observations for $\lambda = 0$, $c_2 = 0$. Figure 4.6(a) displays the steady state solutions for $Ca = 0.005 : 0.01 : 0.205$. Part (b) plots the deformation of these steady states as a function of the capillary number. This figure is in strong agreement with Eggers and du Pont [12], where an excellent agreement with perturbation theory is reported. The deformation graph is increasing and almost approaching a line which can be interpreted as non-existence of Ca_{cr} . Figure 4.6(c) plots the maximum curvature as a function of the capillary number. Figure 4.7 demonstrates the steady state shape for $Ca = 0.3$, to compute this solution, $n = 256$ points are used clustered at the tips, using the method described in section 3.4.2 with function $R(\alpha) = (1 - \varepsilon \cos(2\alpha))/\pi$. The shape is elongated with a maximum curvature of 100.

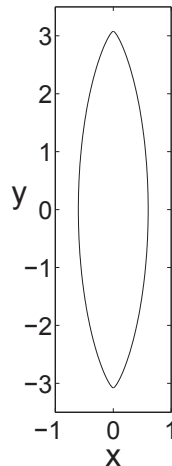


Figure 4.7: Steady States for $Ca = 0.3$, $\lambda = 0$, $c_2 = 0$.

4.3.2 Steady States as Function of λ , $Ca = Ca_{cr}$

In this section, we compute the steady states at the critical capillary number, $Ca = Ca_{cr}$, for a range of values of λ . These solutions are computed using the approach

described in section 4.3.1. Throughout this section, $c_2 = 0$. Other values of c_2 exhibit qualitatively similar behaviors. Figure 4.8(a) plots the solution with $\lambda = 0.02, 0.05, 1$ and 10 . For smaller values of λ the steady state drop is more elongated, with the largest elongation shown corresponding to $\lambda = 0.01$. The behavior is also captured in figure (b), which shows that as λ decreases, the deformation D increases. Figure (c) shows that the corresponding maximal curvature κ_{max} also increases as λ decreases. As λ increases, the maximum curvatures seem to approach a constant value significantly larger than the curvature $\kappa_{max} = 2$ of the initial sphere. The

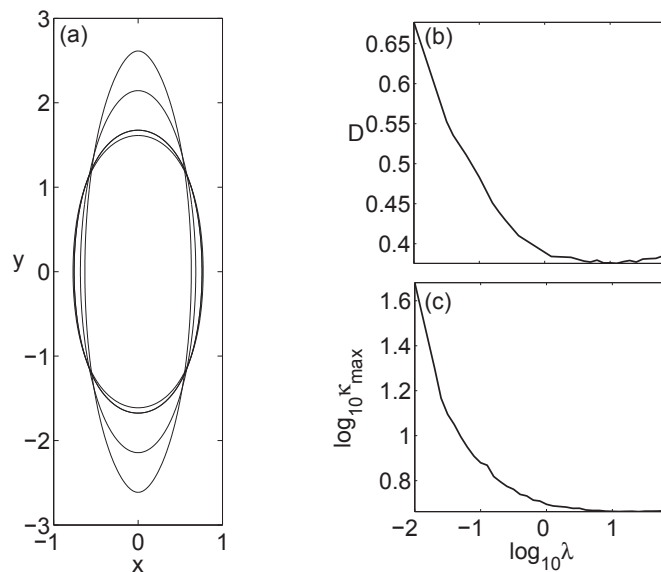


Figure 4.8: (a) Steady states for $Ca = Ca_{cr}$ and $\lambda = 10, 1, 0.05, 0.02, 0.01$ (b) Deformation as a function of $\log_{10}(\lambda)$ (c) Maximum curvature as a function of $\log_{10}(\lambda)$.

numerical noise observed in figure 4.8 is due to the approximation made for the stopping criteria given in section 4.3.1. Small changes to the capillary number result in a change in the maximum curvature. Here, we compute the results for small λ using the method described in section 3.4.2 to cluster particles at the tip. This enables us to resolve the regions of high curvature. In these computations, the final clustering factor is 13. That is, the finest spacing between points at the final time

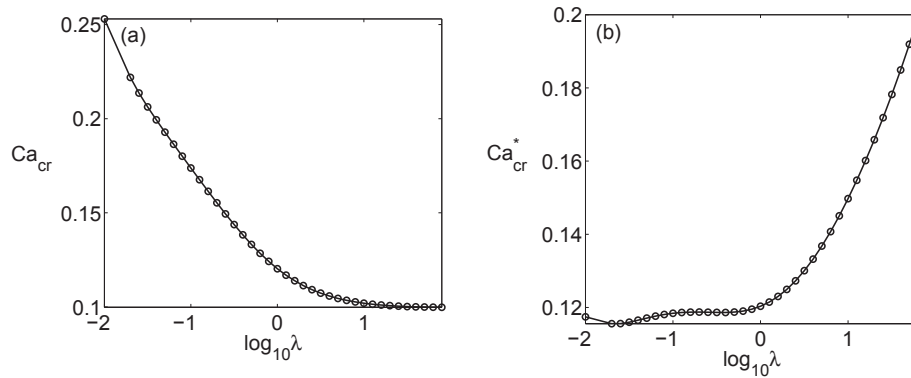


Figure 4.9: (a) Ca_{cr} as a function of $\log_{10}(\lambda)$, $c_2 = 0$ (b) Ca_{cr}^* as a function of $\log_{10}(\lambda)$, $c_2 = 0$.

using 256 points which is the same as if we had used 13×256 equally spaced points.

To compare these results with Taylor's universal theory, the length and capillary number are re-scaled to $l^* = l\lambda^{1/3}$ and $Ca^* = Ca\lambda^{1/6}$. Fig 4.9(a) plots the capillary

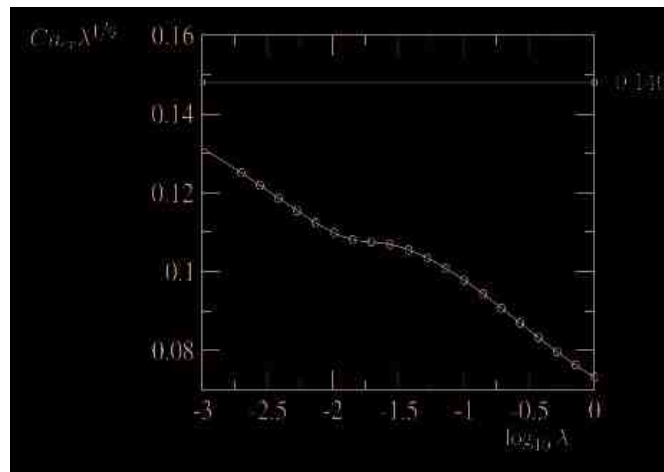


Figure 4.10: Ca_{cr}^* as a function of $\log_{10}(\lambda)$ presented by Eggers, $c_2 = 0$.

number Ca as a function of λ , and figure (b) plots the re-scaled capillary number Ca^* versus λ . A figure of the re-scaled capillary number was previously shown by Eggers and du Pont [12], and is reproduced here in figure 4.10. Comparing figures 4.9(b)

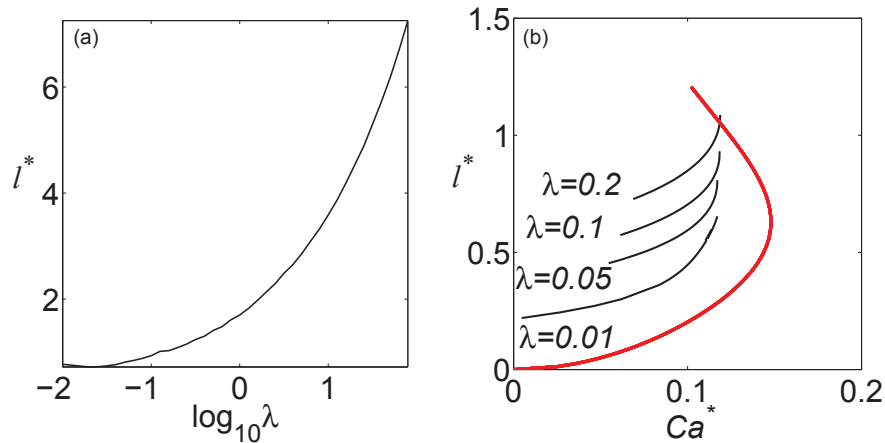


Figure 4.11: (a) Rescaled length $l^* = l\lambda^{1/3}$ as a function of $\log_{10}(\lambda)$, $c_2 = 0$, $Ca = Ca_{cr}$ (b) Rescaled length $l^* = l\lambda^{1/3}$ as a function of $Ca^* = Ca\lambda^{1/6}$, $c_2 = 0$, $Ca = Ca_{cr}$.

and 4.10 we see a discrepancy between our and Eggers results. For example, for $\log(\lambda) = -2$ our value is approximately 0.118, whereas Eggers is 0.11. Furthermore, the qualitative behaviors for $\log(\lambda) > -2$ differ markedly: Eggers' decreases, ours increase, yielding very different results for larger λ . For example, for $\log(\lambda) = 0$ ($\lambda = 1$), our value is approximately 0.12 and Eggers' value is much smaller, 0.075. We have confidence in our results since (1) we have carefully checked our work, (2) our results are consistent with Eggers figure 7 which is inconsistent with his figure 8 shown in 4.10. Thus there are some inconsistencies in his paper.

Figure 4.11 plots the re-scaled length l^* as a function of λ (figure a) and Ca (figure b). The result of Taylor's universal theory, obtained in the limit of infinite

slenderness ($B/L \rightarrow \infty$)

$$Ca^* = \frac{1}{\sqrt{20}} \frac{\sqrt{l^*}}{1 + 4l^{*3}/5} \quad (4.3.1)$$

is the red (parabolic) curve in (b). While it appears that the computed maximum Ca^* does not converge to Taylor's value as λ decreases, figure 4.11(b) shows that there is an increasing trend in Ca_{max}^* as λ decreases below 0.01 that we have not yet resolved.

4.3.3 Steady States as Function of c_2 , $Ca = Ca_{cr}$

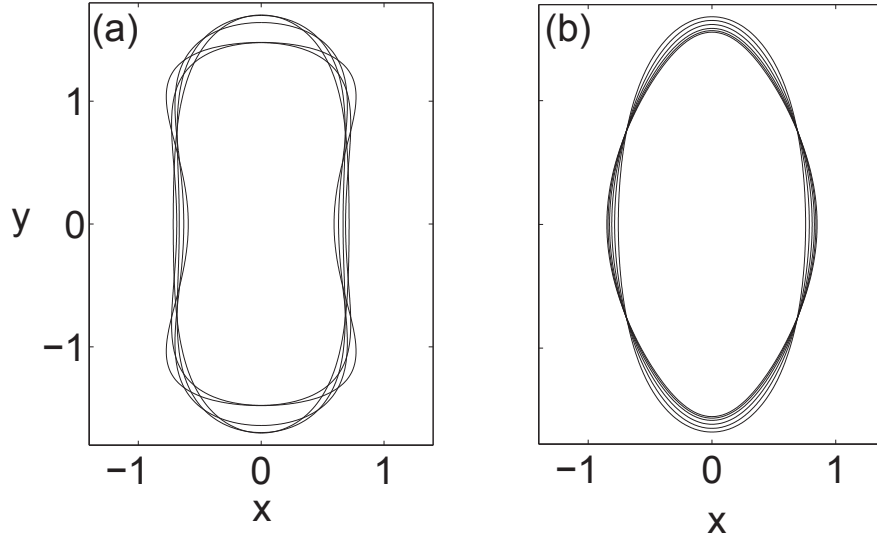


Figure 4.12: (a) Steady States for $c_2 = -0.1, -0.2, -0.3, -0.4$ and -0.5 , $\lambda = 1$ and $Ca = Ca_{cr}$ (b) Steady States for $c_2 = 0, 0.1, 0.2, 0.3, 0.4$ and 0.5 , $\lambda = 1$ and $Ca = Ca_{cr}$.

Figure 4.12 plots the steady state solutions at $Ca = Ca_{cr}$ for various values of $c_2 \in [-0.5, 0.5]$. Through this section, we use $\lambda = 1$ for simplicity. In figure(a), for small values of c_2 , the steady shapes are elliptical. For more negative values, the shapes are

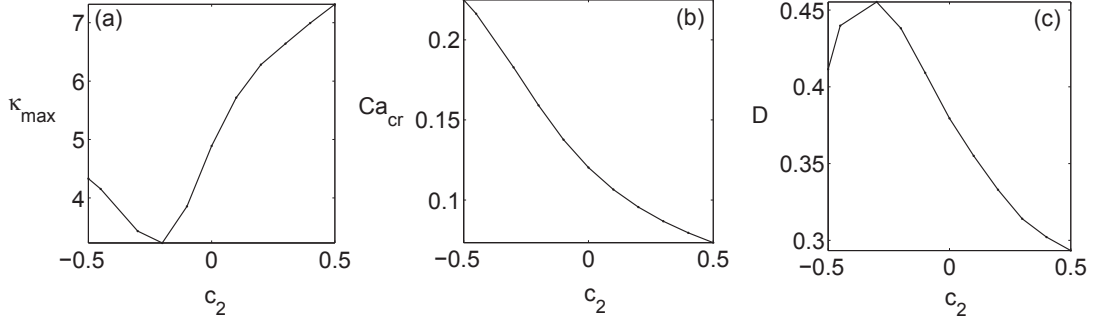


Figure 4.13: (a) Maximum curvature as a function of c_2 , $\lambda = 1$ (b) Critical capillary number as a function of c_2 , $\lambda = 1$ (c) Deformation as a function of c_2 , $\lambda = 1$.

biconcave. This can be explained by remembering that for $c_2 < 0$, the background flow has two non-zero stagnation points at $(0, -1/\sqrt{-c_2})$ and $(0, 1/\sqrt{-c_2})$. For sufficiently negative values of c_2 , these stagnation points are close to the drop and the effect of the corresponding strain fields becomes visible as biconcavity. The steady shapes for $c_2 > 0$ shown in figure 4.12(b) remain concave, but develop large curvatures near the tips. The dependence of κ_{max} , Ca_{cr} and D as a function of c_2 is shown in figure 4.13. The critical capillary number increases as c_2 decreases, while the maximum curvature of the drop and its deformation does not vary monotonically. As c_2 decreases from any positive value to zero and negative values with smaller magnitude, the maximum curvature decreases while the deformation of the drop increases. In the region where the shape of the drop is biconcave, maximum curvature increases and the drop deformation decreases. This seems different than all other cases. In the other cases κ_{max} increases as D increases, so the drop develops high curvature as it gets long and longer but in this case, the drop develops high curvature regions while it stays confined in a region. κ_{max} has a local minimum around $c_2 =$

-0.2 , and D has a local maximum around $c_2 = -0.3$. We note that the values $c_2 < -0.2$ are precisely those for which the shape starts to become biconcave.

4.4 Non-steady Evolution

The previous section presented the steady states for $Ca < Ca_{cr}$. The focus of this section is to study the evolution of viscous drops in time for capillary numbers past the critical value. In figure 4.14, the top row represents the evolution of the drop for a finite value of capillary number past the critical value and the bottom row represents the evolution of the drop in the absence of surface tension, which we will denote by $Ca = \infty$. For all results in 4.14, $\lambda = 0.01$.

Fig 4.14 (a) shows the evolution for $c_2 = 0.5$, $Ca = 0.2$, at times $t \leq 2.07$, computed with $n = 512$, $\Delta t = 0.0025$. The drop tips become increasingly pointed. At the final time $\kappa_{max} = 59$. In section 4.4.1, we investigate whether the drop develops a corner or a cusp. Figure (b), plots the evolution of the drop for same value of c_2 , but $Ca = \infty$. The drop elongates and it forms a spindle-like shape.

In figures (c,d), $c_2 = 0$, while $Ca = 0.3$, $t \leq 11$ for (c) and $ca = \infty$ for (d). The drops keep elongating with a moderate curvature at the tips. For $Ca = \infty$ the drop keeps elongating into a rod shape and interfaces are nearly elliptical throughout the evolution. These plots are in a strong agreement with Pozrikidis' figure 7 [11].

In figures (e,f) the value of $c_2 = -0.2$, while $Ca = 0.3$ for (e) and $Ca = \infty$ for (f). In (e), the drop maintains a rounded shape which later transforms into a dumbbell shape. As we will show later, as long as Ca is not too large, the drop surface pinches at two points. The capillary number before which the pinch-off occurs is called "singular capillary number" and is denoted by Ca_s . In (f), the drop also develops dumbbell shape, but the outer portions grow. We will see that the radius

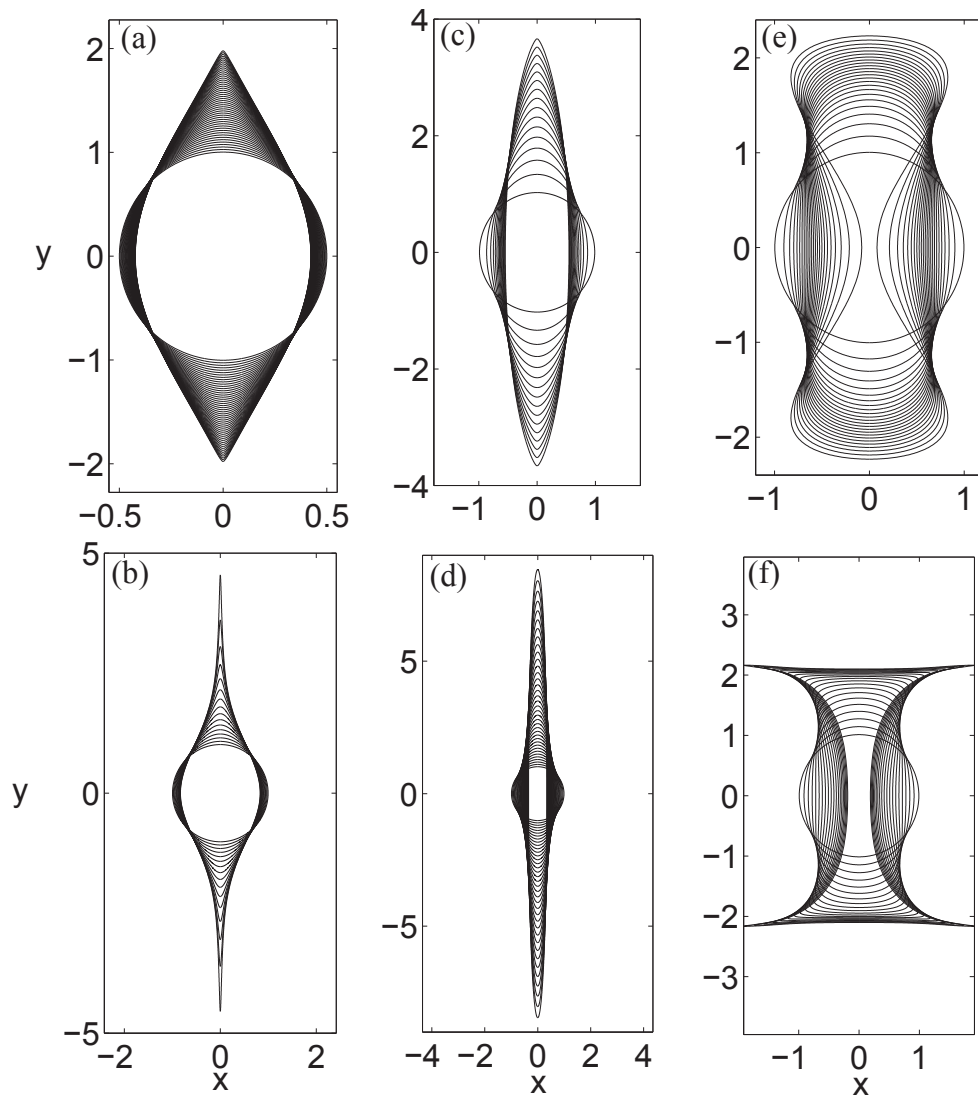


Figure 4.14: Evolution of drops passed the critical capillary numbers, $\lambda = 0.01$. (a) $c_2 = 0.5$, $Ca = 0.2$ (b) $c_2 = 0.5$, $Ca = \infty$ (c) $c_2 = 0$, $Ca = 0.3$ (d) $c_2 = 0$, $Ca = \infty$ (e) $c_2 = -0.2$, $Ca = 0.3$ (f) $c_2 = -0.2$, $Ca = \infty$.

of the top and bottom grows exponentially fast.

4.4.1 Cusp or Corner?

Figure 4.14(b) illustrates a spindle-like shape for $c_2 > 0$ and $Ca = \infty$. In this section we investigate whether for $Ca < \infty$, the drop approaches a cusp or a corner. To this effect we consider the angle θ formed between tangent line and x -axis illustrated in figure 4.15(a). Figure 4.15 shows the solution at $t = 0.4, 0.5$ and 0.6396 for $Ca = 0.5$ using $n=256$ points which are bunched to the tips with $\varepsilon_{max} = 0.999$. By clustering

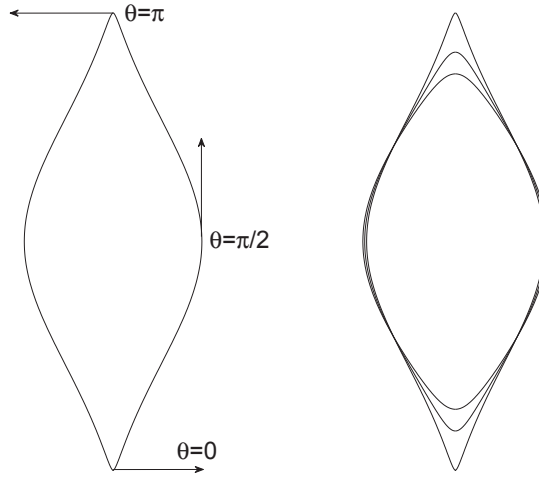


Figure 4.15: (a) Tangent angle θ (b) Drop profiles for $Ca = 0.5$, $c_2 = 0.5$, $n = 256$, $\Delta t = 0.0001$, $\varepsilon_{max} = 0.999$, $\lambda = 0.01$, $t = 0.4, 0.5$ and 0.6396 .

the points to the tips, a factor of 60 is obtained which is equivalent to using 15760 equally-spaced computational points. $t = 0.6396$ is the last time computed. Note that the numerical calculations are stopped at $t = 0.6396$ since the curvature was large and it acquires small time-steps. Figure 4.16(b) plots the angle as a function of arc length for $t = 0 : 500 : 6396$. All the units are expressed in degrees. As the time increases, the angle θ increases very rapidly from zero which indicates the cusp formation. Generally, the cusp formation refers to the case at which the angle reaches quickly from zero to 90° . Figure 4.17 plots the length of the drop as a function of

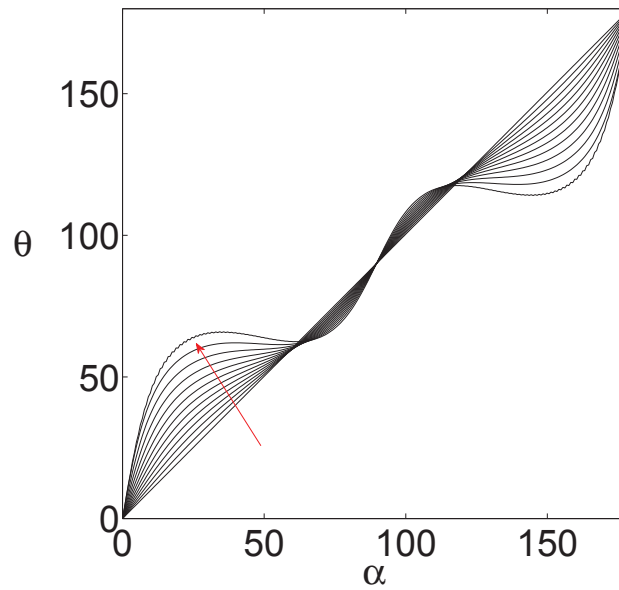


Figure 4.16: Angle θ as s function of arc length for $Ca = 0.5$, $c_2 = 0.5$ and $t = 0 : 500 : 6396$. Arrow displays the direction of increasing time.

time. This figure shows that the drop length continues to increase with time which again is evidence of the cusp formation.

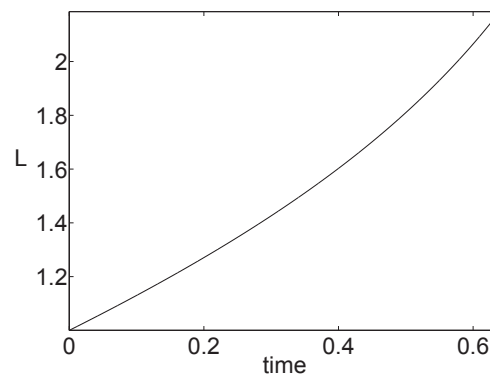


Figure 4.17: Length as a function of time for $Ca = 0.5$, $c_2 = 0.5$ and $t = 0 : 6396$.

4.4.2 Effect of Accuracy

As explained in section 3.2.1, Nitsche et al. [1] developed a uniformly fifth-order method by applying pole corrections. These corrections improve the accuracy of the simulations only when the endpoint curvatures and velocities are moderate. In this section two cases are studied in which the pole corrections are not negligible.

Case 1

Considering a spherical drop as the initial condition, for $c_2 = 0$, $\lambda = 10$ and $Ca = 0.4$, the drop keeps elongating. Even though the interface is smooth and curvature is growing slowly, the results are difficult to compute. Figure 4.18(a) illustrates the

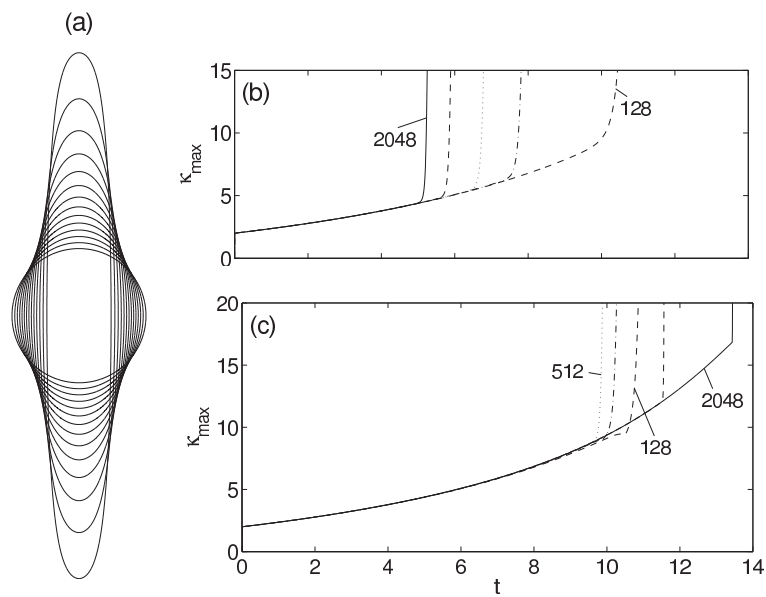


Figure 4.18: (a) Evolution of a drop with $c_2 = 0$, $\lambda = 10$, $Ca = 0.4$, $n = 2048$ and $\Delta t = 0.005$ (b) Maximum curvature as a function of time using point wise method (c) Curvature as a function of time using uniform method.

evolution of the drop using $n = 2048$ computational points with $\Delta t = 0.005$ for $t = 0 : 1 : 13$. The drop keeps elongating to a long rod shape. Figure 4.18(b,c), shows the curvature as a function of time for different values of computational points. These results demonstrate that the dependence of curvature to n is not monotonic. In part (b), the break-down time decreases as n increases from 128 to 1024. This results may be misinterpreted as a finite time singularity but as n increases from 1024 to 2048, the break-down time increases, which is an indication of convergence. Using a uniformly fifth-order method, as shown in part (c), the break-down time increases past $n = 512$ and solves the solutions for longer times. Therefore it is predicted that a solution exists for all times and it is possible to compute it with acceptable resolution.

Case 2

Similar results have been observed for the case where $c_2 > 0$. The shape of the drop differs from the one observed for $c_2 = 0$, forming into a spindle-like shape compared to the elongating rod shape. Figure 4.19 plots the evolution of the drop for up to $t = 0.403$. The drop becomes more pointed as time increases. The maximum curvature obtained with 2048 marker points is equal to 490 and it breaks up at $t = 0.403$. Figure 4.19 plots $1/\kappa_{max}$ as a function of time for $Ca = 0.5$, for various resolutions ranging from $n = 256$ to $n = 2048$, using the point-wise fifth-order method part (b), and the uniform fifth-order method part (c). This figure shows that the maximum curvature becomes unbounded in finite time. The solution breaks down after the final time is reached since the method used does not converge. By varying Δt between 0.2–0.001, it is confirmed that this behavior is independent of the time-step. For the point-wise fifth-order method, the breakdown time decreases as n increases from 128 to 2048. This may be misinterpreted as a finite time singularity in the curvature. The results obtained with the uniformly fifth-order methods are

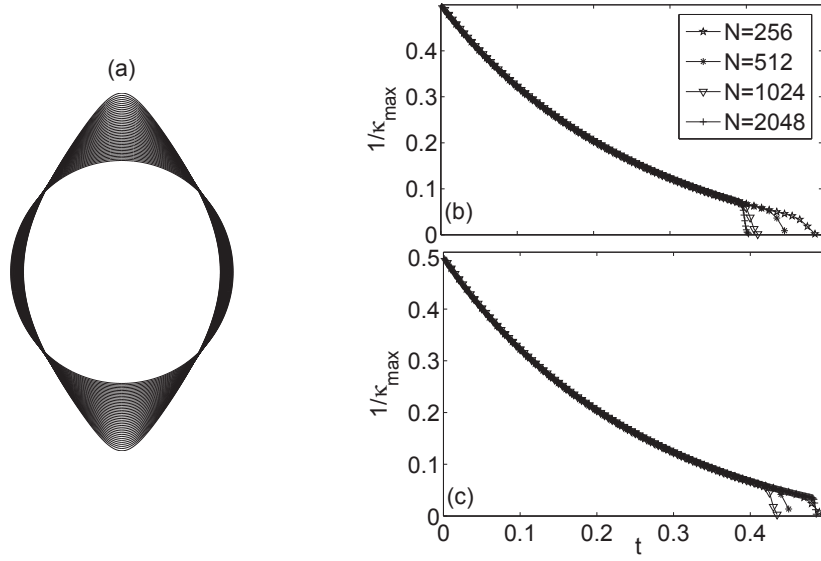


Figure 4.19: (a) Curvature as a function of time for $c_2 = 0.5$, $Ca = 0.5$, $n = 2048$, and $\Delta t = 0.001$ (b) $1/\text{curvature}$ as a function of time using point wise method (c) $1/\text{curvature}$ as a function of time using uniformly fifth-order method.

similar for n up to 1024. However, with $n = 2048$, the solution is solved for longer time. Thereby at this case the solution converges and a higher resolution is needed to compute the results for longer times.

4.4.3 Pinch-off or Exponential Growth?

When $c_2 < 0$ and $Ca > Ca_{cr}$, the drop forms into a dumbbell shape and it exhibits different dynamics depending on the capillary number. We found that for capillary numbers up to some critical value $Ca < Ca_s$, the drop pinches at two symmetric points in finite time. For capillary numbers past the value Ca_s , the drop keeps elongating from the corners with no visible singularities. This section explains the details.

For the case of $Ca < Ca_s$, the behavior of drop shown in figure 4.14(e), is in an excellent agreement with figure 6 and 7 reported by both Pozrikidis [11] and Sherwood [13]. Sherwood discovered that when the capillary number is raised beyond the value where $(R/L)^2 = -c_2$, the steady solutions computed from the slender-body theory break down. L is the drop half-length and R is the initial drop radius. For $c_2 = -0.2$, the predicted drop length at which the break-up occurs is at $L = 2.24$ which is in excellent agreement with the length obtained from the numerical simulations presented here. The length of the drop when its surfaces pinches is $L = 2.24$.

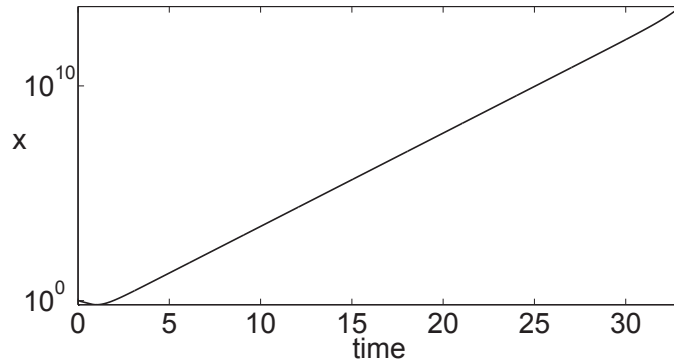


Figure 4.20: The maximum value of x component of the drop in time in semi-log scale for $Ca = \infty$, $\lambda = 0.5$, $c_2 = -0.2$ up to time $t = 33$.

To investigate the behavior of a drop for $Ca > Ca_s$, an infinite capillary number is considered. When the capillary number is infinite and the viscosity ratio $\lambda = 1$, equation (2.6.11) indicates that the only governing velocity is the outer velocity which basically means that we are solving the equation $\dot{x} = x$. Therefore the x component is expected to grow exponentially. Figure 4.20 illustrates the maximum value of x component in semi-log scale and verifies the initial assumption. Next, an infinite capillary number is considered with $\lambda = 0.5$. In this case, the double layer velocity is contributing to the outer velocity which slows down the evolution. Figure 4.21 plots the value of $1/x$ for different n . Using $n = 256$ computational points with

$\Delta t = 0.005$, the solution breaks down at $t = 2.55$. By increasing the computational points to $n = 512$ points with $\Delta t = 0.0001$, the solution breaks down at time equal to $t = 2.68$. The break down time further increases to $t = 2.9$, using $n=1024$ points and $\Delta t = 0.0001$. Therefore it is concluded that no finite time singularity occurs and when the required resolution is available, the solution can be computed for longer times.

The shape of the drop at pinch-off only depends on the viscosity ratio λ and is independent of the capillary number Ca and of c_2 . As the capillary number increases, the pinch-off occurs at two points further away from the center but the geometrical shape of the drop at the pinch-off remains the same. Figure 4.22 plots the evolution of a drop for $c_2 = -0.2$, $\lambda = 0.01$ and various capillary numbers. As shown in this figure, it is evident that the points where the pinching occurs move away from the center and finally for capillary number past Ca_s , the drop keeps elongating from the corners. The smaller the value of c_2 is in magnitude, the more the drop becomes elongated but the geometrical shape of the drop at the pinch-off remains unaltered. Figure 4.23 displays the difference in the shape of the drop observed for two different

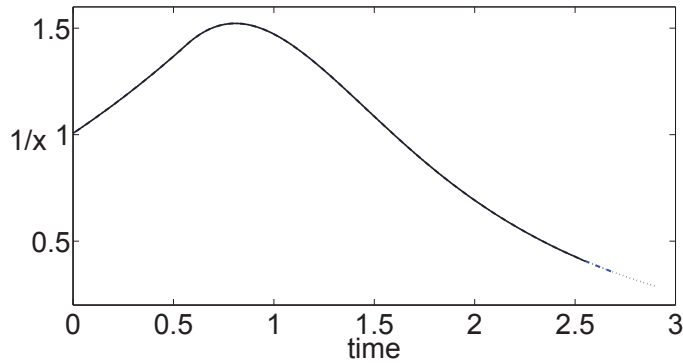


Figure 4.21: The values of $1/x_{max}$ component of the drop for $n = 256$, $\Delta t = 0.0005$ (solid curve), $n = 512$, $\Delta t = 0.0001$ (blue dashed-dot curve) and $n = 1024$, $\Delta t = 0.0001$ (dot curve).

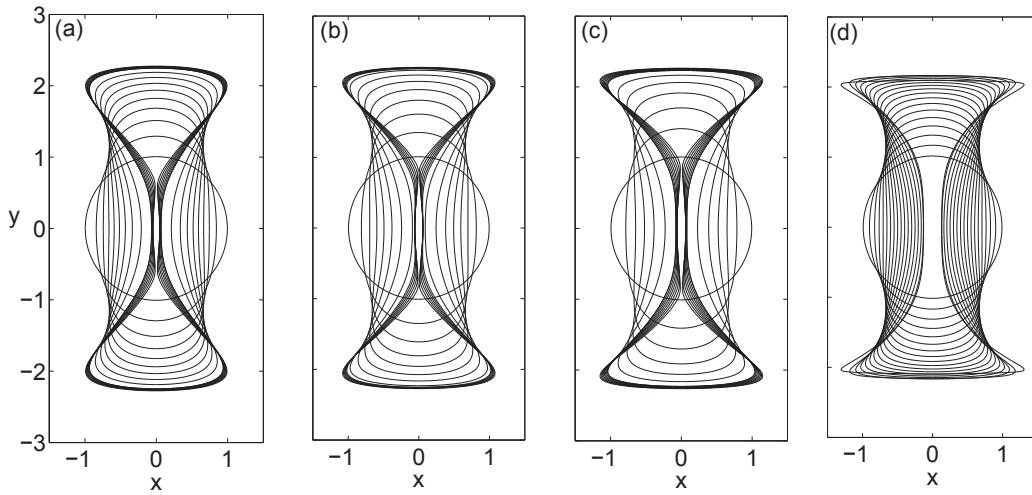


Figure 4.22: Evolution of a drop towards pinch-off for $c_2 = -0.2$ and $\lambda = 0.01$. (a) $Ca = 0.5$ (b) $Ca = 0.6$ (c) $Ca = 0.7$ (d) $Ca = 1$.

values of viscosity ratio. It is visible from figure 4.23 that for $\lambda = 1$, the drop forms a corner shape while it creates a cuspidal shape at the pinch-off when viscosity ratio is low.

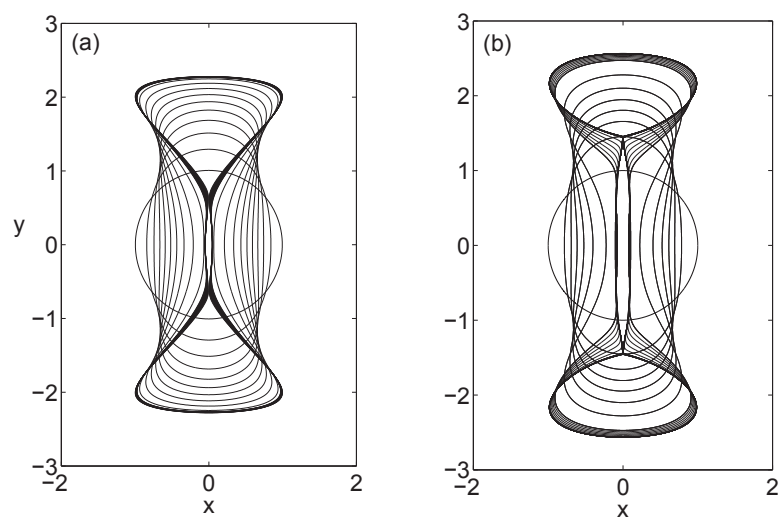


Figure 4.23: Evolution of the drops towards pinch-off for different values of viscosity ratio. (a) $\lambda = 0.01$, $c_2 = -0.2$, $Ca = 0.5$ (b) $\lambda = 1$, $c_2 = -0.2$, $Ca = 0.2$.

Chapter 5

Finite Time Pinch-off and Recoiling

In the previous section it was shown that when c_2 is negative and $Ca_{cr} < Ca < Ca_s$, the viscous drop deforms into a dumbbell shape and finally pinches at two points, displaying a finite time singularity. In this section, we study the detailed dynamics of the drop as pinch-off is approached. Then we present a method to simulate the breaking of the drop and using this method, the evolution of the drop shortly after pinch-off is also presented. Everywhere in this section, the values for $c_2 = -0.2$, $Ca = 0.2$ and $\lambda = 1$ are fixed.

5.1 Pre Pinch-off Numerical Results

Figure 5.1(a), plots the solution at a sequence of time $0 \leq t \leq 38.0068$, computed using the uniform fifth-order rule with $n = 4096$ and $\Delta t = 0.000025$. The interface appears to pinch at two symmetric points. Figure 5.1(b), shows a close-up view near the bottom pinch-off point. In this computation, the method used is the one

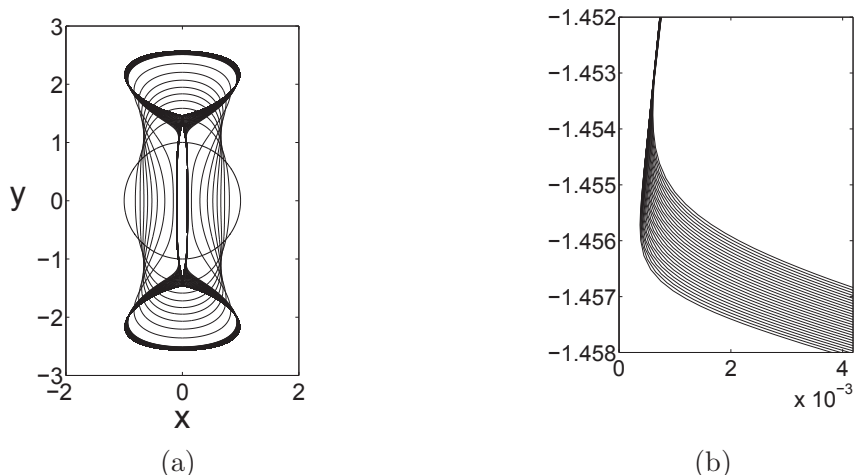


Figure 5.1: Evolution of a drop with $c_2 = -0.2$, $Ca = 0.2$ and $\lambda = 1$ computed using uniformly fifth-order method with $n = 4096$ points. (a) Solution is shown for $t = 0 : 5 : 35$, $t = 35 : 0.25 : 36$, $t = 36 : 0.1 : 37.9$, $t = 37.9 : 0.02 : 38$ and $t = 38 : 0.000025 : 38.00685$ (b) The close-up of bottom pinch-off for $t = 38 : 0.00025 : 38.0066$.

described in section 3.4.2. Initially, points are equally spaced, which means Δs_k is constant in space. As time increases, the drop develops a neck which has a minimum radius x_{min} . We choose s_α so that Δs has a minimum, by using $R(\alpha)$ as shown in figure 3.4 where $\varepsilon_{max} = 0.9989$ is used. The finest spacing in figure 5.1 is equal to $\Delta s = 0.000267408936$, which is equivalent to having 30000 equally-spaced computational points. In figure 5.1, it appears that the neck radius of the drop goes to zero while the y -coordinate of this point is approaching a constant value y_0 in time. To investigate this observation, figure 5.2 plots the minimum radius x_{min} near pinch-off for $n = 4098$ (O), $n = 2048$ (X), and $n = 1024$ (+). The radius approaches zero linearly as time approaches the time of pinch-off, which indicates a finite time singularity. The smallest radius computed with $n = 4096$ is $x_{min} = 0.0003$ and the corresponding maximal curvature is $\kappa_{max} = 2473$.

The pinch-off time is estimated by approximating the $n = 4096$ data using least

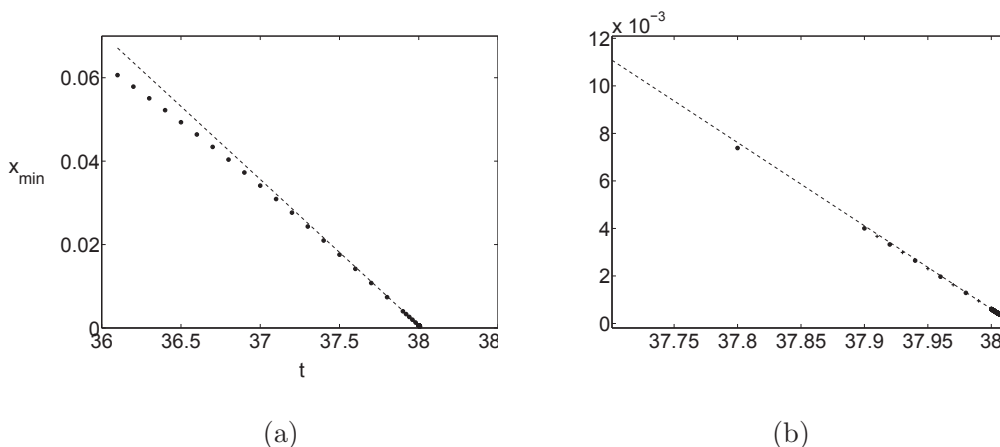


Figure 5.2: (a) Minimum radius of neck vs. time computed using $n = 4098$ (o), $n = 2048$ (X) and $n = 1024$ (+) (b) The close-up. The dashed line is the least squares fit for the interval $(38.0065, 38.0069)$.

squares linear polynomial fit over the interval $[38.0065, 38.0069]$. As can be seen from figures 5.2(a,b), the line thus obtained approximates the data over a much larger interval $[37, 38]$. The estimated pinch-off time is $t_p = 38.0177$. This value is the time at which the line crosses the t -axis. The line approximation agrees with the data over the interval of approximation within 10^{-9} . The fact that all these three data sets are practically indistinguishable gives strong evidence that the results have converged.

Figure 5.3 plots the axial component y_{min} of the neck versus time. To investigate the scaling behavior of y_{min} , its values are approximated by a line over the interval $[38.0065, 38.0069]$, which is used to extrapolate value to $t_p = 38.0177$. The line (see figure 5.3) agrees with data less well than for x . The extrapolated value is $y_0 = -1.459$. Figure 5.4, plots x_{min} and $y_{min} - y_0$ as a function of $t_p - t$, showing their linear scaling. Therefore, x and $y - y_0$ have compatible length scales near pinch-off and

$$x, y - y_0 \sim (t_p - t). \tag{5.1.1}$$

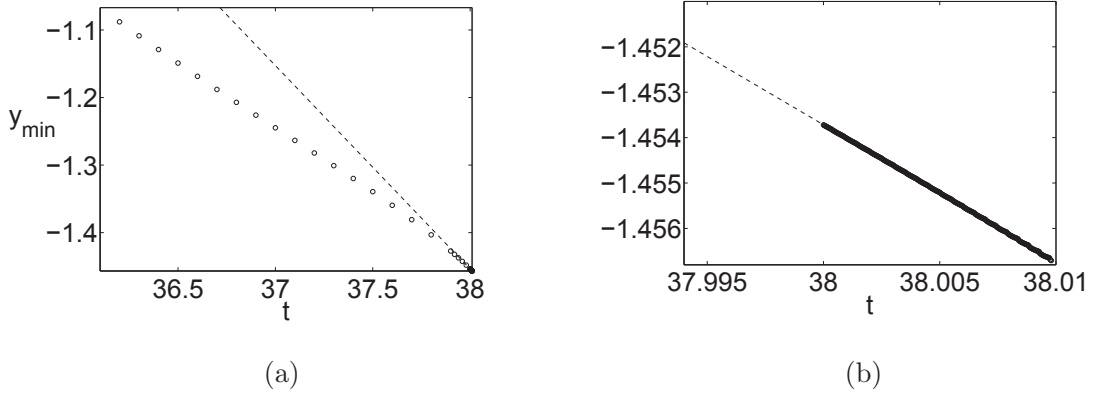


Figure 5.3: (a) Position of pinch-off vs. time computed using $n = 4098$ (b) The close-up. The dashed line is a least squares fit for a small interval near the pinch-off.

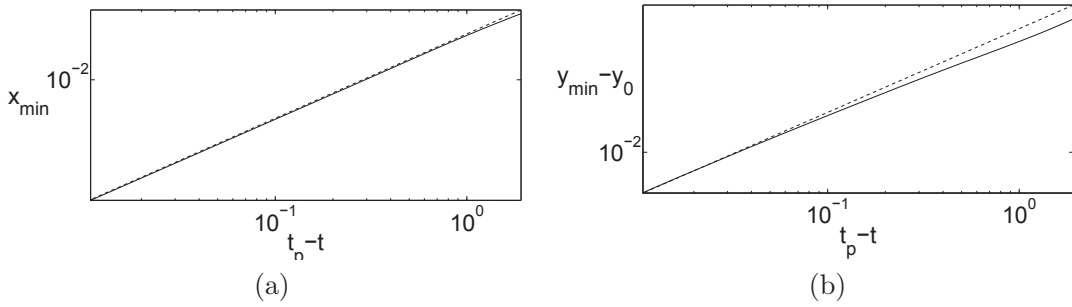


Figure 5.4: (a) Minimum radius of the neck, x_{\min} as a function of the time to pinch, $t_p - t$ (b) $y_{\min} - y_0$ as a function of the time to pinch, $t_p - t$.

Lister and Stone [18] studied a viscous thread surrounded by another viscous fluid. They used dimensional analysis to show that the viscous pinch-off process is self-similar and follows a linear scaling law (see Appendix C). The analysis is based on negligible inertia, and the asymptotic balance between viscous stresses and surface tension. Our findings here agrees with Lister and Stone's work. Note that the drop pinches at two symmetric points. Figure 5.3 only shows the calculations for the lower pinch-off point. Due to symmetry, similar behavior is observed for the top pinch-off.

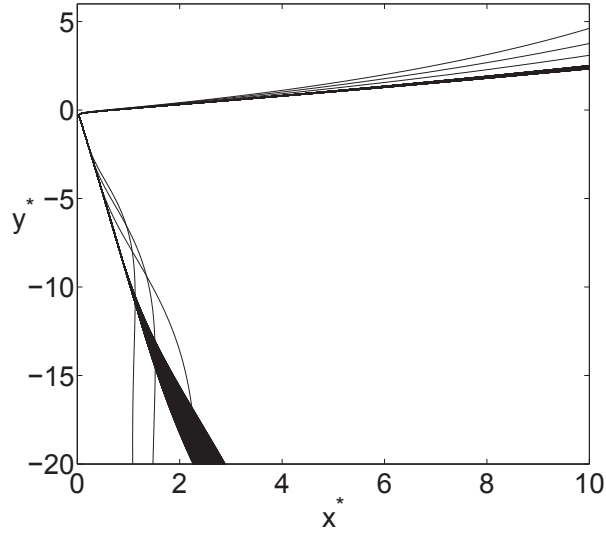


Figure 5.5: Self-similar solution shown for upper pinch-off.

The self-similar components are given as follows

$$x^* = \frac{x}{t_p - t} \qquad y^* = \frac{y - y_0}{t_p - t} \qquad (5.1.2)$$

Figure 5.5 plots the self-similar solution (x^*, y^*) at times $t_p - t$ for $t = 36 : 38.00685$. This figure shows that all the curves collapse into one as $t_p - t \rightarrow 0$. This is indicating that the drop follows the scaling laws near pinch-off.

5.2 Numerical Method to Simulate the Breaking of a Drop

In experiments, it is observed that viscous drops break into droplets. In this section we develop a numerical method to simulate the breaking of the drop surface and reconnection into smaller drops. This approach is explained in three parts.

Close to Pinch-off

The solution is calculated up to time $t = 38.00685$ smooth, using both $n = 2048$, and $n = 4096$. As explained in the previous section, computational points are bunched at the pinch-off locations which enable us to use less computational points. The smallest spacing between points in neck region is the same as if 30000 uniformly spaced points were used.

Cutting

The drop is divided into three separate pieces. Consider the solution at $t = 38.00685$ with $n = 4096$ shown in figure 5.6. Figure shows the solution at a fixed time. We choose to break the interface and reconnect it into two separate pieces by replacing the curve in a region around the point of minimum radius. This region is delimited by two points with indices j_1 and j_2 . Figure 5.6 show two choices for these points: $j_1, j_2 = 905, 916$, and $j_1, j_2 = 908, 913$. We now remove the portion of the interface between j_1 and j_2 . We refer to this process as cutting.

Reconnection

We now place two new pieces of interface between the remaining points j_1, j_2 . See figure 5.7(b) 5.7b. These new pieces are determined as follows. Lets call the start point α_n which refers to j_1 and the end point α^* as shown in picture 5.7. Note that the satellite drop has different start and end points, β_n and β^* , while similar method is applied for those points. Since the drop is symmetric around the y -axis, α^* needs to be located on the y -axis. Based on the given values of $\theta(s(\alpha_n))$, $\dot{\theta}(s(\alpha_n))$, $\ddot{\theta}(s(\alpha_n))$ and $\theta(s(\alpha^*)) = \pi$, a fifth-order polynomial is constructed. To evaluate the polynomial, the arc length $\Delta s = s(\alpha^*) - s(\alpha_n)$ needs to be determined.

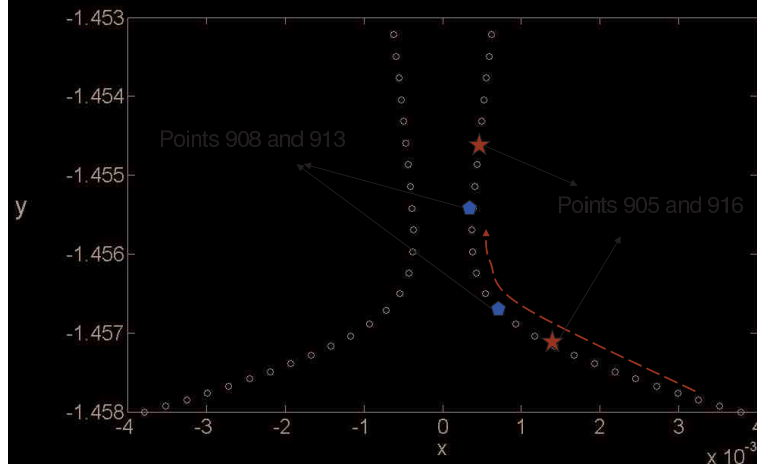


Figure 5.6: Close up of the solution near pinch-off at $t = 38.00685$ and $n = 4096$, points used for cutting at $j_1 = 905$ and $j_2 = 915$ (Red star), $j_1 = 908$ and $j_2 = 913$ (Blue pentagon) and the red curve displays that x coordinate departs away from its minimum value.

It is found that only one value of Δs exists at which the last computational point attains its x -coordinate value at zero. Choosing longer arclength causes the curve to cross the y -axis while shorter x - axis does not reach the axis. Figure 5.8 shows the angle θ as a function of arclength s . The original data are shown by a solid curve and the polynomial interpolation is displayed by a dotted curve. A close-up of the interpolated part is also given. Next, we re-sample the reconnected portions on the new drops by sub-sampling an interpolant of the data. For these new set of points $n = 512$ for each end drop and $n = 1024$ for the satellite is chosen. $\alpha = j\pi/512$ and $\beta = j\pi/1024$ are computed for the end and the middle drop, respectively. For the bottom drop, fixing $\varepsilon_{max} = 0.9989$, $R(\alpha)$ is computed as given in section 3.4.2. Using $R(\alpha)$, $S(\alpha) = L \cdot R(\alpha)$ is evaluated. The values of $s(\alpha)$ are obtained by integrating

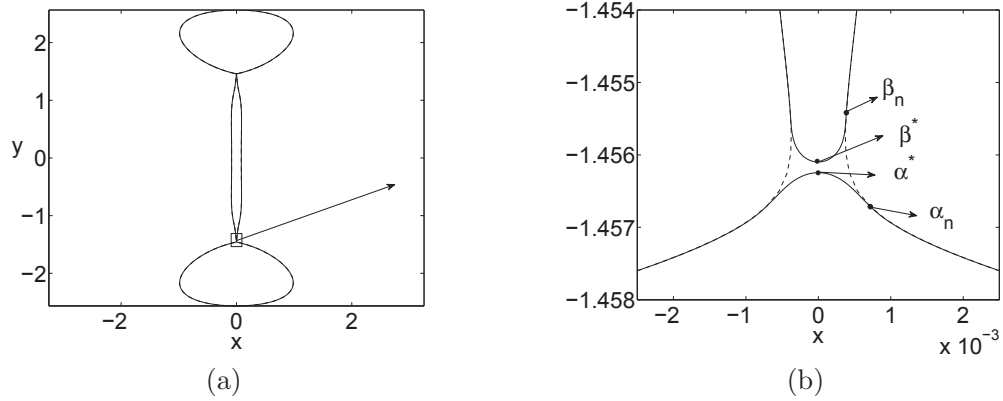


Figure 5.7: (a) Shape of the three separated drops after pinch-off (b) Solution at $t = 38.00685$ (dashed line), cut and reconnected curves (solid line), α^* and α_n , start and end points of the gap for the bottom drop, β^* and β_n start and end points of the gap for the middle drop.

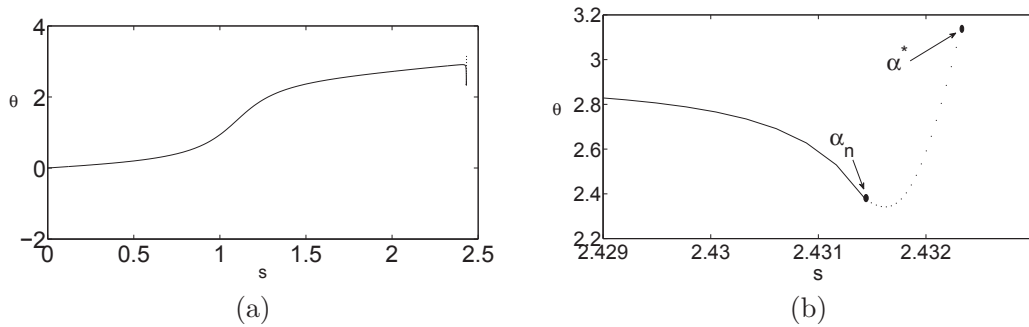


Figure 5.8: (a) θ as a function of arc length s for the bottom drop (-) and fifth-order polynomial interpolation (.) (b) Close up with start point α_n and end point α^* of the interpolation.

s_α and the corresponding θ values are found using a cubic interpolation. Using the new values of θ and s_α the coordinates x and y are calculated by integration.

5.3 Numerical Results of Recoiling

We now investigate the recoiling of the drops after pinch-off, by computing the evolution of the reconnected pieces. It is important to verify whether or not the numerical results computed in this section are independent of the details in the implementation used to simulate breaking. To that effect, two different values of n and three different cuts are considered and compared throughout this section. Figure 5.9 plots two different cuts for $n = 4096$. The dashed line represents the

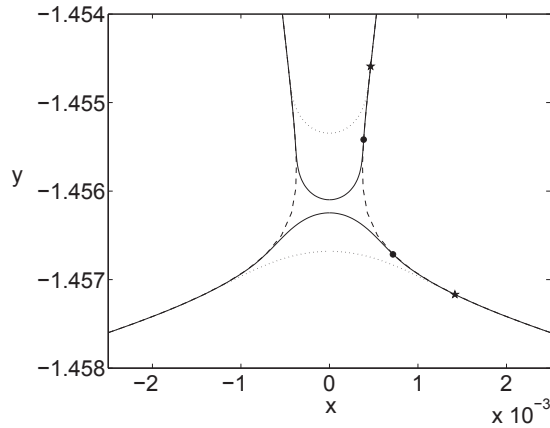


Figure 5.9: Solution before pinch-off at $t = 38.00685$, $n=4096$ (dashed curve), Cut solution with cut points at $j_1 = 905$ and $j_2 = 916$ (dotted curve), Cut solution with cut points at $j_1 = 908$ and $j_2 = 913$ (solid curve).

last solution computed for $t = 38.00685$ with $n=4096$ points. The dotted curve is obtained by cutting the dashed curve at $j_1 = 905$, and $j_2 = 916$ and reconnecting it. The solid curve is obtained by cutting the dashed curve at $j_1 = 908$, and $j_2 = 913$ and reconnecting it.

Figure 5.10 displays the time evolution of a drop after breaking for times $t_c : 0.01 : t_c + 0.1$, where $t_c = 38.00685$ is the time when the drop is cut. The solutions are recorded every 200 steps with time-step $\Delta t = 0.00005$. After breakup, the drops start to retract back which is called the recoiling process.

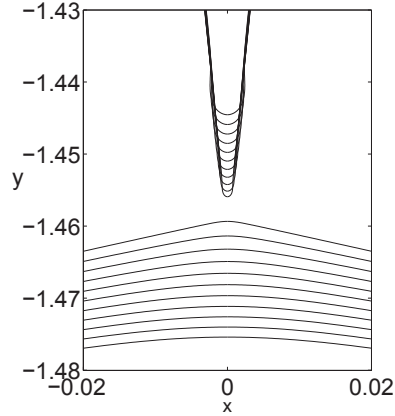


Figure 5.10: Time evolution after pinch-off for $t = 0 : 0.01 : 0.1$.

Brenner et al. [17] studied the droplet fission at a high Reynolds number. He showed that numerical simulations, as well as experimental work, verify that the dynamics after rupture is determined by the shape at the breaking point, and thereby the time dependence of recoiling does not follow a simple scaling law. In this section, the scaling law for a viscous drop after rupture is numerically investigated.

Note that to compute the velocity after recoiling, four components need to be considered. The velocity that one drop induces on itself, the outer velocity, the velocities that the other two drops induce on the corresponding drop. By computing the velocity, using fourth-order Runge-Kutta method, the drop is moved. The last solution computed in this simulation is $t = t_c + 1.53$ at which the method diverge due to formation of another pinch-off. Figure 5.11(a) plots the evolution of the drop up to time $t = t_c + 1.53$. The drops start to retract back until the middle drop surface approaches a second pinch-off. Figure 5.11(b) shows a close-up near the breaking point. The second row displays the step by step evolution of the drop given in part (b) which clearly shows the recoiling process and pinch-off formation. Figure 5.11(c) plots the solution at time $t = t_c + 1.46$ indicating the formation of a new droplet. Part (c) is plotted for two different values of n and three different cuts. The fact that

these three curves are indistinguishable indicates that occurrence of second pinch-off is independent of the method used.

Now we want to find the scaling behavior past pinch-off. Recall that before breakup, to find the time of pinch-off, the minimum neck radius was used. After the drop breaks, there is no neck. Instead, the position of the drop tips are tracked. Figure 5.12 plots the y values of the tip y_{min} in time for the satellite drop and the bottom drop. The linear behavior of these values is evident. Using least squares approximation, the time that two lines cross is computed which determines the breakup time \tilde{t}_p . This approximation also determines the position of pinch-off \tilde{y}_0 . The values obtained here are $\tilde{t}_p = 38.0095$ and $\tilde{y}_0 = -1.457$. Using the values \tilde{t}_p and \tilde{y}_0 , figure 5.13 plots the value $y_{min} - \tilde{y}_0$ as a function of $t - \tilde{t}_p$ in log scale. This plots show that, as $t - \tilde{t}_p$ increases, $y_{min} - \tilde{y}_0$ departs from the line. Assuming that radial scale is linear, the solution is computed and plotted in figure 5.14 for $t = t_c : t_c + 0.5$

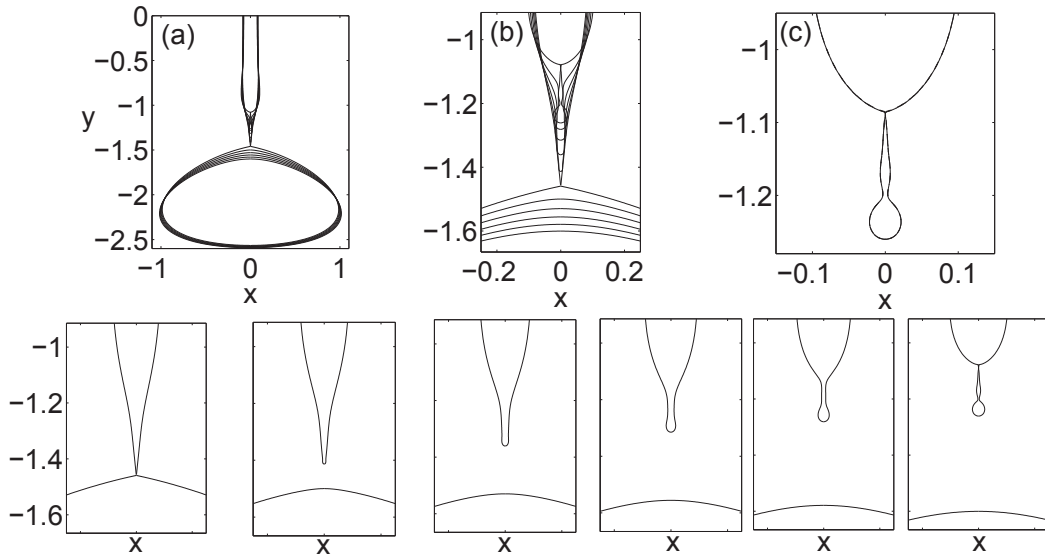


Figure 5.11: First row: (a) Evolution of drops after pinch-off for $t = 0 : 0.3 : 1.53$ (b) Close up of part (a) (c) Close up of new pinch-off for $j=4096$, cut at $j=905,916$ (dashed curve), $n=4096$ cut at $j=908,913$ (dot-dashed curve) and $n=2048$ cut at 510, 521 (dotted curve). Second row: Step by step evolution shown in part (b).

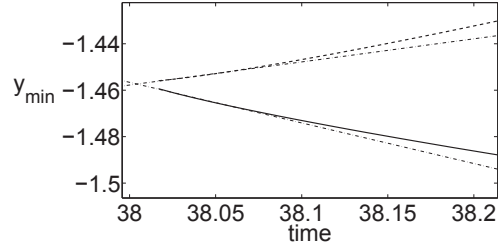


Figure 5.12: Position of the tips y_{min} with respect to time for satellite drop (Solid line), bottom drop (dashed line) and the least square fit (dashed-dot line) $t = t_c : 0.01 : t_c + 0.21$.

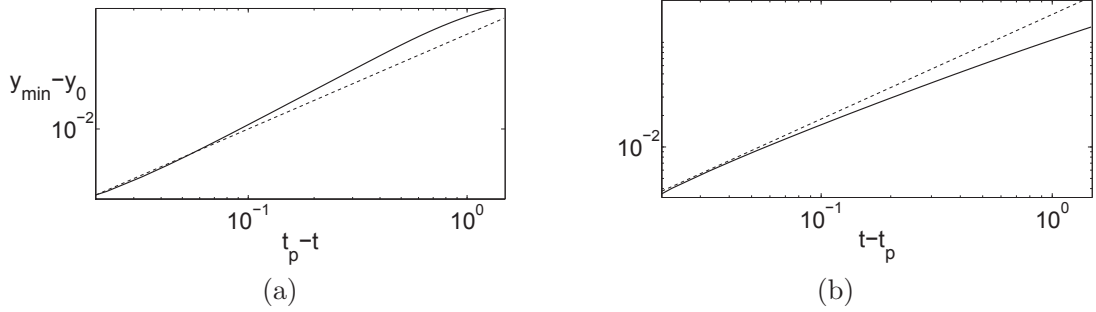


Figure 5.13: (a) Position of pinch-off as a function of time $t - t_p$ for the satellite drop (b) Position of pinch-off as a function of time $t - t_p$ for the bottom drop, dashed line is plotting $t - t_p$.

where,

$$x^* = \frac{x}{t - \tilde{t}_p} \quad y^* = \frac{y - \tilde{y}_0}{t - \tilde{t}_p} \quad (5.3.1)$$

The curves are all collapsing into one curve validating our assumption and verifying the self similarity behavior of the drop after pinch-off. To ease the comparison between figure 5.14 and figure 5.5, the self similar solutions are shown for upper pinch-off in figure 5.14.

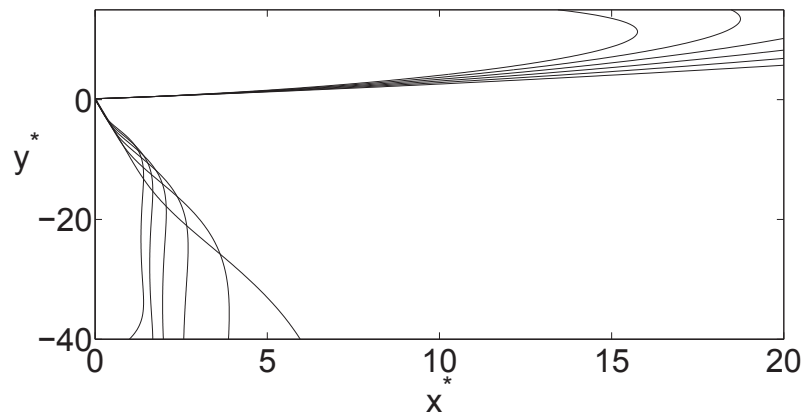


Figure 5.14: Self-similar solution after pinch-off shown for upper pinch-off.

Chapter 6

Conclusions

6.1 Summary and Conclusions

This dissertation studies the evolution of a viscous drop placed in another viscous fluid subject to an axisymmetric strain flow. A fifth-order boundary integral method is used.

The first part of this study focuses on presenting a clear classification of steady state solutions in parameter space. This parameter space consists of the critical capillary number Ca , the viscosity ratio λ , and the nonlinear term in the outer flow c_2 . The variation of the deformation, the maximum curvature, and the critical capillary number as functions of the three key parameters Ca , λ , and c_2 is investigated. Presenting the variation of c_2 in parameter space is a new contribution. We demonstrate previously unobserved biconcave steady shapes and correct some results in the literature describing the critical capillary number as a function of λ .

The second part describes the non-steady evolution of the drops in parameter space. With $c_2 = 0$, the drop reaches an elongated pointed shape. With $c_2 > 0$, the

surface approaches a cusp as it increases in length. With $c_2 < 0$, the drop surface pinches at two points. The existence of a value of capillary number Ca_s is found, above which the drop does not pinch. The importance of using a fifth-order method is indicated. Using this method, we show that the finite time singularity only occurs for $c_2 < 0$, $Ca_{cr} < Ca < Ca_s$.

Finally, the third part focuses on the evolution of the drop, before and after pinch-off. We develop a numerical method which enables us to compute the time evolution after pinch-off. The drop pinches at two points and breaks into three drops. The drop follows a linear self similar scaling before and after pinch-off. After breaking, a second pinch-off forms and a third pinch-off is predicted.

6.2 Proposed Future Research

The interesting results found in the course of this investigation have led to several new research ideas for future work. The method developed here can be further used to study the pinch-off of a viscous drop for different values of viscosity ratios as well as an inviscid case. There have been several studies that investigate the effect of a surfactant on the deformation and tip curvature [11], [36], [15] and [37]. This work can be further extended by adding a surfactant to the interface of the drop. A full investigation of the second drop forming after pinch-off can also be done by using the same method developed here. It is very interesting to find out how long this pinching process continues and how the droplets' dynamics change.

Appendices

A Derivation of G, Ω, p and T	1
B Contribution of u_∞ on Inner and Outer Velocity	2
C Scaling Arguments	3

Appendix A

Derivation of \mathbf{G} , Ω , p and T

This appendix summarizes the derivations of Green's function and its curl. Consider $G_{ij} = (I\nabla^2 - \nabla\nabla)r$ where $r = \|\hat{\mathbf{x}}\| = \|\mathbf{x} - \mathbf{x}_0\|$. Let $\mathbf{x} = (x_1, y_1, z_1)$ and $\mathbf{x}_0 = (x_0, y_0, z_0)$, thus r can be written as $r = \sqrt{(x_1 - x_0)^2 + (y_1 - y_0)^2 + (z_1 - z_0)^2}$, which implies to

$$\nabla r = \left(\frac{x_1 - x_0}{r}, \frac{y_1 - y_0}{r}, \frac{z_1 - z_0}{r} \right). \quad (\text{A.0.1})$$

By taking the divergence of equation (A.0.1), the Laplacian of r is computed as follows,

$$\begin{aligned} \nabla^2 r &= \nabla \cdot \nabla r = \left(\frac{r - \frac{x_1 - x_0}{r} \cdot (x_1 - x_0)}{r^2} + \frac{r - \frac{y_1 - y_0}{r} \cdot (y_1 - y_0)}{r^2} + \frac{r - \frac{z_1 - z_0}{r} \cdot (z_1 - z_0)}{r^2} \right) \\ &= \frac{1}{r} - \frac{(x_1 - x_0)^2}{r^3} + \frac{1}{r} - \frac{(y_1 - y_0)^2}{r^3} + \frac{1}{r} - \frac{(z_1 - z_0)^2}{r^3} = \frac{2}{r}. \end{aligned} \quad (\text{A.0.2})$$

Taking the gradient of equation (A.0.1) yields

$$\nabla(\nabla r) = \begin{pmatrix} \frac{1}{r} - \frac{(x_1 - x_0)^2}{r^3} & \frac{-(x_1 - x_0)(y_1 - y_0)}{r^3} & \frac{-(z_1 - z_0)(x_1 - x_0)}{r^3} \\ \frac{-(x_1 - x_0)(y_1 - y_0)}{r^3} & \frac{1}{r} - \frac{(y_1 - y_0)^2}{r^3} & \frac{-(z_1 - z_0)(y_1 - y_0)}{r^3} \\ \frac{-(z_1 - z_0)(x_1 - x_0)}{r^3} & \frac{-(z_1 - z_0)(y_1 - y_0)}{r^3} & \frac{1}{r} - \frac{(z_1 - z_0)^2}{r^3} \end{pmatrix}. \quad (\text{A.0.3})$$

Appendix A. Derivation of \mathbf{G}, Ω, p and T

Using equations (A.0.2) and (A.0.3), the Green's function can be written as

$$\mathbf{G} = I\nabla^2 r - \nabla\nabla r = \begin{pmatrix} \frac{2}{r} & 0 & 0 \\ 0 & \frac{2}{r} & 0 \\ 0 & 0 & \frac{2}{r} \end{pmatrix} - \begin{pmatrix} \frac{1}{r} - \frac{(x_1-x_0)^2}{r^3} & \frac{-(x_1-x_0)(y_1-y_0)}{r^3} & \frac{-(z_1-z_0)(x_1-x_0)}{r^3} \\ \frac{-(x_1-x_0)(y_1-y_0)}{r^3} & \frac{1}{r} - \frac{(y_1-y_0)^2}{r^3} & \frac{-(z_1-z_0)(y_1-y_0)}{r^3} \\ \frac{-(z_1-z_0)(x_1-x_0)}{r^3} & \frac{-(z_1-z_0)(y_1-y_0)}{r^3} & \frac{1}{r} - \frac{(z_1-z_0)^2}{r^3} \end{pmatrix} = \frac{\delta_{ij}}{r} - \frac{\hat{x}_i\hat{x}_j}{r^3}.$$

Next we compute Ω_{ij} using the relationship $\Omega_{ij} = \nabla \times \mathbf{G}_{ij}$ as follows,

$$\Omega_{ij}(\hat{\mathbf{x}}) = \begin{pmatrix} 0 & 2\frac{\hat{x}_3}{r^3} & -2\frac{\hat{x}_2}{r^3} \\ -2\frac{\hat{x}_3}{r^3} & 0 & 2\frac{\hat{x}_1}{r^3} \\ 2\frac{\hat{x}_2}{r^3} & -2\frac{\hat{x}_1}{r^3} & 0 \end{pmatrix}$$

where $\hat{x}_1 = x_1 - x_0$, $\hat{x}_2 = y_1 - y_0$, and $\hat{x}_3 = z_1 - z_0$. As an example the component Ω_{21} can be computed as follows,

$$\begin{aligned} \Omega_{21} &= -\partial_1 G_{31} + \partial_3 G_{11} = -\frac{\partial}{\partial \hat{x}_1} \left(\frac{\hat{x}_3 \hat{x}_1}{r^3} \right) + \frac{\partial}{\partial \hat{x}_3} \left(\frac{1}{r} + \frac{\hat{x}_1^2}{r^3} \right) \\ &= -\frac{\hat{x}_3 r^3 - 3r^2 \frac{\hat{x}_1}{r} \hat{x}_1 \hat{x}_3}{r^6} + \left[\frac{\left(\frac{-\hat{x}_3}{r} \right)}{r^2} + \frac{-3r^2 \left(\frac{\hat{x}_3}{r} \right) \hat{x}_1^2}{r^6} \right] \\ &= \frac{-2\hat{x}_3}{r^3} \end{aligned}$$

that is equal to the following equation when $i = 2, j = 1, l = 3$, and $\varepsilon_{213} = -1$

$$\Omega_{ij}(\hat{\mathbf{x}}) = 2\varepsilon_{ijl} \frac{\hat{x}_l}{r^3}$$

where

$$\varepsilon_{ijk} = \begin{cases} 0 & \text{unless } i, j, k \text{ are distinct} \\ +1 & \text{if } (i, j, k) \text{ is an even permutation of } (1, 2, 3) \\ -1 & \text{if } (i, j, k) \text{ is an odd permutation of } (1, 2, 3) \end{cases}$$

and pressure is calculated as follows

$$p = -\frac{1}{4\pi} g_i \cdot \nabla \left(\frac{1}{r} \right) = -\frac{1}{4\pi} g_i \cdot \left(\frac{-\hat{x}_i}{r^2} \right) = -\frac{1}{4\pi} g_i \left(-\frac{\hat{x}_i}{r^3} \right).$$

Appendix A. Derivation of \mathbf{G} , Ω , p and T

Comparing equation above to equation (2.3.3), yields

$$p_i(\hat{\mathbf{x}}) = 2\frac{\hat{\mathbf{x}}_i}{r^3}$$

and finally substituting equations (2.3.13) and (2.3.15) into equation (2.3.6) gives

$$T_{ijk}(\hat{\mathbf{x}}) = -\delta_{ik} \left(\frac{2\hat{\mathbf{x}}_j}{r^3} \right) + \frac{\partial}{\partial x_k} \left(\frac{\delta_{ij}}{r} + \frac{\hat{\mathbf{x}}_i \hat{\mathbf{x}}_j}{r^3} \right) + \frac{\partial}{\partial x_i} \left(\frac{\delta_{kj}}{r} + \frac{\hat{\mathbf{x}}_k \hat{\mathbf{x}}_j}{r^3} \right)$$

that simplifies to

$$T_{ijk}(\hat{\mathbf{x}}) = -6\frac{\hat{\mathbf{x}}_i \hat{\mathbf{x}}_j \hat{\mathbf{x}}_k}{r^5}.$$

Appendix B

Contribution of u_∞ on Inner and Outer Velocity

The aim of this appendix is to demonstrate the impact of outer velocity on the velocities of the fluids inside and outside of the drop. Consider the disturbance field velocity \mathbf{u}^D which is defined by composing the field velocity \mathbf{u} into the outer field velocity \mathbf{u}_∞ . Note that, despite of the continuity of outer field velocity across the interface, the corresponding stress fields are discontinuous due to different viscosities. This discontinuity is given by

$$\Delta \mathbf{f}^\infty = \mathbf{f}^{\infty(1)} - \mathbf{f}^{\infty(2)} = (1 - \lambda) \mathbf{f}^{\infty(1)} = \left(\frac{1}{\lambda} - 1\right) \mathbf{f}^{\infty(2)}. \quad (\text{B.0.1})$$

Applying equation (2.5.3) to \mathbf{u}^∞ yields

$$\int_S f_i^{\infty(2)}(\mathbf{x}) G_{ij}(\mathbf{x} - \mathbf{x}_0) d\mathbf{S}(\mathbf{x}) - \mu_2 \int_S u_i^\infty T_{ijk}(\mathbf{x} - \mathbf{x}_0) n_k(\mathbf{x}) d\mathbf{S}(\mathbf{x}) = 0. \quad (\text{B.0.2})$$

Using equations (B.0.1) and (B.0.3), we can write

$$-\frac{1}{8\pi\mu_1} \int_S \Delta f_i^{\infty(2)}(\mathbf{x}) G_{ij}(\mathbf{x} - \mathbf{x}_0) d\mathbf{S}(\mathbf{x}) + \frac{1 - \lambda}{8\pi} \int_S u_i^\infty T_{ijk}(\mathbf{x} - \mathbf{x}_0) n_k(\mathbf{x}) d\mathbf{S}(\mathbf{x}) = 0. \quad (\text{B.0.3})$$

Appendix B. Contribution of u_∞ on Inner and Outer Velocity

Furthermore, the external disturbance field velocity can be expressed as follows,

$$\begin{aligned} u_j^{(D1)}(\mathbf{x}_0) &= \frac{-1}{8\pi\mu_1} \int_S \Delta f_i(\mathbf{x}) G_{ij}(\mathbf{x} - \mathbf{x}_0) dS(x) + \\ &\frac{1-\lambda}{8\pi} \int_S u_i(\mathbf{x}) T_{ijk}(\mathbf{x} - \mathbf{x}_0) n_k(\mathbf{x}) dS(\mathbf{x}) + \frac{-1}{8\pi\mu_1} \int_S \Delta f_i^\infty(\mathbf{x}) G_{ij}(\mathbf{x} - \mathbf{x}_0) dS(x) \\ &+ \frac{1-\lambda}{8\pi} \int_S u_i^\infty(\mathbf{x}) T_{ijk}(\mathbf{x} - \mathbf{x}_0) n_k(\mathbf{x}) dS(\mathbf{x}). \end{aligned} \quad (\text{B.0.4})$$

Using $\mathbf{u}^{1D} + \mathbf{u}^\infty = \mathbf{u}^1$, and the equation (B.0.3), the external velocity can be written as,

$$\begin{aligned} u_j^{(1)}(\mathbf{x}_0) &= u_j^\infty(\mathbf{x}_0) - \frac{1}{8\pi\mu_1} \int_S \Delta f_i(\mathbf{x}) G_{ij}(\mathbf{x} - \mathbf{x}_0) dS(x) + \\ &\frac{1-\lambda}{8\pi} \int_S u_i(\mathbf{x}) T_{ijk}(\mathbf{x} - \mathbf{x}_0) n_k(\mathbf{x}) dS(\mathbf{x}). \end{aligned}$$

To derive a boundary integral representation for the internal flow, the outer velocity can be expressed as,

$$\begin{aligned} u_j^{(\infty)}(\mathbf{x}_0) &= \frac{1}{8\pi\mu_2} \int_S f_i^{(2)} G_{ij}(\mathbf{x} - \mathbf{x}_0) dS(x) \\ &- \frac{1}{8\pi} \int_S u_i^\infty(\mathbf{x}) T_{ijk}(\mathbf{x} - \mathbf{x}_0) n_k(\mathbf{x}) dS(\mathbf{x}). \end{aligned} \quad (\text{B.0.5})$$

Using equation (B.0.3), the equation (B.0.5) can be further simplified to

$$\begin{aligned} u_j^{(\infty)}(\mathbf{x}_0) &= \frac{1}{\lambda} u_j^{(\infty)}(\mathbf{x}_0) - \frac{1}{8\pi\mu_1\lambda} \int_S \Delta f_i^\infty G_{ij}(\mathbf{x} - \mathbf{x}_0) dS(x) \\ &+ \frac{1}{8\pi} \left(\frac{1-\lambda}{\lambda} \right) \int_S u_i^\infty(\mathbf{x}) T_{ijk}(\mathbf{x} - \mathbf{x}_0) n_k(\mathbf{x}) dS(\mathbf{x}). \end{aligned} \quad (\text{B.0.6})$$

The internal disturbance field velocity can be expressed as follows,

$$\begin{aligned} u_j^{(D2)}(\mathbf{x}_0) &= \frac{-1}{8\pi\mu_1\lambda} \int_S \Delta f_i(\mathbf{x}) G_{ij}(\mathbf{x} - \mathbf{x}_0) dS(x) + \\ &\frac{1-\lambda}{8\pi\lambda} \int_S u_i(\mathbf{x}) T_{ijk}(\mathbf{x} - \mathbf{x}_0) n_k(\mathbf{x}) dS(\mathbf{x}) + \frac{-1}{8\pi\mu_1\lambda} \int_S \Delta f_i^\infty(\mathbf{x}) G_{ij}(\mathbf{x} - \mathbf{x}_0) dS(x) \\ &+ \frac{1-\lambda}{8\pi\lambda} \int_S u_i^\infty(\mathbf{x}) T_{ijk}(\mathbf{x} - \mathbf{x}_0) n_k(\mathbf{x}) dS(\mathbf{x}). \end{aligned} \quad (\text{B.0.7})$$

Appendix B. Contribution of u_∞ on Inner and Outer Velocity

Using $\mathbf{u}^{2D} + \mathbf{u}^\infty = \mathbf{u}^1$, and the equation (B.0.8), the internal velocity can be written as,

$$\begin{aligned} u_j^2(\mathbf{x}_0) &= \frac{1}{\lambda} u_j^{(\infty)}(\mathbf{x}_0) - \frac{1}{8\pi\mu_1\lambda} \int_S \Delta f_i G_{ij}(\mathbf{x} - \mathbf{x}_0) dS(x) \\ &+ \frac{1}{8\pi} \left(\frac{1-\lambda}{\lambda} \right) \int_S u_i(\mathbf{x}) T_{ijk}(\mathbf{x} - \mathbf{x}_0) n_k(\mathbf{x}) dS(\mathbf{x}). \end{aligned} \tag{B.0.8}$$

Appendix C

Scaling Arguments

Consider a viscous drop with radius $x(y, t)$, viscosity μ_2 , and surface tension γ in an ambient fluid of viscosity μ_1 . It has been shown that the dynamics are given by a balance between the axial gradient of the capillary pressure, viscous forces and shear stress forces [18], [14]. The external flow exerts a shear stress of order $\mu_1 \partial v / \partial r$ which the contribution on the balance will be $\mu_1 \partial^2 v / \partial r_2$ to satisfy the dimensions of pressure gradient, $kg/m^2 s^2$. The balance in dynamics is represented as follows,

$$\gamma \frac{\partial x^{-1}}{\partial y} \sim \mu_2 \frac{\partial v^2}{\partial y^2} \sim \mu_1 \frac{\partial^2 v}{\partial r_2}. \quad (\text{C.0.1})$$

The dimensions are matched as,

$$\left[\frac{kg}{s^2} \right] \cdot \left[\frac{1}{m^2} \right] \sim \left[\frac{kg}{ms} \right] \cdot \left[\frac{1}{ms} \right].$$

By taking the integral of $\gamma \frac{\partial x^{-1}}{\partial y} \sim \mu_2 \frac{\partial v^2}{\partial y^2}$ with respect to y , we obtain,

$$\frac{\gamma}{x} \sim \mu_2 \frac{\partial v}{\partial y} = \mu_2 \frac{1}{\tau},$$

and therefore

$$x \sim \frac{\gamma \tau}{\mu_2}. \quad (\text{C.0.2})$$

Appendix C. Scaling Arguments

Now consider $x \sim r$ and $\mu_2 \frac{\partial v^2}{\partial y^2} \sim \mu_1 \frac{\partial^2 v}{\partial r^2}$. It follows from equation (C.0.2) that,

$$x \sim \frac{\gamma\tau}{\mu_2} = \frac{\gamma \frac{y}{v}}{\mu_2} = \frac{\gamma y}{\mu_2 v} \Rightarrow y \sim \frac{v\mu_2}{\gamma} x.$$

Therefore,

$$\frac{\partial^2 v}{\partial x^2} \sim \left(\frac{v\mu_2}{\gamma} \right)^2 \frac{\partial^2 v}{\partial y^2}.$$

Since $\mu_2 \frac{\partial v^2}{\partial y^2} \sim \mu_1 \frac{\partial^2 v}{\partial r^2}$, we obtain,

$$\frac{\mu_2}{\mu_1} \sim \left(\frac{v\mu_2}{\gamma} \right)^2 \Rightarrow \left(\frac{\mu_2}{\mu_1} \right)^{1/2} \sim \frac{\gamma}{v\mu_2} = \frac{\gamma\tau}{y\mu_2}.$$

Lastly $y \sim \frac{\gamma\tau}{\lambda^{1/2}\mu_2}$ which together with equation (C.0.2) demonstrates the linear relationship between x , y values and time to pinch-off.

References

- [1] Nitsche, M., Cenicerros, H., Karniala, A., Naderi, S. A., *High order quadratures for the evaluation of interfacial velocities in axi-symmetric Stokes flows*, J. Comput. Phys. 229, 6318-6342.
- [2] Taylor, G. I., 1934. *The formation of emulsions in definable fields of flow*, Proc. Roy. Soc. Lond. A 146, 501-523.
- [3] Taylor, G. I., 1964. *Conical free surfaces and fluid interfaces*, Proc. 11thInt. Congr. Appl. Mech. 790796
- [4] Buckmaster, J. D., 1972. *Pointed bubbles in slow Stokes flow*, J. Fluid Mech. 55, 385-400
- [5] Barthes-Biesel D., Acrivos, A. 1972. *Deformation and burst of a liquid droplet freely suspended in a linear shear field*, J. Fluid Mech. 61, 1-21
- [6] Siegel, M., 2000. *Cusp formation for time-evolving bubbles in two-dimensional stokes flow*, J. Fluid Mech. 412, 227-257.
- [7] Youngren, G. K., Acrivos, A., 1975. *Stokes flow past a particle of arbitrary shape: a numerical method of solution*, J. Fluid Mech. 69, 377-403.
- [8] Youngren, G. K., Acrivos, A., 1976. *On the shape of a gas bubble in a viscous extensional flow*, J. Fluid Mech. 76, 433.
- [9] Rallison, J. M., Acrivos, A., 1978. *A numerical study of the deformation and burst of a viscous drop in an extensional flow*, J. Fluid Mech. 89, 191-200.
- [10] Rallison, J. M., 1984. *The deformation of small viscous drops and bubbles in shear flows*, Annu. Rev. Fluid Mech. 16, 45-66.
- [11] Pozrikidis, C., 1998. *Numerical studies of cusp formation at fluid interfaces in stokes flow*, J. Fluid. Mech. 357, 29-57.

References

- [12] Eggers, J., du Pont, S. C., 2009. *Numerical analysis of tips in viscous flow*, Phys. Rev. E 79 (6), 066311(16).
- [13] Sherwood, J. D. 1984. *Tip streaming from slender drops in a nonlinear extensional flow*, J. Fluid Mech. 144, 281-295.
- [14] Eggers, J., 1993. *Universal pinching of 3D axisymmetric free-surface flow*, Phys. Rev. Lett. 71, 3453.
- [15] Stone, H.A., Leal, L. G. 1990 *The effects of surfactants on drop deformation and breakup*, J. Fluid Mech. 220, 161-186.
- [16] Cristini, V., Blawdziewicz, J., Loewenberg, M., 1998. *Drop breakup in three-dimensional viscous flows*, Phys. Fluids 10, 1781-1783.
- [17] Brenner, M. P., Eggers, J., Joseph, K., Nagel, S. R., Shi, X. D., 1997. *Breakdown of scaling in droplet fission at high Reynolds number*, Phys. Fluids 9, 1573-2764
- [18] Lister, J. R., Stone, H. A., 1998. *Capillary Breakup of a viscous thread surrounded by another viscous fluid*, Phys. Fluids. vol.10, 2758-2764.
- [19] Zhang, W. W., Lister, J. R., 1999. *Similarity solutions for capillary pinch-off in fluids of differing viscosity*, Phys. Rev. Lett. 83, 1151-1154.
- [20] Sierou, A., Lister, J. 2003. *Self-similar solutions for viscous capillary pinch-off*, J. Fluid Mech. 497, 381-403.
- [21] Gekle, S., Snoeijer, J. H., Lohse, D., Meer, D., 2009. *Approach to universality in axisymmetric bubble pinch-off*, Phys. Rev. E 80, 036305.
- [22] Stone, H., Leal, L. G., 1989. *Relaxation and breakup of an initially extended drop in an otherwise quiescent fluid*, J. Fluid Mech. 198, 399-427.
- [23] Manga, M., Stone, H., 1993. *Buoyancy-driven interactions between deformable drops at low Reynolds numbers*, J. Fluid Mech. 256, 647-683.
- [24] Loewenberg, M., Hinch, E. J., 1996. *Numerical simulation of a concentrated emulsion in shear flow*, J. Fluid Mech. 321, 395-419.
- [25] Antanovskii, L. K. 1996 *Formation of a pointed drop in Taylor's four-roller mill*, J. Fluid Mech. 327, 325-341.
- [26] Eggleton, C. D., Pawar, Y. P., Stebe, K. J., 1999. *Insoluble surfactants on a drop in an extensional flow: a generalization of the stagnated surface limit to deforming interfaces*, J. Fluid Mech. 385 (1999) 7999.

References

- [27] Jin, F., Gupta, N. R., Stebe, K. J., 2006. *The detachment of a viscous drop in a viscous solution in the presence of a soluble surfactant*, J. Phys. Fluids 22103-10.
- [28] Lac, E., Homsy, G. M., 2006. *Axisymmetric deformation and stability of a viscous drop in a steady electric field* J. Fluid Mech. 590, 239264.
- [29] Pozrikidis, C., 1992. *Boundary integral and singularity methods for linearized viscous flow*, Cambridge Univ. Press, Cambridge, U.K.
- [30] Kress, R., *Linear integral equation*, Springer N.Y.
- [31] Sidi, A., Israeli, M., 1988. *Quadrature methods for periodic singular and weakly singular Fredholm integral equations*, J. Sci. Comput. 3 (2), 201231.
- [32] Fraysse, V., Giraud, L., Gratton, S., Langou, J., 2003. *A set of GMRES routines for real and complex arithmetics on high performance computers*, Tech. Rep. TR/PA/03/3, CERFACS.
- [33] Davis, R. H., 1999. *Buoyancy-driven viscous interaction of a rising drop with a smaller trailing drop*, Phys. Fluids 11 (5), 1016-1028.
- [34] Hou, T. Y., Lowengrub, J. S., Shelley, M. J., 1994. *Removing the stiffness from interfacial flows with surface tension*, J. Comput. Phys. 114, 312-338.
- [35] Nitsche, M., Steen, P. H., 2004. *Numerical simulations of inviscid capillary pinchoff*, J. Comp. Phys. 200, 299-324.
- [36] Milliken, W. J., Stone, H. A., Leal, L. G. 1993 *The effect of surfactant on the transient motion of Newtonian drops*, Phys. Fluids A 5, 69-79.
- [37] Antanovskii, L. K. 1994b *Influence of surfactants on a creeping free-boundary flow induced by two counter-rotating horizontal thin cylinders*, Eur. J. Mech. B Fluids 13, 73-92.